

MINERALOGY OF COPPER SULFIDES IN PORPHYRY COPPER AND RELATED  
DEPOSITS

By

Benjamin N. Schumer

---

Copyright © Benjamin N. Schumer 2017

A Dissertation Submitted to the Faculty of the

DEPARTMENT OF GEOSCIENCES

In Partial Fulfillment of the Requirements

For the Degree of

DOCTOR OF PHILOSOPHY

In the Graduate College

UNIVERSITY OF ARIZONA

2017

## THE UNIVERSITY OF ARIZONA GRADUATE COLLEGE

As members of the Dissertation Committee, we certify that we have read the dissertation prepared by Benjamin N. Schumer, titled “Mineralogy of Copper Sulfides in Porphyry Copper and Related Deposits” and recommend that it be accepted as fulfilling the dissertation requirement for the Degree of Doctor of Philosophy.

---

Date: (14 April 2017) Mark D. Barton

---

Date: (14 April 2017) Robert T. Downs

---

Date: (14 April 2017) C. Eric Seedorff

---

Date: (14 April 2017) J. Brent Hiskey

---

Date: (14 April 2017) Frank K. Mazdab

Final approval and acceptance of this dissertation is contingent upon the candidate's submission of the final copies of the dissertation to the Graduate College.

I hereby certify that I have read this dissertation prepared under my direction and recommend that it be accepted as fulfilling the dissertation requirement.

---

Date: (14 April 2017) Mark D. Barton

### **STATEMENT BY AUTHOR**

This dissertation has been submitted in partial fulfillment of the requirements for an advanced degree at the University of Arizona and is deposited in the University Library to be made available to borrowers under rules of the Library.

Brief quotations from this dissertation are allowable without special permission, provided that an accurate acknowledgement of the source is made. Requests for permission for extended quotation from or reproduction of this manuscript in whole or in part may be granted by the head of the major department or the Dean of the Graduate College when in his or her judgment the proposed use of the material is in the interests of scholarship. In all other instances, however, permission must be obtained from the author.

SIGNED: Benjamin N. Schumer

## ACKNOWLEDGEMENTS

Financial support was provided by Freeport McMoRan Copper and Gold, Newmont Mining, the Mineralogical Society of America Krauss Crystallographic Research Grant, the Tucson Gem and Mineral Society, and the Dewey Fellowship. I would like to thank Ralph Stegen and Robert A. Jenkins of Freeport for providing the samples for my Morenci study. Richard Graeme III and Douglass Graeme provided invaluable samples, maps, photos, and first-hand recollections of the underground geology of the Bisbee district.

I would like to acknowledge those who provided significant help with my research: Hexiong Yang, Mark D. Barton, Frank K. Mazdab, Robert T. Downs, Eric Seedorff, Brent Hiskey, Ken Domanick, JD Mizer, and Simone Runyon. My family and friends provided much needed moral support throughout this long and sometimes tedious process, without which I would have been lost.

## TABLE OF CONTENTS

<b>ABSTRACT .....</b>	<b>8</b>
<b>INTRODUCTION.....</b>	<b>11</b>
OVERVIEW OF STUDY .....	12
<i>Methods and Context</i> .....	13
<b>PRESENT STUDY.....</b>	<b>16</b>
NATROPALERMOITE, A NEW MINERAL.....	16
THE CRYSTAL STRUCTURE OF NICKELSKUTTERUDITE AND OCCUPANCY OF THE ICOSAHEDRAL CATION SITE IN SKUTTERUDITE GROUP MINERALS.....	17
MINERALOGICAL PROFILE OF SUPERGENE SULFIDE ORE, MORENCI.....	19
HYPOGENE MINERALOGY AND ZONING OF POLYMETALLIC LODES, BISBEE.....	20
KEY FINDINGS .....	23
REFERENCES.....	26
<b>APPENDIX A: NATROPALERMOITE, <math>\text{Na}_2\text{SRAL}_4(\text{PO}_4)_4(\text{OH})_4</math>, A NEW MINERAL ISOSTRUCTURAL WITH PALERMOITE, FROM THE PALERMO NO. 1 MINE, GROTON, NEW HAMPSHIRE, USA .....</b>	<b>29</b>
ABSTRACT.....	30
INTRODUCTION.....	30
SAMPLE DESCRIPTIONS AND EXPERIMENTAL METHODS.....	31
<i>Occurrence, physical and chemical properties, and Raman spectra</i> .....	31
<i>X-ray crystallography</i> .....	33
DISCUSSION.....	34
<i>Crystal Structure</i> .....	34
<i>Raman Spectroscopy</i> .....	35
REFERENCES.....	37
FIGURE CAPTIONS .....	38
FIGURES .....	39
TABLE EXPLANATORY NOTES .....	43
TABLES .....	44
<b>APPENDIX B: A NEW FORMULA AND CRYSTAL STRUCTURE FOR NICKELSKUTTERUDITE, <math>(\text{Ni,Co,Fe})\text{As}_3</math>, AND OCCUPANCY OF THE ICOSAHEDRAL CATION SITE IN THE SKUTTERUDITE GROUP .....</b>	<b>48</b>
ABSTRACT.....	49
INTRODUCTION.....	50
EXPERIMENTAL.....	53
RESULTS.....	55
DISCUSSION.....	58
IMPLICATIONS .....	60
ACKNOWLEDGEMENTS.....	60
REFERENCE.....	61
FIGURE CAPTIONS .....	66
FIGURES .....	67
TABLE EXPLANATORY NOTES.....	71
TABLES.....	72
<b>APPENDIX C: MINERALOGICAL PROFILE OF SUPERGENE SULFIDE ORE IN THE WESTERN COPPER AREA, MORENCI MINE.....</b>	<b>77</b>

ABSTRACT .....	78
INTRODUCTION .....	79
SUPERGENE PROCESSES IN PORPHYRY COPPER DEPOSITS.....	81
GEOLOGY OF THE MORENCI DEPOSIT .....	82
WESTERN COPPER STUDY AREA .....	83
MATERIALS AND EXPERIMENTAL METHODS.....	84
RESULTS.....	85
<i>Hypogene Mineralogy</i> .....	85
<i>Supergene Mineralogy</i> .....	86
DISCUSSION .....	88
<i>Comparison of natural and synthetic secondary sulfides</i> .....	88
<i>Ore textures as evidence of supergene fluid composition</i> .....	88
FUTURE WORK.....	91
<i>Effect of crystal structure on formation of copper sulfides</i> .....	91
CONCLUSIONS .....	91
ACKNOWLEDGEMENTS.....	92
REFERENCES.....	93
FIGURE CAPTIONS.....	96
FIGURES .....	98
TABLE EXPLANATORY NOTES.....	102
TABLES .....	103
APPENDIX 1: PETROGRAPHIC DESCRIPTIONS.....	104
APPENDIX 2: MICROPROBE DATA AND NORMALIZATIONS .....	113
TABLE A2-1.....	114

<b>APPENDIX D: HYPOGENE MINERALOGY AND ZONING OF CORDILLERAN POLYMETALLIC LODES AND CONSTRAINTS ON HYDROTHERMAL FLUID EVOLUTION AT BISBEE, COCHISE COUNTY, ARIZONA.....</b>	<b>120</b>
ABSTRACT .....	121
INTRODUCTION .....	123
GEOLOGY OF THE BISBEE DISTRICT.....	125
<i>Sedimentary Rocks</i> .....	125
<i>Igneous Rocks</i> .....	126
<i>Structure</i> .....	128
GENERAL FEATURES OF MINERALIZATION AND HYDROTHERMAL ALTERATION .....	129
MATERIALS AND METHODS.....	132
ORE MINERALOGY .....	132
<i>Overview</i> .....	132
<i>Silica-pyrite bodies</i> .....	133
<i>Chalcopyrite-rich types</i> .....	133
<i>Telluride-bearing ore</i> .....	135
<i>Bornite-rich types</i> .....	136
<i>Mineral compositions in bornite-rich ore</i> .....	137
<i>Chalcocite-rich ore types</i> .....	138
<i>Zn-Pb association</i> .....	140
CONSTRAINTS ON CONDITIONS OF MINERALIZATION .....	141
TIME-SPACE RELATIONSHIPS.....	144
<i>Zonation</i> .....	144
COMPARISON WITH OTHER Cu LODE SYSTEMS.....	147
<i>Carbonate rock hosted lodes</i> .....	148

<i>Igneous rock hosted lodes</i> .....	148
CONCLUSIONS .....	149
ACKNOELWDGEMENTS.....	151
REFERENCES.....	152
FIGURE CAPTIONS.....	159
FIGURES .....	164
TABLE EXPLANITORY NOTES.....	174
APPENDIX 1: PETROGRAPHIC DESCRIPTIONS.....	182
APPENDIX 2: MICROPROBE DATA AND MINERAL NORMALIZATIONS .....	198
TABLE EXPLANITORY NOTES.....	199
TABLES .....	200

## ABSTRACT

Porphyry copper deposits represent one of the largest copper reserves on Earth. They typically contain large, low-grade reserves of primary ore and higher-grade, supergene enrichment blankets of sulfide and oxide ores. Understanding the mineralogy of porphyry copper ores and ores related to porphyry copper systems is exceedingly important for several reasons, foremost of which are the information provided by ore mineral parageneses, assemblages, and mineral chemistry on evolution of these magmatic-hydrothermal systems, and information on mineral processing characteristics of the ores. The focus of this work is to better understand the mineralogy of supergene copper sulfides in porphyry copper systems and hypogene base metal lodes related to porphyry copper systems, and use this mineralogical knowledge to improve our understanding of the processes responsible for ore formation.

The objectives of this study are accomplished by two means: focusing on the crystallography and crystal chemistry of minerals, and then applying this mineralogical knowledge to a supergene sulfide enrichment blanket and hypogene massive sulfides from base metal lodes in southeastern Arizona. The discovery of a new mineral, natropalermoite,  $\text{NaSr}_2\text{Al}_4(\text{PO}_4)_4(\text{OH})_4$ , provided the opportunity to use single-crystal X-ray diffraction to solve a crystal structure, and electron-probe microanalysis (EPMA) to study the crystal chemistry of natropalermoite and how the accommodation of Na in the structure changes lengthens the unit cell along [010] and shortens it along [100] and [001] compared to its lithium analogue, palermoite. Solution of the crystal structure of the mineral nickelskutterudite,  $(\text{Ni},\text{Co},\text{Fe})\text{As}_3$ , allowed for the investigation of anion deficiency in minerals of the skutterudite group, a problem whose solution has eluded

researchers for nearly 100 years. Two skutterudite ( $\text{CoAs}_3$ ) and two nickelskutterudite samples were analyzed using single-crystal X-ray diffraction, EPMA, and procrystal electron density. The results showed fully-occupied anion sites and a cation surplus, which was accommodated in the icosahedral site, proving that minerals of the skutterudite group are not anion deficient.

This mineralogical knowledge was applied to the supergene enrichment blanket in the Western Copper section of the Morenci mine, Greenlee County, and hypogene massive sulfide deposits associated with a porphyry copper deposit at Bisbee, Cochise County, Arizona. This is one of very few studies of supergene sulfide blankets ever completed. One drill hole through the supergene blanket at Western Copper was examined using ore microscopy and EPMA. Results showed dominant (Cu+Fe):S ratios of  $1.80 \pm 0.05$ ,  $1.92 \pm 0.03$ , and  $1.10 \pm 0.10$ , with higher (Cu+Fe):S dominant high in the blanket and low ratios dominant near the base of the blanket. These values were interpreted to be controlled by activity of  $\text{Cu}^{2+}$ ,  $\text{Fe}^{2+}$ , and  $\text{Fe}^{3+}$  in solution.

Massive sulfide deposits at Bisbee were investigated using ore microscopy and EPMA in order to correct the previous conflicting reports of the mineralogy and paragenesis of this famous district and interpret constraints on conditions of ore-forming fluids. Results show four types of ore: chalcopyrite-rich with hematite and/or pyrite, bornite-rich, chalcocite-rich, and a Zn-Pb association. Chalcopyrite-rich ores formed first, followed by bornite-rich and chalcocite-rich ores. All ores were formed at relatively shallow depths from oxidized, moderately sulfur-rich fluids; early fluids were higher temperature and later fluids were lower temperature and considerably more sulfidized. Zinc-lead ores formed early and were continuously dissolved and reprecipitated distal to

Cu-mineralization. These patterns are similar to many other base-metal lode districts worldwide, however Bisbee contains more Zn-Pb ore than other districts with hematite-containing ores and less than those without hematite.

## INTRODUCTION

Copper is mined from a diverse suite of deposit types. Two important classes of Cu deposits are porphyry copper and intrusion-related base metal lodes. Porphyry copper deposits are characterized by large tonnages of relatively low-grade ore in vein stockworks and/or disseminations within hydrothermally altered rock (e.g. Seedorff et al. 2005). Base metal lodes typically form well-zoned massive sulfide vein or replacement bodies, and contain mineral assemblages varying from low to high sulfidation state (Catchpole et al. 2012). Despite the importance of these deposit types, the mineralogy of supergene sulfide enrichments in porphyry copper systems and hypogene mineralogy of base metal lodes in southeastern Arizona remain poorly understood.

A solid foundation in mineralogy and crystal chemistry is necessary for the understanding of such mineralogically complex systems as porphyry copper deposits and base metal lodes. In order to better understand mineralogy and crystal chemistry, and contribute to the overall knowledge in the field, I solved the crystal structures of natropalermoite and nickelskutterudite and investigated the crystal-chemistry of natropalermoite-palermoite and the skutterudite group, addressing the long-standing issue of anion deficiency in skutterudites along the way.

Arizona is home many porphyry copper deposits and base metal lodes (e.g. Lang et al., 2001). Both the Morenci and Bisbee districts were historically important copper producers. Morenci is a very large porphyry copper deposit and ores at Bisbee were predominantly base metal lodes surrounding a multiphase intrusive complex, which hosted a porphyry copper deposit. Mining at Morenci is ongoing, while Bisbee ceased

production in 1975. This dissertation focuses on the supergene ore at Morenci and hypogene ore at Bisbee.

Supergene ore forms the bulk of economic ore at the Morenci mine in Greenlee County, Arizona. Morenci is a large mining complex exploiting a dissected Laramide porphyry copper deposit. Supergene ore at Morenci is processed in two ways: low-grade chalcocite ore is sent directly to run-of-mine leach pads, while ore containing covellite is crushed, milled, and sent to the flotation circuit to produce a concentrate. Understanding how copper sulfides are formed in time and space within the zone of supergene enrichment will allow for better grade control and higher recoveries in leach and flotation circuits. Understanding the secondary sulfide paragenesis and how the chemistry of the copper sulfides changes from top to bottom of the sulfide zone in the enrichment blanket is a focus of this study.

The Bisbee district in southeastern Arizona was a historic source of polymetallic ore from base metal lodes; however the overall paragenetic relationships and mineralogy of the district are still poorly understood. Previous mineralogical studies of the district focused on individual ore bodies or a single ore type (e.g. Tenney, 1916; Schwartz and Park, 1932; Criddle et al., 1982), and the paragenetic information presented in these studies is often conflicting. The focus of this study is to interpret the district-wide paragenesis of hypogene sulfide ores and constrain possible conditions of mineralizing fluids.

## OVERVIEW OF STUDY

Methods used in this study vary widely among sub-studies, and are presented along with results and conclusions in each of the four pre-publication manuscripts attached to this dissertation as Appendices A-D. The methods for used in mineralogical

studies include single-crystal X-ray diffraction and EPMA. I used procrystal electron density modeling, based on single-crystal X-ray data, to investigate the bonded ring of four As atoms in nickelskutterudite. Knowledge gained in the mineralogical and crystal-chemical studies was applied to two little-studied aspects of southeastern Arizona ore deposits to interpret the conditions responsible for the observed mineralogy and parageneses. The first applied mineralogical study is the supergene sulfide blanket in the Western Copper section of the Morenci mine, and the second is polymetallic lode deposits at Bisbee.

#### *Methods and Context*

In the first paper, I describe the new mineral natropalermoite (IMA 2013-118) using single-crystal X-ray diffraction and EPMA to solve the crystal structure and investigate crystal-chemical aspects of the relationship between natropalermoite and palermoite. Natropalermoite,  $\text{NaSr}_2\text{Al}_4(\text{PO}_4)_4(\text{OH})_4$ , was discovered on a sample of palermoite from the Palermo No. 1 mine, North Groton, New Hampshire, which I donated to the RRUFF project. The goal of this study was to describe a mineral new to science and investigate its relationships with previously described minerals with identical crystal structures but vastly different chemistry, such as carminite  $\text{PbFe}^{3+}_2(\text{AsO}_4)_2(\text{OH})_2$ .

In the second paper, I describe the crystal structure of nickelskutterudite  $(\text{Ni},\text{Co},\text{Fe})\text{As}_3$ , for the first time using single-crystal X-ray diffraction and EPMA, and investigate the long-standing issue of anion deficiency in skutterudite group minerals. Skutterudite group minerals, of ideal formula  $BX_3$  or  $B_4X_{12}$  where  $B$  is Co, Ni, or Fe and  $X$  is As or Sb, adopt a distorted perovskite structure, with an unoccupied A or icosahedral site and tilted  $BX_6$  octahedra which bring together four X atoms in otherwise unoccupied

icosahedral sites to form bonded 4-member rings (Aleksandrov and Beznosikov, 2007). Numerous synthetic compounds isostructural with natural skutterudites exist, and are either filled, with a partially to fully occupied icosahedral site and general formula  $AB_4X_{12}$ , or a vacant icosahedral site and general formula  $BX_3$ . Synthetic filled skutterudites are widely studied because of their thermoelectric properties such as low thermal conductivity and high Seebeck coefficients (e.g. Chakoumakos and Sales, 2006; Fukuoka and Yamanaka, 2009).

Current IMA nomenclature described skutterudite and nickelskutterudite as anion deficient:  $CoAs_{3-x}$  and  $NiAs_{3-x}$ . The issue of whether or not skutterudites are actually anion deficient has been widely discussed for nearly 100 years, and provided motivation for this study. Site-occupancy refinement of nickelskutterudite and skutterudite allowed for the investigation of anion deficiency and additionally provided data on the chemistry of nickelskutterudite.

In the third paper, I investigate the mineralogy of supergene sulfide enrichment in the Morenci mine by ore microscopy and EPMA. Enrichment of low-grade hypogene ore in porphyry copper deposits by supergene processes results in a blanket of supergene ore in many cases of much higher grade than the primary ore (Anderson, 1982; Titley and Marozas, 1995; Sillitoe, 2005). Despite the importance of supergene sulfide enrichments, comparatively few detailed mineralogical studies of natural supergene copper sulfides have been completed to date, such as the work of Sillitoe and Clark (1969) on supergene Cu sulfides and Cu-Fe sulfides in the Copiapó district, Chile, or the EPMA study of Cu sulfides in red-bed copper deposits of Alberta by Goble and Smith (1973). Investigation of paragenesis and changes in (Cu,Fe):S by depth allows for a detailed understanding of

the mineralogy of supergene sulfide enrichments and interpretation of fluid conditions responsible for the observed textures and compositions. These data will also allow for better grade control and Cu recovery in mill and leach circuits at the Morenci mine.

In the fourth paper, I investigate the mineralogy and paragenesis of hypogene polymetallic lodes in the Bisbee district, Arizona. The motivation behind this study is often conflicting paragenetic relationships reported in earlier works and a lack of application of this work at a district-scale. The Graeme family of Bisbee provided access to specimens from the now flooded workings. Using ore microscopy, I examine the mineralogy and paragenetic relationships of ores from throughout the district. I use EPMA to trace the chemical composition of sphalerite and tennantite-group minerals by ore type. Ore microscopy results allow for the interpretation of the progression of mineralization with time and zoning at both ore body and district scales. Examination of paragenetic, zoning, and chemical data allows for interpretation of fluid evolution in time and space throughout the Bisbee district. Wherever possible, these observations are compared to those of previous workers to build a more complete picture of the processes involved.

## PRESENT STUDY

In this section I present an overview of how the results of my work enhance the knowledge of the mineralogy/crystal chemistry and the mineralization processes in porphyry copper and related deposits in southeastern Arizona.

### NATROPALERMOITE, A NEW MINERAL

In Appendix A, I present a description of the new mineral natropalermoite. Natropalermoite is named for the sodium (natrium) content and isostructural relationship with palermoite. The new mineral and its name have been approved by the Commission on New Minerals, Nomenclature and Classification (CNMNC) of the International Mineralogical Association (IMA 2013-118). It occurs as a secondary phosphate formed from hydrothermal alteration of primary triphyllite in the core-margin zone of the Palermo No. 1 pegmatite (Page and Larrabee 1962, Segeler et al. 1981). Minerals associated with natropalermoite include palermoite, lefontite, childrenite, iron oxides, and quartz. Natropalermoite forms prismatic crystals up to 0.2 mm in length, elongated and striated along the  $a$  axis. It is brittle, with subconchoidal to fibrous fracture and perfect cleavage  $\{001\}$ , fair on  $\{100\}$  and no parting was observed. Natropalermoite is non-pleochroic, biaxial (-),  $\alpha = 1.624(1)$ ,  $\beta = 1.641(1)$ ,  $\gamma = 1.643(1)$  (589 nm),  $2V_{\text{meas}} = 43(4)^\circ$ ,  $2V_{\text{calc}} = 38^\circ$ , dispersion  $v > r$ , medium to weak. Chemistry measured by electron microprobe corresponds to an empirical formula of

$(\text{Na}_{1.69}\text{Li}_{0.31})_{\Sigma 2.00}(\text{Sr}_{0.95}\text{Mg}_{0.04}\text{Ca}_{0.02}\text{Ba}_{0.01})_{\Sigma 1.02}(\text{Al}_{3.82}\text{Mn}_{0.03}\text{Fe}_{0.03})_{\Sigma 3.88}(\text{P}_{1.01}\text{O}_4)_4(\text{OH})_4$  based on 20 O atoms per formula unit, which can be simplified to  $\text{Na}_2\text{SrAl}_4(\text{PO}_4)_4(\text{OH})_4$ .

Natropalermoite is orthorhombic, adopting space group  $Imcb$ , with cell dimensions  $a = 11.4849(6)$ ,  $b = 16.2490(7)$ ,  $c = 7.2927(4)$  Å,  $V = 1360.95(17)$  Å<sup>3</sup>,  $Z = 4$ . The crystal structure consists of two  $\text{AlO}_4(\text{OH})_2$  octahedra form edge-sharing

$\text{Al}_2\text{O}_7(\text{OH})_3$  dimers. These dimers are corner linked to one another at OH<sub>2</sub>, forming infinite zigzag chains along [100]. Chains are hexagonal closest packed, accounting for the hexagonal morphology of the crystals. Chains are interconnected by PO<sub>4</sub> groups. Sodium and strontium atoms are accommodated within channels along [100]. Sodium atoms are staggered, forming a “double stack” arrangement, while Sr atoms are “single file.” The larger size of Na versus Li atoms increases the width of the channels accommodating sodium in the [010] direction, lengthening the overall *b* dimension of the unit cell. Widening of the channels along [010] results in the angle between the two octahedra in the  $\text{Al}_2\text{O}_7(\text{OH})_3$  dimer to narrow, and causes the shortening of the *a* = 11.4849(6) and *c* = 7.2927(4) Å dimensions of natropalermoite versus those of palermoite: *a* = 11.577(1) and *c* = 7.3276(7) Å.

#### THE CRYSTAL STRUCTURE OF NICKELSKUTTERUDITE AND OCCUPANCY OF THE ICOSAHEDRAL CATION SITE IN SKUTTERUDITE GROUP MINERALS

In Appendix B, I present the first description of the crystal structure of nickelskutterudite. Single-crystal X-ray diffraction data were collected using a crystal from the Alhambra mine, New Mexico, and used to solve the crystal structure. Stanley Evans of the University of Arizona completed chemical analyses using EPMA. A total of four samples were analyzed, two nickelskutterudites and two skutterudites.

Nickelskutterudite is cubic, space group  $Im\bar{3}$ , adopting a distorted perovskite structure. The crystal structure consists of one metal site fully occupied by Ni, Co, or Fe, in octahedral coordination with six As atoms. Octahedra are distorted and notably tilted, resulting in four As atoms stuffed into three of every four icosahedral cages centered on A sites. Procrystal electron density modeling shows each As atom is bonded to two cations and two other As atoms, resulting in a rectangular, four-member ring with edges

2.547 Å and 2.475 Å. Site-occupancy refinement showed the anion site is fully-occupied in all samples, and a cation surplus was found in one skutterudite and one nickelskutterudite sample. This cation surplus is accommodated at the one *A* site not occupied by an As<sub>4</sub> ring.

The angle of octahedral tilt for phases isomorphous with skutterudite is derived from the relationship of the skutterudite unit cell (space group  $Im\bar{3}$ ) to the ReO<sub>3</sub> unit cell (space group  $Pm\bar{3}m$ ). The unit cell edge *a* for ReO<sub>3</sub> in space group  $Pm\bar{3}m$  is equal to twice the Re-O distance **d**, or 2**d**, and as ReO<sub>3</sub> has no octahedral tilt, it is not necessary to factor tilt into the equation,  $a = 2\mathbf{d}$ .

Tilting of the  $MX_6$  octahedra about [111] relative to their positions in the  $Pm\bar{3}m$  unit cell doubles the size of the  $Im\bar{3}$  unit cell edge versus that of the  $Pm\bar{3}m$  cell, or 4**d**, where **d** is the *M-X* distance. Thinking of octahedral tilt as a linear transformation on the location of the  $MX_6$  octahedra in  $Pm\bar{3}m$  to  $Im\bar{3}$ , the overall magnitude of tilt is equal to the trace of the linear transformation matrix, or  $1+2\cos\phi$ . The tilt operates about all three of the pseudocubic subcell axes, so the overall tilt must be averaged, giving  $(1+2\cos\phi)/3$ . Factoring the tilt into the equation for *a*, we have  $a = 4\mathbf{d}[(1+2\cos\phi)/3]$ , and solving for  $\cos\phi$  gives  $\cos\phi = 3a/8\mathbf{d} - 0.5$ .

Electron microprobe analyses by Stanley Evans gave an empirical chemical formula of  $(\text{Ni}_{0.62}\text{Co}_{0.28}\text{Fe}_{0.12})_{\Sigma=1.02}(\text{As}_{2.95}\text{S}_{0.05})_{\Sigma=3.00}$  normalized to three anions. Natural nickelskutterudite is always reported with significant Co and Fe, and pure NiAs<sub>3</sub> has not been synthesized. This observation is consistent with Ni<sup>4+</sup> being unable to spin-pair its seven non-bonded electrons, requiring Co<sup>3+</sup> and Fe<sup>2+</sup>, which can spin-pair all non-bonded electrons, to stabilize the structure. The lack of anion deficiency and inclusion of

structurally necessary Co and Fe, led us to propose the formula of nickelskutterudite be changed from  $\text{NiAs}_{3-x}$  to  $(\text{Ni,Co,Fe})\text{As}_3$ . The IMA has approved this change.

#### MINERALOGICAL PROFILE OF SUPERGENE SULFIDE ORE, MORENCI

In Appendix C, I investigate the mineralogy of supergene copper sulfides in the Morenci mine, Greenlee County, Arizona. Samples used in this study originate from HQ drill hole 4511 in the Western Copper section of the Morenci mine. The motivation behind this study is to better understand the changes in supergene copper sulfide mineralogy in space within the enrichment blanket to better aid mineral processing and to provide a detailed mineralogical study of supergene copper sulfides, which are generally lacking for porphyry copper deposits in southwestern North America. The investigation focused on the chemistry of supergene sulfides and paragenetic relationships between of supergene and hypogene minerals. Hypogene minerals identified in hole 4511 are chalcopyrite, pyrite, quartz, and minor molybdenite. Sieve-textured pyrite contains inclusions of hematite, sphalerite, acanthite, a Cu-Bi-S phase, and an Ag-Bi-Te phase.

Three main ore textures were observed in supergene copper sulfides: partial to complete replacement of chalcopyrite, partial replacement of pyrite, and partial to complete replacement of one another. Compositions for copper sulfides vary widely, but  $(\text{Cu}+\text{Fe}):\text{S}$  ratios of  $1.80 \pm 0.05$ ,  $1.92 \pm 0.03$ , and  $1.10 \pm 0.10$  are dominant, and no stoichiometric  $\text{Cu}_2\text{S}$  was found. High Cu:S phases  $1.80 \pm 0.05$  and  $1.92 \pm 0.03$  replacing primary chalcopyrite and pyrite or lower Cu:S supergene sulfides are dominant high in the enrichment blanket and near/within faults. Near the base of the blanket low Cu:S phases  $1.10 \pm 0.10$  replacing primary chalcopyrite or higher Cu:S supergene sulfides gradually become more dominant. Pyrite is only replaced by high Cu:S phases, and then only when no chalcopyrite is present.

Petrographic data were coupled with chemical data to interpret possible conditions required to form the observed ore textures in hole 4511, dependent on the concentrations of  $\text{Cu}^{2+}$ ,  $\text{Fe}^{2+}$ , and  $\text{Fe}^{3+}$  in the descending solutions. Direct replacement of chalcopyrite by low Cu:S phases requires high concentrations of  $\text{Cu}^{2+}$  in solution. Formation of high Cu:S phases directly from chalcopyrite, by analogy with synthetic chalcopyrite leaching, requires high concentrations of both  $\text{Fe}^{2+}$  and  $\text{Cu}^{2+}$  in solution (Hiroyoshi et al., 2000). Replacement of pyrite by high Cu:S phases, seen only in faults and in areas of low chalcopyrite content, also indicates the necessity of high  $\text{Cu}^{2+}$  concentration: without dissolved iron species in solution, pyrite replacement requires almost 3 moles of  $\text{Cu}^{2+}$  for each mole of pyrite, whereas chalcopyrite replacement requires only 1 mole of  $\text{Cu}^{2+}$ . These conditions would be met high in the blanket or within faults where access to fresh fluids would provide the required amounts of  $\text{Cu}^{2+}$  and  $\text{Fe}^{2+}$  in solution.

Replacement of copper sulfides by one another is governed by redox potential and dissolved copper and iron species (Hiskey and Wadsworth, 1982; Titley and Mazoras, 1995). High Cu:S phases replacing lower Cu:S phases is the most commonly observed texture, however the reverse is seen in several samples. Replacement of lower Cu:S phases by those richer in copper is interpreted as an example of reducing conditions, or possibly high activities of  $\text{Cu}^{2+}$  and  $\text{Fe}^{2+}$  (Walsh and Rimstidt, 1986). Lower Cu:S phases replacing higher Cu:S phases indicates progressive leaching of Cu by oxidizing fluids during a drop in the water table.

#### HYPOGENE MINERALOGY AND ZONING OF POLYMETALLIC LODES, BISBEE

In Appendix D, I investigate the mineralogy and zoning of Cordilleran polymetallic lodes at Bisbee, Arizona, related to the multiphase Sacramento porphyritic

granitic intrusion of Jurassic age. Motivation for this study is the lack of district-scale mineralogical work on Bisbee, and the often-conflicting results of earlier studies. Ore petrography was used to investigate paragenetic relationships within and between ore types, and EPMA was used to measure mineral chemistry, especially of tennantite-tetrahedrite and sphalerite. The goal was to establish a district-wide paragenesis of hypogene ores and interpret changes in mineralogy and mineral chemistry in terms of time and space within the Bisbee district, and compare Bisbee to other polymetallic lode districts worldwide.

Bisbee ores are dominated by either Cu or Zn-Pb, and can further be divided into chalcopyrite-rich ore, bornite-rich ore, chalcocite-rich ore, and a Zn-Pb association. Ore types contain distinct accessory mineralogy: chalcopyrite-rich ore contains Cu-Bi-sulfides, tellurides, and minor oxides of U, Sn, and W; bornite-rich ore is associated tennantite and Cu-Sn-W-V sulfides; chalcocite-rich ore contains accessory chalcostibite and tetrahedrite; and the zinc-lead association contains tennantite-tetrahedrite.

Ores are zoned at a district scale from Cu-rich ores proximal to the Sacramento complex outwards to Zn-Pb (Mn) > Cu ores restricted to the northwestern and southeastern fringes of the district. At the ore body scale, silica-pyrite cores are overprinted and surrounded by zones of bornite- and/or chalcopyrite-rich ores and a discontinuous fringe of hematite  $\pm$  magnetite with or without pyrite. Within the copper-dominant zone, the chalcocite-rich ore type is restricted to the southern portion of the district. Zinc-lead ores are found distal to and above Cu ores in individual lodes, and Mn ore is found distal to and stratigraphically above Zn-Pb ore.

Paragenetic relationships indicate magnetite + chlorite + quartz and then hematite + anhydrite + chlorite + quartz were the first minerals to replace limestone, followed by pyrite. Chalcopyrite + chlorite + quartz  $\pm$  pyrite followed pyrite, bornite + pyrite + muscovite followed chalcopyrite and local enargite, chalcocite-digenite, or covellite followed bornite. The Zn-Pb (Mn) association was deposited furthest from the sources of fluid. Small relicts of sphalerite and galena within bornite-rich ores suggest Zn-Pb ores were continuously dissolved and redeposited distal to Cu ores.

Based on the work of Einaudi (1982) and Einaudi et al. (2003) and the lack of skarn alteration, the lodes at Bisbee probably formed at relatively shallow depths (<2 km) at temperatures from <325°C to <250°C. Fluids forming early hematite-magnetite were near the SO<sub>2</sub>-H<sub>2</sub>S buffer, moderately oxidized and S-rich at relatively low sulfidation state. Later fluids were similarly S-rich, moderately oxidized but were considerably more sulfidized, forming chalcopyrite-pyrite, bornite-pyrite, digenite/covellite-pyrite, or enargite. The paragenesis and zoning indicate progressive reaction of fluids with host rocks drops sulfidation state as fluids migrate outward, leading to distal sphalerite, galena, pyrite, and hematite. These relationships, as well as mineralogy of accessory phases, are similar to worldwide polymetallic lodes such as Butte and Magma, USA, Morococha, Peru, Chuquicamata, Chile, and Elshitsa, Bulgaria.

An attempt was made to calculate temperatures of ore-forming fluids at Bisbee using Zn-Fe exchange between coexisting sphalerite and tennantite-tetrahedrite in ore using the method of O'Leary and Sack (1987) and Sack et al. (1987). This method involves the relationship between mole fraction (X) Fe and Zn in sphalerite (sph) and tennantite-tetrahedrite (tet) according to the equation:

$$RT\ln(X_{\text{Fe}}/X_{\text{Zn}})_{\text{tet}}(X_{\text{Zn}}/X_{\text{Fe}})_{\text{sph}} + RT\ln(\gamma_{\text{ZnS}}/\gamma_{\text{FeS}})_{\text{sph}} =$$

$$\Delta G^{\circ}_{\text{Zn/Fe}} + \frac{1}{2} \Delta G^{\circ}_{23}(X_2) + \frac{1}{2} \Delta G^{\circ}_{24}(X_4)$$

where R is the ideal gas constant (1.9872 cal/K mol), T is temperature in K,  $\gamma_{\text{ZnS}}$  and  $\gamma_{\text{FeS}}$  are the activity coefficients of ZnS and FeS in sphalerite,  $\Delta G^{\circ}_{\text{Zn/Fe}}$  is the molar vibrational Gibbs energy difference between Zn and Fe end-member tetrahedrite (2.07 kcal/gfw),  $\Delta G^{\circ}_{23}$  is the molar vibrational Gibbs energy difference between pure tennantite and pure tetrahedrite (2.59 kcal/gfw),  $X_2 = X_{\text{As}}/(X_{\text{As}} + X_{\text{Sb}})$ ,  $\Delta G^{\circ}_{24}$  is the difference in molar vibrational Gibbs energy of pure  $\text{Cu}_{10}\text{Zn}_2(\text{As,Sb})_4\text{S}_{13}$  and  $\text{Ag}_6\text{Cu}_4\text{Zn}_2(\text{As,Sb})_4\text{S}_{13}$ , and  $X_4 = 3/5 \text{ Ag}/(\text{Ag}+\text{Cu})$ . For Ag free tennantite-tetrahedrite,  $X_4$  is 0. Solving for temperature gives  $T = 1041.6667 + 742.25(X_2)/\ln(X_{\text{Fe/Zn,tet}} * X_{\text{Zn/Fe, sph}}) - \ln(\gamma_{\text{ZnS}}/\gamma_{\text{FeS}})_{\text{sph}}$ .

The ratio of activity coefficients,  $\ln(\gamma_{\text{ZnS}}/\gamma_{\text{FeS}})$ , is calculated using the mole fraction of Fe in sphalerite:  $\ln(\gamma_{\text{ZnS}}/\gamma_{\text{FeS}})_{\text{sph}} = 0.7285 - 0.9186(X_{\text{FeS}}) - 0.5295(X_{\text{FeS}})^2 - 0.1772(X_{\text{FeS}})^3$ .

Results were mixed, with temperatures ranging from 270 K (-2°C) to 597.5 K (324.5°C). Out of four samples, only two gave reasonable temperature estimates of 301°C and 324°C: a sphalerite-galena sample and a bornite sample, respectively, both from the Campbell shaft. The unlikely temperature results came from samples containing tennantite-tetrahedrite grains zoned by Zn-Fe, As-Sb-Te, or both, in association with unzoned sphalerite. Redoing calculations by zone gave similarly unlikely results.

## KEY FINDINGS

In the mineralogical portion of this study, I describe natropalermoite, a mineral new to science, and explain how the accommodation of Na versus Li leads to an elongation of the *b* unit cell axis versus that of palermoite by narrowing the angle between the two

octahedra in the  $\text{Al}_2\text{O}_7(\text{OH})_3$  dimer and consequently causing a shortening of the a and c axes to accommodate this change in angle.

Single-crystal X-ray diffraction and electron microprobe studies of two skutterudite and two nickelskutterudite samples establish that skutterudite-group minerals are not anion deficient, and in fact contain a cation surplus accommodated at the icosahedral cation site. The observed occupancy of the icosahedral site is the first example of this phenomenon in natural skutterudites. Essential Co and Fe seen in nickelskutterudite, along with the fully occupied anion site, lead to the proposed (and accepted) change in chemical formula to  $(\text{Ni},\text{Co},\text{Fe})\text{As}_3$ .

Secondary copper sulfides in the supergene blanket at Morenci formed from as few as one to as many as three periods of supergene activity. The overall  $(\text{Cu}+\text{Fe}):\text{S}$  ratio decreases with depth and is interpreted to have been caused by decreasing activity of Cu and Fe ionic species in solution. In terms of ore processing, the upper blanket is mostly leach material and the lower blanket is mostly mill feed, with important exceptions. Much of the leach material contains low Cu:S phases, which will leach poorly and negatively impact leach recoveries.

At Bisbee, ores exhibit a district-wide paragenesis from early Zn-Pb to later Cu mineralization. In addition to the previously identified chalcopyrite-rich ores and bornite-rich ores, I identified a chalcocite-rich ore restricted to the southern portion of the district. Ore forming fluids were oxidized and S-rich. Earlier fluids were higher temperature and lower sulfidation state, responsible for magnetite, hematite, and chlorite, while later fluids were lower temperature and considerably higher sulfidation state, responsible for forming pyrite, chalcopyrite, bornite, and chalcocite. Sulfidation state increased at any

given point within an orebody as time progressed. Zinc-lead ores were continuously dissolved and redeposited distal to Cu ores throughout the life of the hydrothermal system at Bisbee.

## REFERENCES

- Aleksandrov, K.S., and Beznosikov, B.V., 2007, Crystal Chemistry and Prediction of Compounds with a Structure of Skutterudite Type. *Kristallografiya*, 52:1, 32-40.
- Anderson, J.A., 1982, Leached capping and techniques of appraisal, in Titley, S.R., ed. *Advances in geology of the porphyry copper deposits, southwestern North America*: Tucson, University of Arizona Press, p. 275-295.
- Catchpole, H., Kouzmanov, K., Fontboté, L., 2012, Copper-excess stannoidite and tennantite-tetrahedrite as proxies for hydrothermal fluid evolution in a zoned Cordilleran base metal district, Morococha, Central Peru. *Economic Geology*, 50, 719-743.
- Chakoumakos, B.C., and Sales, B.C., 2006, Skutterudites: Their structural response to filling. *Journal of Alloys and Compounds*, 407, 87-93.
- Criddle, A.J., Stanley, C.J., Eady, C.S., 1982, Ore mineralization of the Campbell orebody, Bisbee, Arizona. Unpublished report, Freeport McMoRan files.
- Einaudi, M.T., 1982, Skarns associated with porphyry copper plutons, I. Description of deposits, southwestern U.S., II. General features and origin, in Titley, S.R., ed., *Advances in geology of the porphyry copper deposits, southwestern North America*: Tucson, University of Arizona Press, pp. 139-183.
- Einaudi, M.T., Hedenquist, J.W., Inan, E.E., 2003, Sulfidation state of fluids in active and extinct hydrothermal systems: transitions from porphyry to epithermal environments. *Special Publication-Society of Economic Geologists*, 10, 285-314.
- Goble, R.J., Smith, D.G.W., 1973, Electron microprobe investigation of copper sulfides in the Precambrian Lewis Series of S.W. Alberta, Canada. *Canadian Mineralogist* 12, 95-103.

- Hiskey, J.B., Wadsworth, M.E., 1981, Electrochemical processes in the leaching of metal sulfides and oxides. *Journal of Macromolecular Science-Physics*, 303-325.
- Lang J., Thompson J., Mortensen J., Baker T., Coulson I., Duncan R., Maloof T., James J., Friedman R., Leprite M., 2001, The Arizona porphyry province, *in* Lang, J., ed., *Regional and System-Scale Controls on the Formation of Copper and/or Gold Magmatic-Hydrothermal Mineralization*, p. 53-76. The Mineral Deposit Research Unit, The University of British Columbia, British Columbia.
- O'Leary, M.J., and Sack, R.O., 1987, Fe-Zn exchange reaction between tetrahedrite and sphalerite in natural environments. *Contributions in Mineralogy and Petrology*, 96, 415-425.
- Page, J.J. and Larrabee, D.M., 1962, Beryl resources of New Hampshire. *United States Geological Survey Professional Paper 353*, 49 pp.
- Sack, R.O., Ebel, D.S., O'Leary, M.J., 1987, Tennahedrite thermochemistry and metal zoning, *in* Helgeson, H.C. (ed.), *Chemical transport in metasomatic processes*. Springer Netherlands, 701-731.
- Schwartz, G.M., Park, C.F., Jr., 1932, A microscopic study of ores from the Campbell mine, Bisbee, Arizona. *Economic Geology*, 26, 39-51.
- Seedorff, E., Dilles, J.H., Proffett, J.M. Jr., Einaudi, M.T., Zurcher, L., Stavast, W.J.A., Johnson, D.A., Barton, M.D., 2005, Porphyry Copper Deposits: Characteristics and Origin of Hypogene Features. *Econ. Geol. 100<sup>th</sup> Anniversary Volume*, 251-298.
- Segeler, C.G., Ulrich, W., Kampf, A.R. and Whitmore, R.W., 1981, Phosphate minerals of the Palermo No. 1 pegmatite. *Rocks and Minerals*, **56**, 197-214

- Sillitoe, R.H., 2005, Supergene oxidized and enriched porphyry copper and related deposits: Economic Geology 100<sup>th</sup> Anniversary Volume, 723-768.
- Sillitoe, R.H., Clark, A.H., 1969, Copper and copper-iron sulfides as the initial products of supergene oxidation, Copiapó mining district, northern Chile. American Mineralogist 54, 1684-1710.
- Tenney, J.B., 1913, Unpublished report on 2,200 hand specimen and thin section determinations. Freeport McMoRan files.
- Titley, S.R., Mazonras, D.C., 1995, Processes and products of supergene copper enrichment: Arizona Geological Society Digest 20, 156-168.
- Walsh, C.A., Rimstidt, J.D., 1986, Rates of reaction of covellite and blaubleibender covellite with ferric iron at pH 2.0. Canadian Mineralogist 24, 35-44.

**APPENDIX A: NATROPALERMOITE,  $\text{Na}_2\text{SrAl}_4(\text{PO}_4)_4(\text{OH})_4$ , A NEW MINERAL  
ISOSTRUCTURAL WITH PALERMOITE, FROM THE PALERMO NO. 1  
MINE, GROTON, NEW HAMPSHIRE, USA**

This paper was accepted for publication in *Mineralogical Magazine* in August, 2017.

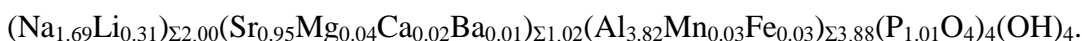
Benjamin N. Schumer, Hexiong Yang and Robert T. Downs

*Department of Geosciences, University of Arizona, 1040 E 4th Street, Tucson, AZ 85721-0077, USA*

Schumer, B.N., Yang, H., and Downs, R.T. (In Press) Natropalermoite,  $\text{Na}_2\text{SrAl}_4(\text{PO}_4)_4(\text{OH})_4$ , a new mineral isostructural with palermoite, from the Palermo No. 1 mine, Groton, New Hampshire, USA. *Mineralogical Magazine*, **80**.

## ABSTRACT

Natropalermoite, ideally  $\text{Na}_2\text{SrAl}_4(\text{PO}_4)_4(\text{OH})_4$ , the Na-analogue of palermoite, is a new mineral from the Palermo No. 1 mine, Groton, New Hampshire, USA. Associated minerals are palermoite, eosphorite, and quartz. Natropalermoite crystals are prismatic with striations parallel to the direction of elongation (the  $a$  axis) up to  $200 \times 50 \times 45 \mu\text{m}$  in size. The mineral is colorless, transparent with white streak and vitreous luster and is visually indistinguishable from palermoite. It is brittle with subconchoidal fracture and has a Mohs hardness of 5.5. Cleavage is perfect on  $\{001\}$ , fair on  $\{100\}$  and no parting was observed. The calculated density is  $3.502 \text{ g/cm}^3$ . Natropalermoite is biaxial (-),  $\alpha = 1.624(1)$ ,  $\beta = 1.641(1)$ ,  $\gamma = 1.643(1)$  (589 nm),  $2V_{\text{meas}} = 43(4)^\circ$ ,  $2V_{\text{calc}} = 38^\circ$ . An electron microprobe analysis yielded an empirical formula (based on 20 O apfu) of



Natropalermoite is orthorhombic, space group *Imcb*,  $a = 11.4849(6)$ ,  $b = 16.2490(7)$ ,  $c = 7.2927(4) \text{ \AA}$ ,  $V = 1360.95(17) \text{ \AA}^3$ ,  $Z = 4$ . Natropalermoite is isotypic with palermoite, but substitution of larger Na for Li results in substantial increase of the  $b$  cell parameter. Four of the seven Na-O distances are longer than their equivalents in palermoite, resulting in a more regular 7-fold coordination polyhedron about Na. The eight strongest peaks in the calculated X-ray powder diffraction are [ $d_{\text{calc}}(\text{\AA})$ ,  $I_{\text{rel}}\%$ , ( $hkl$ )]: [3.128, 100, (321)], [4.907, 68, (121)], [3.327, 48, (022)], [4.689, 45, (220)], [3.078, 45, (202)], [2.453, 38, (242)], [2.636, 35, (411)], [2.174, 35, (422)].

## INTRODUCTION

A new mineral species, natropalermoite, ideally  $\text{Na}_2\text{SrAl}_4(\text{PO}_4)_4(\text{OH})_4$ , was found in a sample from the Palermo No. 1 mine, Groton, New Hampshire. The name reflects the presence of sodium (natrium) and the structural isomorphism to palermoite. The new

mineral and its name have been approved by the Commission on New Minerals, Nomenclature and Classification (CNMNC) of the International Mineralogical Association (IMA 2013-118). The holotype sample is deposited in the collections of the Mineral Museum of the University of Arizona, Tucson, Arizona, USA, catalogue number 19735, and the RRUFF Project, deposition number R130092. This paper describes the physical and chemical properties of natropalermoite and the characterization of the structure based on single-crystal X-ray diffraction data.

## SAMPLE DESCRIPTIONS AND EXPERIMENTAL METHODS

### *Occurrence, physical and chemical properties, and Raman spectra*

Natropalermoite was found in a sample from the Palermo No. 1 mine, Groton, Grafton County, New Hampshire, USA which exploited a complex, phosphate-bearing granite pegmatite for mica, feldspar, and beryl (Cameron *et al.* 1954, Page and Larrabee 1962). Associated minerals include palermoite, childrenite, lefontite, mixed iron oxides, and quartz (Fig. 1). Natropalermoite is of secondary origin, formed as a result of hydrothermal alteration of primary triphylite pods in the core-margin zone of the pegmatite (Page and Larrabee 1962, Segeler *et al.* 1981). Palermoite in association with natropalermoite shows cores of near end-member composition with rims higher in Na, indicating natropalermoite forms later than palermoite. The Palermo No. 1 mine was brought into the mineralogical spotlight by the host of secondary phosphate phases found there, and is the type locality for twelve phosphate species, not including natropalermoite: palermoite, whitlockite, goedkenite, schoonerite, bjarebyite, whitmoreite, wolfeite, xanthoxenite, foggite, samuelsonite, falsterite, and nizamoffite (Kampf *et al.* 2013 and references therein).

Natropalermoite crystals are prismatic, up to 200 x 50 x 45  $\mu\text{m}$  in size, elongated and striated along the  $a$  axis (Fig. 2). In transmitted light, natropalermoite is colorless and transparent, with a vitreous luster. It is brittle, has perfect cleavage on  $\{001\}$ , fair on  $\{100\}$  and no parting was observed. Fracture is sub-conchoidal to fibrous. Hardness was not measured but is most likely 5.5 by analogy with palermoite. Natropalermoite is non-pleochroic, biaxial (-),  $\alpha = 1.624(1)$ ,  $\beta = 1.641(1)$ ,  $\gamma = 1.643(1)$  (589 nm),  $2V_{\text{meas}} = 43(4)^\circ$ ,  $2V_{\text{calc}} = 38^\circ$ , dispersion  $v > r$ , medium to weak. Because of the paucity of crystals, no density was measured. The calculated density is 3.502  $\text{g}/\text{cm}^3$ .

Natropalermoite is insoluble in water and acetone.

The chemical composition of natropalermoite was determined using a CAMECA SX100 electron microprobe with beam conditions of 15 kV, 4 nA, and 5  $\mu\text{m}$  beam diameter. Standards used were K-feldspar for Al, albite for Na, synthetic apatite for Ca and P, synthetic  $\text{SrTiO}_3$  for Sr, rhodonite for Mn, forsterite for Mg, fayalite for Fe, and baryte for Ba. The presence of OH was confirmed by both structural determination and Raman spectroscopic measurements (see below), and the amount of OH was estimated by stoichiometry from the crystal structure refinement. Not enough material was available for the direct determination of  $\text{Li}_2\text{O}$ , which was estimated by stoichiometry from the crystal structure refinement. An average of 10 spot analyses (Table 1) yielded an empirical formula of

$(\text{Na}_{1.69}\text{Li}_{0.31})_{\Sigma 2.00}(\text{Sr}_{0.95}\text{Mg}_{0.04}\text{Ca}_{0.02}\text{Ba}_{0.01})_{\Sigma 1.02}(\text{Al}_{3.82}\text{Mn}_{0.03}\text{Fe}_{0.03})_{\Sigma 3.88}(\text{P}_{1.01}\text{O}_4)_4(\text{OH})_4$  based on 20 O atoms per formula unit, which can be simplified to  $\text{Na}_2\text{SrAl}_4(\text{PO}_4)_4(\text{OH})_4$ .

The Raman spectrum of natropalermoite was collected from a randomly oriented crystal on a Thermo Almega microRaman system, using a 532-nm solid-state laser with a

thermoelectric cooled CCD detector. The laser is partially polarized with  $4 \text{ cm}^{-1}$  resolution and a spot size of  $1 \text{ }\mu\text{m}$ .

### *X-ray crystallography*

Because of the paucity of material, X-ray powder diffraction data of natropalermoite (Table 2) were calculated from the determined structure using the program XPOW (Downs et al. 1993).

Single-crystal X-ray diffraction data (Table 2) of natropalermoite were collected using a Bruker X8 APEX2 CCD diffractometer equipped with graphite-monochromatized  $\text{MoK}\alpha$  radiation, with frame widths of  $0.5^\circ$  in  $\omega$  and 30 s counting time per frame. All reflections were indexed based on an orthorhombic unit cell. The intensity data were corrected for X-ray absorption using the Bruker program SADABS. SHELX97 (Sheldrick 2008) was used for structure determination and refinement. The final crystal structure was solved and refined with space group *Imcb* resulting in  $R_1 = 0.021$ ,  $wR_2 = 0.0564$  for 1257 reflections with  $F_o > 4\sigma(F_o)$ . Final atom positions, occupancies and isotropic and anisotropic displacement parameters are given in Table 4, and selected bond distances are given in Table 5. For the refinement, site occupancies were refined for sites Sr and Na to account for substitution of Ca for Sr and Li for Na, respectively, ignoring other trace elements. The refinement showed 0.04 Ca apfu replacing Sr and 0.05 apfu Li replacing Na, compared to 0.02 apfu Ca measured and 0.16 apfu Li estimated from the microprobe analysis.

## DISCUSSION

### *Crystal Structure*

Natropalermoite,  $\text{Na}_2\text{SrAl}_4(\text{PO}_4)_4(\text{OH})_4$ , is isostructural with palermoite,  $\text{Li}_2\text{SrAl}_4(\text{PO}_4)_4(\text{OH})_4$ , the structure of which was described by Moore and Araki (1975). The natropalermoite structure contains five non-H cation sites: one each for  $\text{Sr}^{2+}$ ,  $\text{Na}^+$ ,  $\text{Al}^{3+}$ , and two for  $\text{P}^{5+}$  (P1 and P2), and two non-equivalent H atoms. The crystal structure of natropalermoite is shown in Fig. 3. Two  $\text{AlO}_4(\text{OH})_2$  octahedra form edge-sharing  $\text{Al}_2\text{O}_7(\text{OH})_3$  dimers. These dimers are corner-linked to one another through (OH)<sub>2</sub>, forming infinite zigzag chains along [100] (Fig. 4). The chains themselves are hexagonal closest-packed, accounting for the pseudo-hexagonal prismatic morphology of the crystals. The zigzag chains are interconnected by  $\text{PO}_4$  groups, which share all four O atoms with Al. Na and Sr atoms are 7- and 8-coordinated, respectively, and are located in two distinct types of channels parallel to [100]. When viewed along [100], the Na atoms are staggered within their respective channels, forming a “double-stack” arrangement, while the Sr atoms are “single-file” (Fig. 3). Most remarkably, due to the substitution of Na for Li, the unit cell *b* dimension of natropalermoite is significantly longer than that of palermoite: the larger Na atoms increase the width of their accommodating channels in the [010] direction, lengthening the overall *b* dimension of the unit cell. As the channels widen along [010], the angle between the two octahedra in the  $\text{Al}_2\text{O}_7(\text{OH})_3$  dimer narrows, resulting in the shortening of the  $a = 11.4849(6)$  and  $c = 7.2927(4)$  Å dimensions of natropalermoite versus those of palermoite:  $a = 11.577(1)$  and  $c = 7.3276(7)$  Å. The *b* cell edge is the distinguishing crystallographic parameter which can be used to differentiate natropalermoite from palermoite.

The position of the H1 atom was determined during the structure refinement, indicating the presence of OH in natropalermoite. H1 is bonded to O-H1, which is one of the two atoms in the shared edge of the  $\text{Al}_2\text{O}_7(\text{OH})_3$  dimer. Coordinates for the second H2 atom could not be refined, however valence considerations point to O-H2, the bridging atom linking dimers. The average position of atom H2 was assumed to be  $x = 0.25$ ,  $y = \sim 0.47$ ,  $z = 0$ . This position must represent an average because O-H2, which links two  $\text{AlO}_6$  octahedra, undergoes considerable libration, demonstrated by its elongated displacement ellipsoid, oriented perpendicular to the Al-O-Al plane (Fig 5), making it extremely difficult to observe the electron density associated with the H2 atom.

Natropalermoite is structurally related to carminite,  $\text{PbFe}^{3+}_2(\text{AsO}_4)_2(\text{OH})_2$ . The structures of natropalermoite and carminite contain the same zig-zag chain of  $M_2\text{O}_7(\text{OH})_3$  edge-sharing dimers linked by OH2, with individual chains interconnected by  $\text{TO}_4$  tetrahedra (Moore and Araki 1975). The difference between natropalermoite and carminite lies in accommodation of Na in natropalermoite. Two equivalent Na atoms of site-symmetry  $m$  in natropalermoite take the place of the single Pb2 atom of site-symmetry  $2/m$  in carminite. For a detailed comparison between palermoite and carminite, see Moore and Araki (1975).

### *Raman Spectroscopy*

The Raman spectrum of a natropalermoite crystal in unknown orientation is shown in Fig. 6. The band at  $3215\text{ cm}^{-1}$  can be attributed to O-H stretching vibrations. Bands between  $1142\text{ cm}^{-1}$  and  $524\text{ cm}^{-1}$  are interpreted as P-O stretching and bending vibrations. Bands between  $295$  and  $462\text{ cm}^{-1}$  are interpreted as metal-oxygen stretching vibrations. The broad bands below  $295\text{ cm}^{-1}$  are interpreted as translational lattice

vibrations. The Raman spectra of natropalermoite and palermoite are virtually indistinguishable (Fig. 7).

## REFERENCES

- Cameron, E.N., Larrabee, D.M., McNair, A.H., Page, J.J., Stewart, G.W. and Shainin, V.E. (1954) Pegmatite investigations, 1942-45, New England. *United States Geological Survey Professional Paper 225*, 352 pp.
- Downs, R.T., Bartelmehs, K.L., Gibbs, G.V. and Boisen, M.B., Jr. (1993) Interactive software for calculating and displaying X-ray or neutron powder diffractometer patterns of crystalline materials. *American Mineralogist*, **78**, 1104-1107.
- Kampf, A.R., Falster, A.U., Simmons, W.B., Whitmore, R.B. (2013) Nizamoffite,  $\text{Mn}^{2+}\text{Zn}_2(\text{PO}_4)_2(\text{H}_2\text{O})_4$ , the Mn analogue of hopeite from the Palermo No. 1 pegmatite, North Groton, New Hampshire. *American Mineralogist*, **98**, 1893-1898.
- Moore, P.B. and Araki, T. (1975) Palermoite,  $\text{SrLi}_2[\text{Al}_4(\text{OH})_4(\text{PO}_4)_4]$ : its atomic arrangement and relationship to carminite,  $\text{Pb}_2[\text{Fe}_4(\text{OH})_4(\text{AsO}_4)_4]$ . *American Mineralogist*, **60**, 460-465.
- Page, J.J. and Larrabee, D.M. (1962) Beryl resources of New Hampshire. *United States Geological Survey Professional Paper 353*, 49 pp.
- Segeler, C.G., Ulrich, W., Kampf, A.R. and Whitmore, R.W. (1981) Phosphate minerals of the Palermo No. 1 pegmatite. *Rocks and Minerals*, **56**, 197-214
- Sheldrick, G.M. (2008) A short history of *SHELX*. *Acta Crystallographica* **A64**, 112-122.

## FIGURE CAPTIONS

Figure 1. The sample on which natropalermoite was found.

Figure 2. Prismatic crystal of natropalermoite growing on grayish brown childrenite.

Note weak striations parallel to the axis of elongation  $a$ . The top portion of this crystal was used for X-ray, chemistry, and optical data collection.

Figure 3. The crystal structure of natropalermoite, viewed along [100]. Grey, golden, sky blue, and blue spheres represent Na, Sr, OH and H respectively. Orange tetrahedra are  $\text{PO}_4$  groups and cerulean octahedra are  $\text{AlO}_6$  groups.

Figure 4. The zigzag chain of  $\text{Al}_2\text{O}_7(\text{OH})_3$  dimers, looking down [010], [100] is horizontal. Cerulean octahedra are  $\text{AlO}_6$  octahedra, red spheres represent O-H1, while light blue spheres represent the OH2 group.

Figure 5. Al dimer, with each atom shown as an ellipsoid of 99.999% probability. In particular note the elongated O-H2 ellipsoid indicating significant libration in the direction perpendicular to the Al-O-Al plane. The H2 position is the average likely position that must also have significant motion related to riding on O-H2 and repulsion from its neighboring H2 atom.

Figure 6. Raman spectrum of natropalermoite, showing acoustic and optical modes (left) and a broad band at  $3215\text{ cm}^{-1}$  attributed to O-H stretching.

Figure 7. The Raman spectrum of natropalermoite (bottom) compared with that of palermoite.

## FIGURES

Figure 1



Figure 2

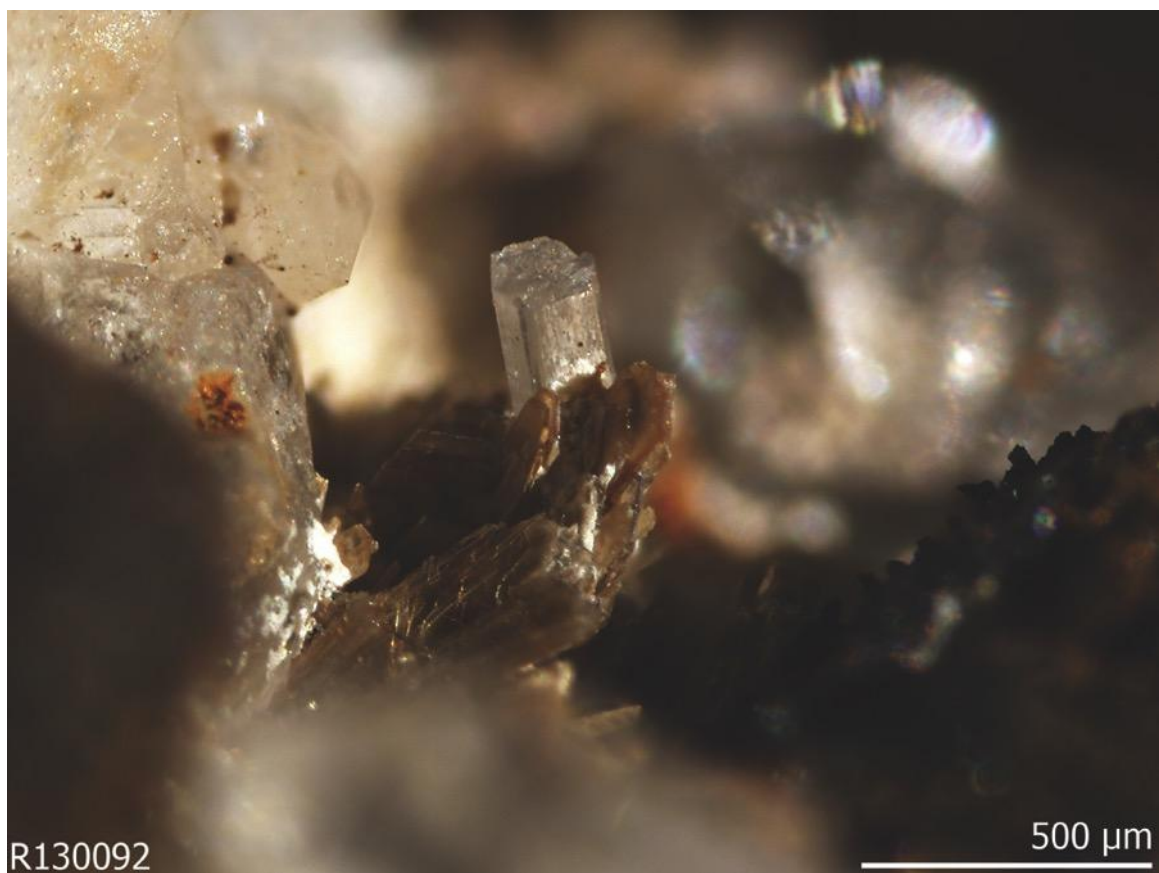


Figure 3

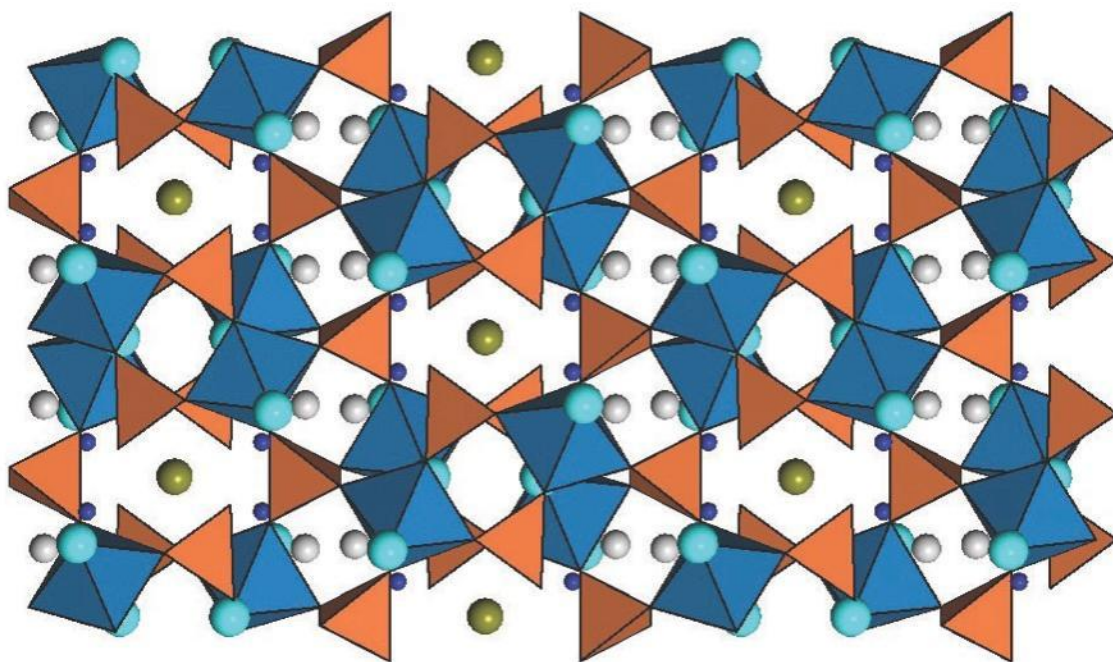


Figure 4

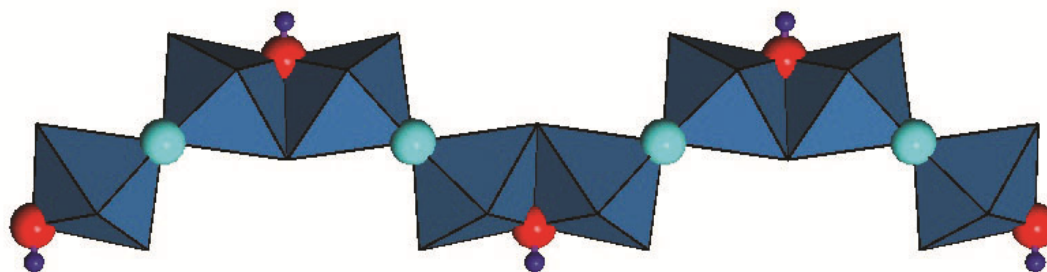


Figure 5

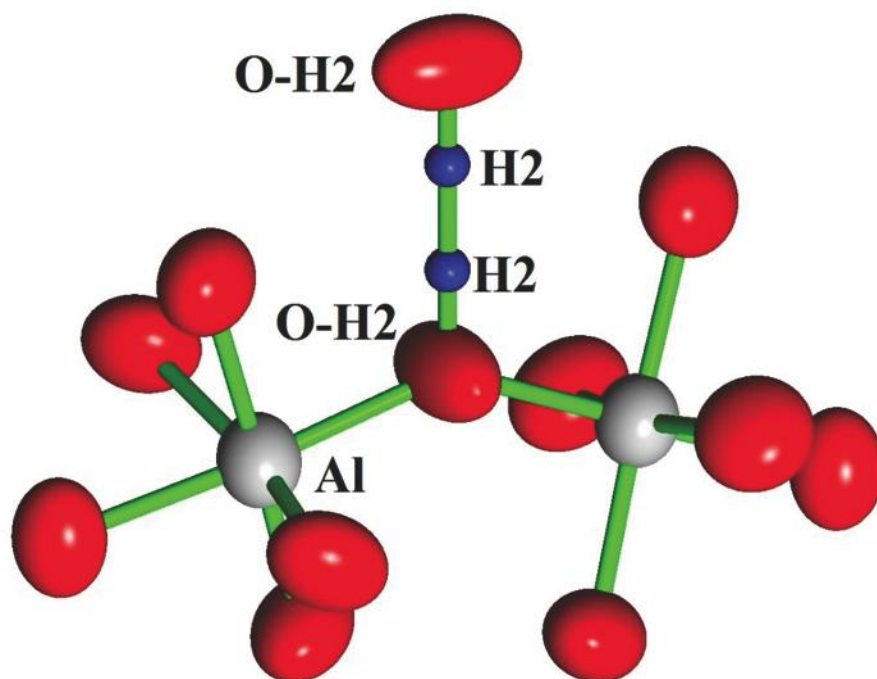


Figure 6

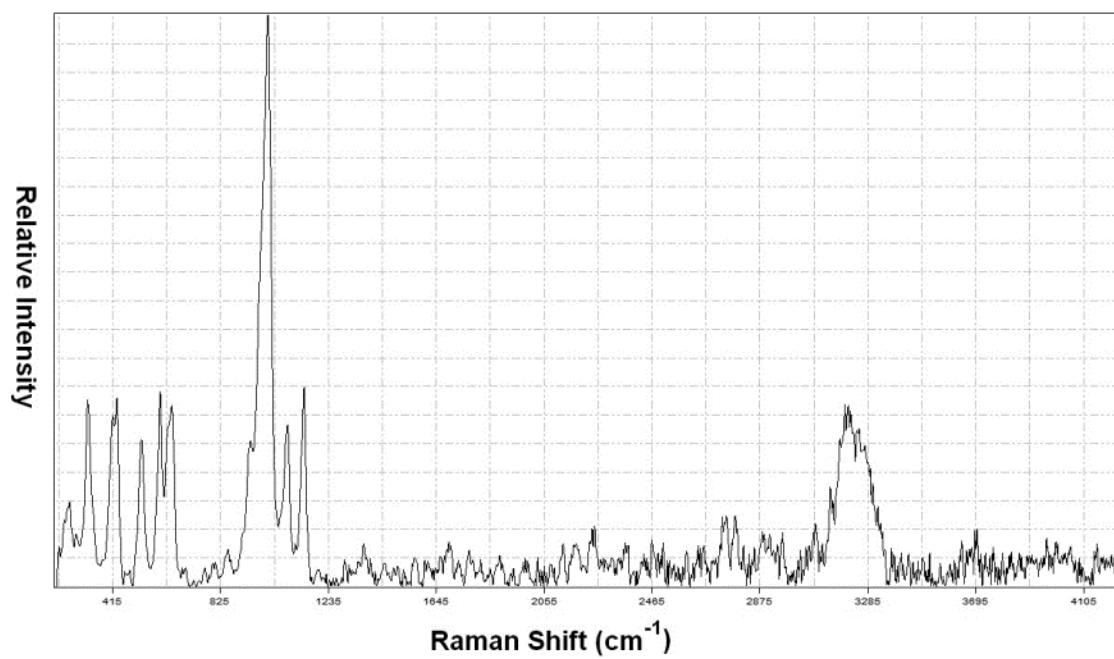
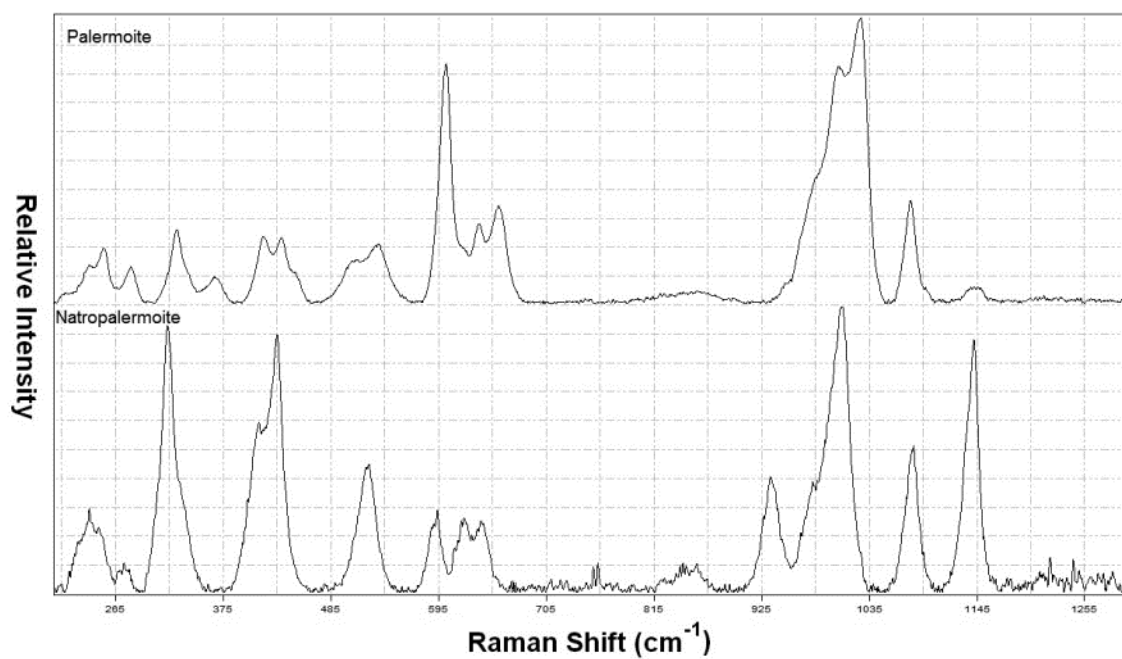


Figure 7



## TABLE EXPLANATORY NOTES

Table 1. Microprobe data for natropalermoite, standard deviation in weight percent are indicated by numbers in parenthesis.

Table 2. Summary of crystal data and refinement results for natropalermoite .

Table 3. Calculated X-ray powder diffraction data for natropalermoite including lines of intensity >12 only.

Table 4. Coordinates and displacement parameters for natropalermoite. Assumed average position of H2 is included for completeness.

Table 5. Selected bond distances in natropalermoite.

## TABLES

Table 1

Constituent	wt%	Range	Probe Standard
Al <sub>2</sub> O <sub>3</sub>	28.6(2)	28.39-28.95	K-feldspar
Mn <sub>2</sub> O <sub>3</sub>	0.36(9)	0.17-0.50	Rhodonite
Fe <sub>2</sub> O <sub>3</sub>	0.35(4)	0.31-0.41	Fayalite
Na <sub>2</sub> O	7.68(10)	7.56-7.87	Albite
Li <sub>2</sub> O	0.69		*
MgO	0.26(3)	0.22-0.31	Forsterite
CaO	0.16(4)	0.11-0.20	Apatite, synthetic
SrO	14.5(4)	14.23-15.29	SrTiO <sub>3</sub>
BaO	0.14(4)	0.10-0.21	Barite
P <sub>2</sub> O <sub>5</sub>	42.28(13)	42.06-42.46	Apatite, synthetic
H <sub>2</sub> O	5.29		*
Total	100.29		

\*Note: Estimated from structure refinement stoichiometry.

Table 2

Natropalermoite (R130092, New Hampshire)	
IMA-defined chemical formula	$\text{Na}_2\text{SrAl}_4(\text{PO}_4)_4(\text{OH})_4$
Effective structural formula	$(\text{Na}_{1.69}\text{Li}_{0.31})_{\Sigma 2.00}(\text{Sr}_{0.95}\text{Mg}_{0.04}\text{Ca}_{0.02}\text{Ba}_{0.01})_{\Sigma 1.02}(\text{Al}_{3.82}\text{Mn}_{0.03}\text{Fe}_{0.03})_{\Sigma 3.88}(\text{P}_{1.01}\text{O}_4)_4(\text{OH})_4$
Space group	<i>Imcb</i>
<i>a</i> (Å)	11.4849(6)
<i>b</i> (Å)	16.2490(7)
<i>c</i> (Å)	7.2927(4)
<i>V</i> (Å <sup>3</sup> )	1360.95(17)
<i>Z</i>	4
$\rho_{\text{calc}}$ (g/cm <sup>3</sup> )	3.328
$\lambda$ (Å)	0.71073
$\mu$ (mm <sup>-1</sup> )	4.73
$2\theta$ range for data collection	<65.19°
No. of reflections collected	5970
No. of independent reflections	1257
No. of reflections with $I > 2\sigma(I)$	1132
No. of parameters refined	86
R(int)	0.0271
Final $R_1$ , $wR_2$ factors [ $I > 2\sigma(I)$ ]	0.0207, 0.0564
Final $R_1$ , $wR_2$ factors (all data)	0.0252, 0.0564
Goodness-of-fit	1.034

Table 3

$I_{\text{rel}}$	$d_{\text{calc}}$	$h$	$k$	$l$
33	6.653	0	1	1
14	5.743	2	0	0
<b>68</b>	<b>4.907</b>	<b>1</b>	<b>2</b>	<b>1</b>
<b>45</b>	<b>4.689</b>	<b>2</b>	<b>2</b>	<b>0</b>
20	4.347	2	1	1
32	3.399	1	1	2
<b>48</b>	<b>3.327</b>	<b>0</b>	<b>2</b>	<b>2</b>
<b>100</b>	<b>3.128</b>	<b>3</b>	<b>2</b>	<b>1</b>
<b>45</b>	<b>3.078</b>	<b>2</b>	<b>0</b>	<b>2</b>
17	2.968	0	5	1
19	2.637	2	5	1
<b>35</b>	<b>2.636</b>	<b>4</b>	<b>1</b>	<b>1</b>
21	2.606	3	1	2
22	2.479	1	6	1
<b>38</b>	<b>2.453</b>	<b>2</b>	<b>4</b>	<b>2</b>
24	2.396	4	3	1
27	2.171	0	6	2
<b>35</b>	<b>2.174</b>	<b>4</b>	<b>2</b>	<b>2</b>
17	2.031	0	8	0
13	1.843	4	1	3
31	1.663	0	4	4
15	1.658	4	8	0
15	1.611	4	5	3

Table 4

Atom	<i>x</i>	<i>y</i>	<i>z</i>	$U_{eq}$	Occ. (<1)	$U^{11}$	$U^{22}$	$U^{33}$	$U^{12}$	$U^{13}$	$U^{23}$
Sr	0.25	0.5	0.5	0.01173 (10)	0.962(4)	0.01685 (17)	0.01113 (15)	0.00722 (14)	0	0	0
Ca	0.25	0.5	0.5	0.01173 (10)	0.038(4)	0.01685 (17)	0.01113 (15)	0.00722 (14)	0	0	0
Li	0.5	0.28990 (6)	0.24295 (14)	0.0185 (3)	0.047(6)	0.0322 (7)	0.0071 (5)	0.0162 (5)	0	0	0.0013 (3)
Na	0.5	0.28990 (6)	0.24295 (14)	0.0185 (3)	0.953(6)	0.0322 (7)	0.0071 (5)	0.0162 (5)	0	0	0.0013 (3)
P1	0.25	0.28936 (3)	0.5	0.00567 (12)		0.0051 (2)	0.0057 (2)	0.0062 (2)	0	0.00005 (16)	0
P2	0	0.46228 (3)	0.76986 (7)	0.00647 (12)		0.0077 (2)	0.0063 (2)	0.0054 (2)	0	0	-0.00014 (16)
Al	0.13198 (4)	0.37236 (3)	0.13801 (6)	0.00707 (11)		0.0054 (2)	0.0074 (2)	0.0084 (2)	-0.00058 (14)	0.00156 (15)	-0.00068 (14)
O1	0.14274 (9)	0.26571 (7)	0.03332 (14)	0.0092 (2)		0.0069 (5)	0.0080 (5)	0.0128 (5)	0.0010 (3)	0.0001 (4)	-0.0018 (4)
O2	0.22871 (9)	0.34742 (7)	0.33754 (14)	0.0094 (2)		0.0096 (5)	0.0106 (5)	0.0080 (5)	-0.0011 (4)	-0.0012 (4)	0.0028 (4)
O3	0	0.40980 (10)	0.6008 (2)	0.0141 (3)		0.0210 (8)	0.0141 (7)	0.0073 (7)	0	0	-0.0034 (5)
O4	0	0.40464 (9)	0.9440 (2)	0.0101 (3)		0.0156 (8)	0.0078 (7)	0.0070 (6)	0	0	0.0014 (5)
O5	0.11018 (9)	0.48323 (7)	0.22553 (14)	0.0091 (2)		0.0067 (5)	0.0093 (4)	0.0111 (5)	0.0000 (3)	0.0000 (4)	-0.0001 (4)
O-H1	0	0.34231 (9)	0.2617 (2)	0.0074 (3)		0.0066 (6)	0.0096 (6)	0.0059 (6)	0	0	0.0002 (5)
O-H2	0.25	0.41142 (11)	0	0.0124 (3)		0.0149 (8)	0.0089 (7)	0.0136 (7)	0	0.0085 (6)	0
H1	0	0.359 (3)	0.376 (5)	0.037 (10)							
H2*	0.25	0.47	0								

\*Assumed average position of H2

**APPENDIX B: A NEW FORMULA AND CRYSTAL STRUCTURE FOR  
NICKELSKUTTERUDITE, (Ni,Co,Fe)As<sub>3</sub>, AND OCCUPANCY OF THE  
ICOSAHEDRAL CATION SITE IN THE SKUTTERUDITE GROUP**

This paper was published in *American Mineralogist*, January, 2017.

Benjamin N. Schumer<sup>a</sup>, Marcelo B. Andrade<sup>b</sup>, Stanley H. Evans<sup>a</sup>, and Robert T. Downs<sup>a</sup>

<sup>a</sup>*Department of Geosciences, University of Arizona, 1040 E. 4th Street, Tucson, Arizona  
85721-0077, USA*

<sup>b</sup>*São Carlos Institute of Physics, University of São Paulo, Caixa Postal 369, 13560-970,  
São Carlos, SP, Brazil*

Schumer, B.N., Andrade, M.B., Evans, S.H., and Downs, R.T. (2017) A new formula and crystal structure for nickelskutterudite, (Ni,Co,Fe)As<sub>3</sub>, and occupancy of the icosahedral cation site in the skutterudite group. *American Mineralogist* **102**, 205-209.

## ABSTRACT

The crystal structure of nickelskutterudite,  $(\text{Ni,Co,Fe})\text{As}_3$ , cubic,  $Im\bar{3}$ ,  $Z = 8$ :  $a = 8.2653(6)$  Å,  $V = 564.65(7)$  Å<sup>3</sup>, has been refined to  $R_1 = 1.4\%$  for 225 unique reflections  $I > 2\sigma(I)$  collected on a Bruker X8 four-circle diffractometer equipped with fine-focus, sealed tube  $\text{MoK}\alpha$  radiation and an APEX-II CCD detector. This is the first report of the crystal structure of nickelskutterudite. Nickelskutterudite, a member of the skutterudite group of isostructural minerals, adopts a distorted perovskite structure with notably tilted octahedra and an unoccupied to partially occupied icosahedral metal site. In the structure of nickelskutterudite, there is one metal ( $B$ ) site occupied by Ni, Co, or Fe in octahedral coordination with six As atoms. Procrystal electron density analysis shows each As anion is bonded to two cations and two As anions, resulting in a four membered ring of bonded As with edges 2.547 Å and 2.475 Å. The extreme tilting of  $B\text{As}_6$  octahedra is likely a consequence of the As-As bonding. The nickelskutterudite structure differs from the ideal perovskite structure ( $A_4B_4X_{12}$ ) in that  $\text{As}_4$  anion rings occupy three of the four icosahedral cages centered on the  $A$  sites. There are reported synthetic phases isomorphous with skutterudite with the other  $A$  site completely occupied by a cation ( $AB_4X_{12}$ ).

Electron microprobe analyses of nickelskutterudite gave an empirical chemical formula of  $(\text{Ni}_{0.62}\text{Co}_{0.28}\text{Fe}_{0.12})_{\Sigma=1.02}(\text{As}_{2.95}\text{S}_{0.05})_{\Sigma=3.00}$  normalized to three anions. Pure  $\text{NiAs}_3$  nickelskutterudite, natural or synthesized, has not been reported. In nature, nickelskutterudite is always observed with significant Co and Fe, reportedly because all non-bonded valence electrons must be spin-paired. This suggests that nickelskutterudite must contain  $\text{Co}^{3+}$  and  $\text{Fe}^{2+}$ , consistent with previous models since  $\text{Ni}^{4+}$  cannot spin-pair

its seven non-bonded electrons,  $\text{Co}^{3+}$  and  $\text{Fe}^{2+}$ , which can spin-pair all non-bonded electrons, are required to stabilize the structure. No anion deficiencies were found in the course of this study so, including the structurally necessary Co and Fe, the chemical formula of nickelskutterudite (currently given as  $\text{NiAs}_{3-x}$  by the IMA) should be considered  $(\text{Ni},\text{Co},\text{Fe})\text{As}_3$ .

## INTRODUCTION

The skutterudite mineral group consists of minerals that exhibit cubic space group symmetry  $Im\bar{3}$  with ideal formula  $BX_3$  or  $B_4X_{12}$ , where  $B$  is Co, Ni, or Fe, and  $X$  is As or Sb. Skutterudite group minerals adopt a distorted perovskite structure with unoccupied  $A$  sites, constructed from a framework of tilted, corner-linked  $BX_6$  octahedra, bringing together four anions in three-quarters of the otherwise vacant icosahedral cages, where they form rectangular four member rings (Aleksandrov and Beznosikov 2007). Numerous synthetic compounds exist which are isomorphous with skutterudite group minerals, and these materials fall into two categories: (1) filled, which follow the general formula  $AB_4X_{12}$ , in which  $A$  is a large cation partially to completely occupying the remaining quarter of the icosahedral cages,  $B$  is generally a transition metal cation, and  $X$  is a P, As, or Sb anion; and (2) unfilled with the general formula  $BX_3$ . Synthetic filled skutterudite materials, such as  $\text{Tl}_{0.5}\text{Co}_4\text{Sb}_{12}$  and  $\text{NdOs}_4\text{Sb}_{12}$ , have been widely studied due to their particular thermoelectric properties including high Seebeck coefficients, high electrical conductivity, and low thermal conductivity (Aleksandrov and Beznosikov 2007; Chakoumakos and Sales 2006; Fukuoka and Yamanaka 2009; Návratil et al. 2010). We suspect that the structures of natural skutterudites can accommodate cations within the icosahedral site.

The skutterudite mineral group currently consists of four members (with current IMA formula): skutterudite ( $\text{CoAs}_{3-x}$ ), nickelskutterudite ( $\text{NiAs}_{3-x}$ ), ferroskutterudite [ $(\text{Fe},\text{Co})\text{As}_3$ ], and kieftite ( $\text{CoSb}_3$ ). The IMA nomenclature commission currently defines the chemical formula for skutterudite and nickelskutterudite as anion deficient,  $\text{BX}_{3-x}$ , after the work of Palache, Berman, and Frondel (1944). Pauling (1978) suggested that the ideal formula of skutterudite be written  $\text{Co}_4(\text{As}_4)_3$ , emphasizing the four member As rings.

The study of the skutterudite group has a long history, with skutterudite *sensu stricto* first reported by Breithaupt (1827) and its chemical composition reported as  $\text{CoAs}_3$  by Haidinger (1845). Over the course of the next century, a series of mineral species were described in order to account for the diversity of chemical compositions and physical properties exhibited by minerals related to skutterudite (Vollhardt 1888). In particular a nickel-dominant phase was described by Waller and Moses (1893) from the Bullard's Peak Mining District, Grant County, New Mexico, and more recently an iron dominant phase was described by Spridonov et al. (2007). The 7<sup>th</sup> edition of Dana's System by Palache, Berman and Frondel (1944), included a summary of the skutterudite minerals, defining them as consisting of cubic  $\text{RAs}_{3-x}$  minerals where  $R = \text{Fe}, \text{Co}$  or  $\text{Ni}$ . The IMA adopted the Palache, Berman, and Frondel (1944) anion deficient ideal chemical formulas.

$0 \leq x \leq \frac{1}{2}$		$\frac{1}{2} \leq x \leq 1$	
skutterudite	$(\text{Co},\text{Ni})\text{As}_{3-x}$	smaltite	$(\text{Co},\text{Ni})\text{As}_{3-x}$
nickel-skutterudite	$(\text{Ni},\text{Co})\text{As}_{3-x}$	chloanthite	$(\text{Ni},\text{Co})\text{As}_{3-x}$
ferrian skutterudite	$(\text{Fe},\text{Ni},\text{Co})\text{As}_{3-x}$	chathamite	$(\text{Fe},\text{Ni},\text{Co})\text{As}_{3-x}$

Ramsdell (1925) examined smaltite and chloanthite, which he considered to be isostructural members of the series  $\text{CoAs}_2\text{-NiAs}_2$ , respectively, and distinct from skutterudite. Ramsdell was, however, unable to solve the structure of either compound. Oftedal (1926) was the first to report the crystal structure of skutterudite, and two years later he compared the crystallography of skutterudite and a sample along the smaltite-chloanthite join (Oftedal 1928). The powder diffraction patterns for skutterudite and smaltite-chloanthite observed by Oftedal (1925) showed that they are isostructural, in spite of their chemical differences. Single-crystal X-ray diffraction data collected by Oftedal (1925) led him to conclude that skutterudite, and therefore smaltite-chloanthite, must follow the general formula  $R\text{As}_3$ , where  $R = \text{Co}$  or  $\text{Ni}$ . Holmes (1947) analyzed and summarized previous studies of the arsenides of cobalt, nickel, and iron, and, based on Oftedal's work, concluded that the skutterudite structure is consistent with a general formula of  $M\text{As}_3$ , but the observed compositions frequently appeared to be anion deficient. In the course of our study, it became clear that cation excess is more likely than anion deficiency in the skutterudite structure, as illustrated by the various synthetic compounds mentioned earlier.

Roseboom (1962) studied the chemical variability of the skutterudite minerals by synthesizing a series of crystals. He reported some slightly anion deficient samples, even those synthesized in the presences of elemental As, but no deficiencies large enough to account for many of the analyses of natural skutterudites (references cited in Roseboom 1962). His synthetic Co samples exhibited maximum deficiencies of  $\text{CoAs}_{2.94\text{-}2.96}$ . He concluded that excess metal replaces deficient As. As well, just as observed in the

natural samples, he could not synthesize end-member Ni or Fe skutterudite. Roseboom (1962) also concluded that the ubiquitous mixing of safflorite [(Co,Ni,Fe)As<sub>2</sub>] with skutterudite in natural samples precludes any confidence in published chemical analyses done on samples without accompanying X-ray diffraction support.

Additional structural refinements of skutterudite have been reported by Ventriglia (1957), Mandel and Donahue (1971), and Kjekshus and Rakke (1974). Ventriglia (1957) is the first to mention distortion of the CoAs<sub>6</sub> octahedra to a form that more resembles trigonal prismatic than octahedral. This distortion was confirmed by Mandel and Donahue (1971). None of these studies mention occupancy of the icosahedral site.

## EXPERIMENTAL

Four skutterudite group minerals were analyzed in this study: two nickelskutterudite samples (R100194, [ruff.info/R100194](http://ruff.info/R100194) from Schneeberg, Germany; R100196, [ruff.info/R100196](http://ruff.info/R100196) from Alhambra mine, Bullard's Peak Mining District, Grant County, New Mexico) and two skutterudite samples (R050593, [ruff.info/R050593](http://ruff.info/R050593) from Bou Azzer, Morocco; R100195, [ruff.info/R100195](http://ruff.info/R100195) from Skutterud, Norway). Chemistry was measured on a Cameca SX100 Electron Microprobe with beam conditions of 20 keV and 20 nA. Standards were NiAs (Ni and As), Co metal (Co), chalcopyrite (Fe), PbS (Pb and S), and AgBiS<sub>2</sub> (Ag and Bi). Trace Sb was detected in sample R100196 at levels slightly lower than the standard deviation, 0.007(8) weight %. Each formula was normalized to three anions. Results of the electron microprobe are given in Table 1 and discussed further below. A portion of each sample analyzed by electron microprobe was removed for structure analysis.

Single-crystal X-ray diffraction data were collected on a Bruker X8 APEX2 CCD X-ray diffractometer equipped with graphite-monochromatized  $\text{MoK}\alpha$  radiation using frame widths of  $0.5^\circ$  in  $\omega$  and 30 s counting time per frame. All reflections were indexed on the basis of a cubic unit cell. The intensity data were corrected for absorption effects by the multi-scan method using the Bruker programs TWINABS for R100196 and SADABS for the remaining samples (Bruker 2007). Crystal and refinement data for all samples are presented in Table 2.

The crystal structure of nickelskutterudite was solved and refined using SHELX97 (Sheldrick 2008) based on space group  $Im\bar{3}$  (no. 204), yielding a reliability factor  $R$  of 1.4%, from data collected on a twinned crystal ( $0.05 \times 0.05 \times 0.04$  mm) removed from R100196. The crystal is twinned according to a reflection on (110) with matrix  $0\ 1\ 0 / 1\ 0\ 0 / 0\ 0\ 1$ . This is a {110} merohedral twin of index 1, forming a “penetration twin” similar to the “iron cross” twins seen in in pyrite. Arsenic was assigned to the Wyckoff position  $24g [x\ y\ 0]$ . Due to the inability of X-ray data to distinguish Ni, Co, and Fe from one another, the three elements were assigned to  $M$  at the  $8c$  position  $[\frac{1}{4}\ \frac{1}{4}\ \frac{1}{4}]$ , and the ratios of Ni, Co, and Fe were constrained to the empirical formula generated from microprobe data. Note, refining site  $8c$  without constraining the ratios of Ni, Co, and Fe to the empirical formula, but keeping the sum of the cations at 1.00, resulted in differences of up to 16% from the microprobe generated formula. Constraining either Co or Fe, not both, to the value of the empirical formula resulted in differences of only 3%.

The positions of all atoms were refined with anisotropic displacement parameters. The refined coordinates and displacement parameters are listed in Table 3, and selected

bond distances and angles are in Table 4. Negligible residual electron density at the icosahedral site,  $A$  (0, 0, 0), indicated that nickelskutterudite R100196 is unfilled. However, residual electron density was seen at  $A$  for skutterudite R050593 and nickelskutterudite R100194. Site occupancy refinement of  $A$  showed 0.01 metal (Co, Ni, or Fe) atom per formula unit in R050593 and R100194.

## RESULTS

As shown in Fig. 1, the structure of nickelskutterudite consists of corner-sharing  $MAs_6$  octahedral groups ( $M = Ni, Co, \text{ or } Fe$ ), similar to the octahedral groups in the  $\alpha$ - $ReO_3$  structure (space group  $Pm\bar{3}m$ , no. 221). However, the  $NiAs_6$  octahedra are tilted about  $[111]$  from the ideal orientation of octahedra in the  $ReO_3$  structure, thereby emplacing As atoms into three quarters of the icosahedral cages (Aleksandrov and Beznosikov 2007, Návrtil et al. 2010). Each of these “stuffed” icosahedral cages contains four As atoms that are close enough to bond, forming a rectangular  $As_4$  ring (Fig. 2). In filled skutterudite compounds, the remaining quarter of the icosahedral cages accommodate filling cations. In the ideal perovskite structure,  $ABX_3$ , each icosahedral cage is occupied by an  $A$  cation, and there are no  $X_4$  rings “stuffed” into the cages. In such a way, the filled skutterudite compounds,  $AB_4X_{12}$ , can be thought of as intermediaries between the  $ReO_3$  and perovskite structures. Interestingly, Aleksandrov and Beznosikov (2007) reported that at pressure ( $\sim 0.52$  GPa), the  $ReO_3$  structure deforms to the skutterudite structure. It would be interesting to demonstrate bonded  $O_4$  rings in high-pressure  $ReO_3$ .

Concomitant with tilting of the octahedra is distortion of the octahedra. Measured As-Ni-As angles for  $NiAs_6$  octahedra in nickelskutterudite deviate significantly ( $\sim 6^\circ$ )

from  $90^\circ$  (Table 3), resulting in Ni coordination polyhedra that resemble trigonal prisms, as previously noted by Ventriglia (1957). Mitchell (2002) and Chakoumakos and Sales (2006) both describe octahedral distortion as a function of both octahedral tilt and anion-anion bonding within the skutterudite structure, dependent on composition. Consequently, octahedral distortion increases as anion-anion distances within the  $X_4$  ring decreases from Sb to P.

A system for the classification of octahedral tilt in perovskite derivative structures was developed by Glazer (1972), and is applicable to the skutterudite structure (Mitchell 2002). A brief summary of Glazer's classification is presented here; for an in-depth discussion of octahedral tilt, the reader is referred to Glazer (1972). According to Glazer (1972), octahedral tilt may be thought of as the combination of tilts about the three 4-fold axes of an octahedron. This overall tilt is characterized according to magnitude and direction. Magnitude is the amount of tilt about the three 4-fold axes, denoted  $a$  relative to  $[100]$ ,  $b$  relative to  $[010]$ , and  $c$  relative  $[001]$ , and equality of tilt is shown by repeating the appropriate letter. Direction refers to tilt of octahedra in successive layers along a given 4-fold axis, denoted as a superscript 0 for no tilt, + for tilt in the same direction, and – for tilt in the opposite direction (Glazer 1972).  $\text{NiAs}_6$  octahedra in nickelskutterudite (and  $\text{MAs}_6$  octahedra in all other skutterudite structures) have equal tilt about all three 4-fold axes, and the tilt of  $\text{NiAs}_6$  octahedra in successive layers along each axis is the same (Aleksandrov and Beznosikov 2007), so the Glazer tilt notation is  $a^+a^+a^+$ . The angle of tilt  $\varphi$  is  $36.20^\circ$ , calculated according to the equation  $\cos(\varphi) = 3\mathbf{a}/(8\mathbf{d} - 0.5)$ , given in Návratil et al. (2010), where  $\mathbf{a}$  is the unit cell edge and  $\mathbf{d}$  is the metal-arsenic bond distance.

Distances between P, Sb, and As in  $X_4$  rings within various synthetic skutterudite compounds were noted by Chakoumakos and Sales (2006) as comparable to distances between nearest neighbor atoms in elemental P, Sb, and As, consistent with  $X-X$  bonding. Distances between As atoms in  $As_4$  rings in nickelskutterudite measure 2.5467(6) Å and 2.4749(5) Å (average = 2.511 Å), similar to nearest neighbor distances of 2.517 Å within native arsenic (hexagonal As; Schiferl and Barrett 1969) and 2.493 Å in arsenolamprite (orthorhombic As; Smith et al. 1974), consistent with As-As bonding. Although the  $As_4$  ring in skutterudite was described by Oftedal (1926) as having four equal sides, nickelskutterudite and skutterudite (Mandel and Donohue 1971) have rings with two different As-As distances, forming rectangles.

In order to test whether or not the As atoms are bonded in skutterudite, the procrystal electron density distribution was calculated using the experimental space group, unit cell dimensions, and atomic coordinates obtained from the single crystal x-ray diffraction data gathered in this study, as outlined by Gibbs et al. (2008), using the software SPEEDEN (Downs et al. 1996). Fig. 3 shows an electron density contour map in the plane of the  $As_4$  ring. Bond paths and saddle points are located in the electron density along the sides of the ring. These saddle points represent (3,-1) bond critical points that satisfy the conditions of Bader (1998): a bonded pair of atoms exists if and only if a bond path and a saddle point exist in the electron density between them, demonstrating As-As bonded interactions in the  $As_4$  ring of nickelskutterudite.

## DISCUSSION

To check for anion deficiency in our skutterudite samples, microprobe data were normalized to a cation-site sum of 1.00 and compared to the formulas generated by normalizing to an anion-site sum of 3.00 (Table 1). When the empirical formulas were normalized to a cation-site sum of 1.00, the formulas were slightly anion deficient. The same formulas, when normalized to an anion-site sum of 3.00, showed a slight cation surplus. Site-occupancy refinement was used to check the validity of each result. Occupancy refinement of the anion site in all four samples showed full occupancy. Occupancy refinement of the *B* cation site showed full occupancy, while residual electron density was seen at the *A* site of R050593 and R100194, and refined to 0.01 metal atoms (Co, Ni, or Fe) per formula unit. Thus, the formulas normalized to 3.00 cations represent the observed structural state, and no anion deficiency is present in our samples.

A relationship was noticed between the degree of octahedral tilt and bond lengths within the  $X_4$  rings. Mitchell (2002) and Chakumakos and Sales (2006) briefly mention the inversely proportional relationship between *X-X* interatomic distances and octahedral tilt, and when we calculated octahedral tilt for various skutterudite phases using the equation given by Návratil et al. (2010), it was seen that as the shortest *X-X* interatomic distance decreases, and therefore the smaller the ionic radius, the greater the octahedral tilt. Table 4 and Fig. 4 show this relationship for various skutterudite type compounds. Phosphides, with the shortest *X-X* bond length, show the greatest tilt, while antimonides, with the longest, show the least tilt, however there is some overlap between the phosphides and arsenides. This relationship begs the chicken-and-egg question: why do the  $MeX_6$  octahedra tilt and why do the  $X_4$  rings form?

The general formula of nickelskutterudite,  $\text{NiAs}_3$ , is not charged balanced assuming  $\text{Ni}^{2+}$ ,  $\text{Ni}^{3+}$  or  $\text{Ni}^{4+}$ . Nickel (1969) suggested that in the skutterudite structure, Ni displays a charge of +4 and As a charge of -3, which give an overall charge of -5. In order to compensate for this charge imbalance, the anions form  $\text{As}_4$  rings (Návrtil et al. 2010; Patrik and Lutz 1999; Takizawa et al. 1999). Tilting of  $\text{NiAs}_6$  octahedra “stuffs” four As atoms into an icosahedral void, allowing them to form a four member,  $\sigma$ -bonded ring, with each As sharing one electron with two other As atoms for an overall charge of -4 (Patrik and Lutz 1999, Nickel 1969).

The chemistry of two different nickelskutterudite samples were examined in this study: R100194 (Schneeberg, Saxony, Germany), and R100196 (New Mexico, USA). Each contains significant amounts of Co and Fe: R100194 empirical formula  $(\text{Ni}_{0.86}\text{Co}_{0.14}\text{Fe}_{0.01})_{\Sigma=1.01}(\text{As}_{2.99}\text{S}_{0.01})_{\Sigma=3.00}$ , R100196 empirical formula  $(\text{Ni}_{0.62}\text{Co}_{0.28}\text{Fe}_{0.12})_{\Sigma=1.02}(\text{As}_{2.95}\text{S}_{0.05})_{\Sigma=3.00}$ . The presence of significant Co and Fe may be explained by the different electronic configurations of  $\text{Ni}^{4+}$  and  $\text{Co}^{3+}$  in the skutterudite structure. Nickel (1969) notes that in the skutterudite structure, cations achieve complete spin-pairing of their non-bonded  $d$ -electrons. For example, when  $\text{Co}^{3+}$  donates sufficient electrons to form pair bonds with neighboring atoms, it has 6 non-bonded  $d$ -electrons which can be spin paired (Nickel 1969). In order for Ni to be left with 6 non-bonded electrons, it must be quadrivalent, and if  $\text{Ni}^{4+}$  donates sufficient electrons to form pair-bonds with all 6 neighboring atoms, it is left with 7 non-bonded electrons, which cannot be fully spin-paired (Nickel, 1969).

## IMPLICATIONS

Important concentrations of Co and Fe in natural NiAs<sub>3</sub>, and the apparent inability to synthesize pure NiAs<sub>3</sub> indicate that Co<sup>3+</sup> and/or Fe<sup>2+</sup> are required to stabilize the nickelskutterudite structure (Grystiv et al. 2002; Borshchevsky et al. 1996; Nickel 1969). For comparison, pure CoAs<sub>2</sub> (clinosaflorite) crystallizes in the arsenopyrite-type structure (*P2<sub>1</sub>/c*) because of the unpaired, non-bonded electron of Co<sup>2+</sup> occupying a  $\pi_b$  orbital (Yang et al. 2008). Incorporation of Ni<sup>2+</sup> and Fe<sup>2+</sup> into CoAs<sub>2</sub> results in crystallization of (Co,Ni,Fe)As<sub>2</sub> (safflorite) in the marcasite-type structure (*Pnmm*), explained by the ability of Fe<sup>2+</sup> and Ni<sup>2+</sup> to spin-pair non-bonded electrons and thus achieve a lower energy, higher symmetry structure (Yang et al. 2008). Further synthesis experiments could be used to constrain the amounts of Co<sup>3+</sup> and/or Fe<sup>2+</sup> necessary to stabilize the nickelskutterudite structure.

Additionally, no anion deficiencies were found in skutterudite phases by either X-ray or electron microprobe, supporting Roseboom's (1962) interpretation that anion deficient skutterudite samples likely do not consist of a single phase. For these reasons, we propose the chemical formula of nickelskutterudite (currently given as NiAs<sub>3-x</sub> by the IMA) should be (Ni,Co,Fe)As<sub>3</sub>.

## ACKNOWLEDGEMENTS

The authors gratefully acknowledge Ron Gibbs for kindly providing the nickelskutterudite sample to the RRUFF Project. Funding support for this study was given by Freeport McMoRan, the Mineralogical Society of America Krauss Crystallographic Research Grant, and M.B.A. acknowledges support by the Brazilian government (FAPESP 2013/03487-8).

## REFERENCE

- Aleksandrov, K.S., and Beznosikov, B.V. (2007) Crystal Chemistry and Prediction of Compounds with a Structure of Skutterudite Type. *Kristallografiya*, 52:1, 32-40.
- Bader, R.F.W. (1998) A Bond Path: A Universal Indicator of Bonded Interactions. *Journal of Physical Chemistry A*, 102, 7314-7323
- Borshchevsky, A., Caillat, T., and Fleurial, J.-P. (1996) Solid Solution Formation: Improving the Thermoelectric Properties of Skutterudites. *Proceedings of the 15<sup>th</sup> International Conference on Thermoelectrics 1996*, 112-116.
- Braun, D.J., and Jetschko, W. (1980) Ternary Arsenides with LaFe<sub>4</sub>P<sub>12</sub>-Type Structure. *Journal of Solid State Chemistry*, 32, 357-363.
- Breithaupt, J.F.A. (1827) Ueber eine neue Kies-Spezies von Skutterud. *Annaler der Physik und Chemie*, 9, 115-116.
- Bruker (2007) APEX2, SAINT, and TWINABS. Bruker AXS Inc., Madison, Wisconsin, USA.
- Chakoumakos, B.C., and Sales, B.C. (2006) Skutterudites: Their structural response to filling. *Journal of Alloys and Compounds*, 407, 87-93.
- Downs, R.T., Andalman, A., and Hudacsko, M. (1996) The coordination numbers of Na and K atoms in low albite and microcline as determined from a procrystal electron density distribution. *American Mineralogist*, 81, 1344-1349.
- Evers, C.B.H., Jetschko, W., Boonk, L., Braun, D.J., Ebel, T., Scholz, U.D. (1995) Rare earth and uranium transition metal pnictides with LaFe<sub>4</sub>P<sub>12</sub> structure. *Journal of Alloys and Compounds*, 224, 184-189.

- Fukuoka, H., and Yamana, S. (2009) High-Pressure Synthesis, Structure and Electrical Properties of Iodine Filled Skutterudite  $I_{0.9}Rh_4Sb_{12}$ -First Anion-Filled Skutterudite. *Chemistry of Materials*, 22, 47-51.
- Gibbs, G.V., Downs, R.T., Cox, D.F., Ross, N.L., Prewitt, C.T., Rosso, K.M., Lippmann, T., and Kirfel, A. (2008) Bonded interactions and the crystal chemistry of minerals: a review. *Zeitschrift für Kristallographie*, 223, 1-40.
- Glazer, A.M. (1972) The Classification of Tilted Octahedra in Perovskites. *Acta Crystallographica*, B28, 3384-3392.
- Grytsiv, A., Rogl, P., Berger, St., Paul, Ch., Michor, H., Bauer, E., Hilscher, G., Godart, C, Knoll, P., Musso, M., Lottermoser, W., Saccone A., Ferro, R., Roisnel, T., Noel, H. (2002) A novel skutterudite phase in the Ni-Sb-Sn system: phase equilibria and physical properties. *Journal of Physics: Condensed Matter*, 14, 7071-7090.
- Haidinger, W. (1845) Zwei Klasse: Geogenide. XIII. Ordnung. Kiese III. Kobaltkies. Skutterudit, in *Handbuch der Bestimmenden Mineralogie*, Bei Braumüller und Seidel, Wien, 559-562.
- Holmes R.J. (1947) Higher mineral arsenides of cobalt, nickel, and iron, *Geological Society of America Bulletin*, 58, 299-392.
- Kjekshus, A., and Rakke, T. (1974) Compounds with the Skutterudite Type Crystal Structure. III. Structural Data for Arsenides and Antimonides. *Acta Chemica Scandanavica*, A 28:1, 99-103.

- Mandel, M., and Donahue, J. (1971) The refinement of the crystal structure of skutterudite,  $\text{CoAs}_3$ . *Acta Crystallographica*, B27, 2288-2289.
- Mitchell, R.H. (2002) *Perovskites Modern and Ancient*, 316 pp. Thunder Bay: Almaz Press.
- Navrátil, J., Laufek, F., Plecháček, T., Plášil, J. (2010) Synthesis, crystal structure and thermoelectric properties of the ternary skutterudite  $\text{Fe}_2\text{Pd}_2\text{Sb}_{12}$ . *Journal of Alloys and Compounds*, 493, 50-54.
- Nickel, E.H. (1969) The application of ligand-field concepts to an understanding of the structural stabilities and solid solution limits of sulphides and related minerals. *Chemical Geology*, 5, 233-241.
- Oftedal, I. (1926) The crystal structure of skutterudite and related minerals. *Norsk Geologisk Tidsskrift*, 8, 250-257.
- Oftedal, I. (1928) Die Kristallstruktur von Skutterudite und Speiskobalt-Chloanthit. *Zeitschrift für Kristallographie*, A66, 517-546.
- Palache, C., Berman, H., Frondel, C. (1944) *Dana's System of Mineralogy*, Vol. I, 829 pp. New York: John Wiley and Sons.
- Patrick, M., and Lutz, H.D. (1999) Semiempirical band structure calculations on skutterudite-type compounds. *Physical Chemistry and Mineralogy*, 27, 41-46.
- Pauling, L. (1978) Covalent chemical bonding of transition metals in pyrite, cobaltite, skutterudite, millerite and related minerals. *Canadian Mineralogist*, 16, 447-452.
- Ramsdell, L.S. (1925) The Crystal Structure of Some Metallic Sulfides. *American Mineralogist*, 10:9, 281-304.

- Roseboom E.H. (1962) Skutterudites (Co,Ni,Fe)As<sub>3-x</sub>: Composition and cell dimensions, *American Mineralogist*, 47, 310-327.
- Schiferl, D., and Barrett, C.S. (1969). The crystal structure of arsenic at 4.2, 78 and 299 K. *Journal of Applied Crystallography* 2, 30-36.
- Schmidt, Th., Kliche, G., and Lutz, H.D. (1987) Structure Refinement of Skutterudite-Type Cobalt Triantimonide, CoAs<sub>3</sub>. *Acta Crystallographica*, C43, 1678-1679.
- Sheldrick, G.M. (2008) A short history of SHELX. *Acta Crystallographica*, A64, 112–122.
- Shirotani, I., Hayashi, A., Takeda, K., Nakada, R., Ohishi, Y. (2006) X-ray study with synchrotron radiation for filled skutterudite YbFe<sub>4</sub>P<sub>12</sub> at ambient and high pressures. *Physica B*, 382, 8-13.
- Smith, P.M., Leadbetter, A.J., and Apling, A.J. (1974) The structures of orthorhombic and vitreous arsenic. *Philosophical Magazine*, 31, 57-64.
- Spiridonov, E.M., Gritsenko, Yu.D., and Kulikova, I.M. (2007). Ferrodskutterudite (Fe,Co)As<sub>3</sub>: a new mineral species from the dolomite-calcite veins of Noril'sk ore field. *Doklady Earth Sciences*, 417:8, 1278-1280.
- Takeda, K., Sato, S., Hayashi, J., Sekine, C., Shirotani, I. (2007) Crystal structure of a new superconductor La<sub>x</sub>Rh<sub>4</sub>P<sub>12</sub> prepared at high pressure. *Journal of Magnetism and Magnetic Materials*, 310, e1-e3.
- Takizawa, H., Miura, K., Ito, M., Suzuki, T., Endo, T. (1999) Atom insertion into the CoSb<sub>3</sub> skutterudite host lattice under high pressure. *Journal of Alloys and Compounds*, 282, 79-83.

- Ventriglia, U. (1957) Studi strutturali sugli arseniuri di cobalto. *Periodico di Mineralogia*, 26, 345-383.
- Vollhardt, G. (1888) Versuche über Speiskobalt, *Zeitschrift für Kristallographie und Mineralogie*, 14, 407-408.
- Waller, E., and Moses, A.J. (1893) A probably new nickel arsenide (preliminary notice). *The School of Mines Quarterly*, 14, 49-51.
- Yang, H., Downs, R.T., and Eichler, C. (2008) Safflorite,  $(\text{Co,Ni,Fe})\text{As}_2$ , isomorphous with marcasite. *Acta Crystallographica*, E64, i62.
- Zemni, S., Tranqui, Duc., Chaudouet, P., Madar, R., Senateur, J.P. (1986) Synthesis and Crystal Structure of a New Series of Ternary Phosphides in the system Tr-Co-P (Tr: Rare Earth). *Journal of Solid State Chemistry*, 65, 1-5.

## FIGURE CAPTIONS

Figure 1. Representative image of the crystal structure of nickelskutterudite (left), viewed along [001]. Green octahedra represent  $\text{NiAs}_6$  groups and As displacement parameters at 99% are represented by grey ellipsoids. Unit cell edges are indicated by the grey square. A representation of the crystal structure of  $\alpha\text{-ReO}_3$ , viewed along [001] (right), is included for the purpose of comparison.

Figure 2. A depiction of the crystal structure of nickelskutterudite as a primitive cubic lattice with white spheres representing metal atoms at lattice points. Three quarters of these cubes contain rectangular four membered rings of bonded As atoms indicated by green rods.

Figure 3. Procrystal electron density map of a rectangular four membered ring of bonded As atoms, from 0.005 to 0.200  $\text{e}/\text{\AA}^3$  in steps of 0.005  $\text{e}/\text{\AA}^3$ . The 0.055  $\text{e}/\text{\AA}^3$  contour is dashed to emphasize the difference in electron density at the bond critical points associated with the different lengths of As-As bonds. The bond critical points are represented by saddles in the contours between bonded As atoms. Note three other As atoms at left (black stars), representing other four membered rings above and below the plane of the observed ring.

Figure 4. Graph showing the inverse relationship between octahedral tilt and shortest anion-anion ( $X-X$ ) distance in  $X_4$  rings in the skutterudite structure. As the  $X-X$  distance, and therefore the size of the  $X$  atom, increases, octahedral tilt will decrease.

## FIGURES

Figure 1

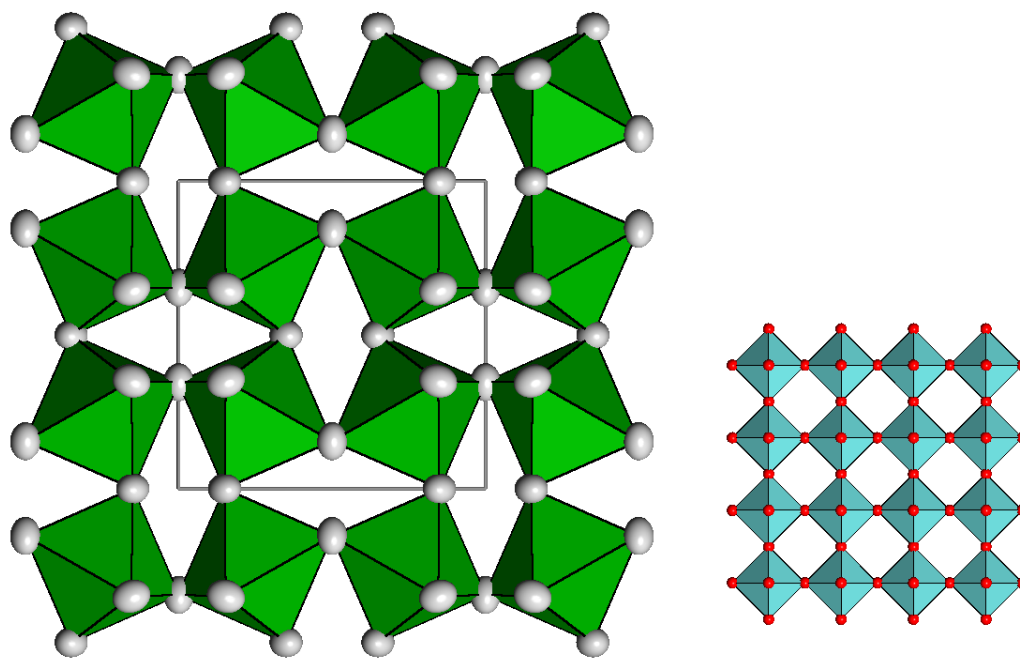


Figure 2

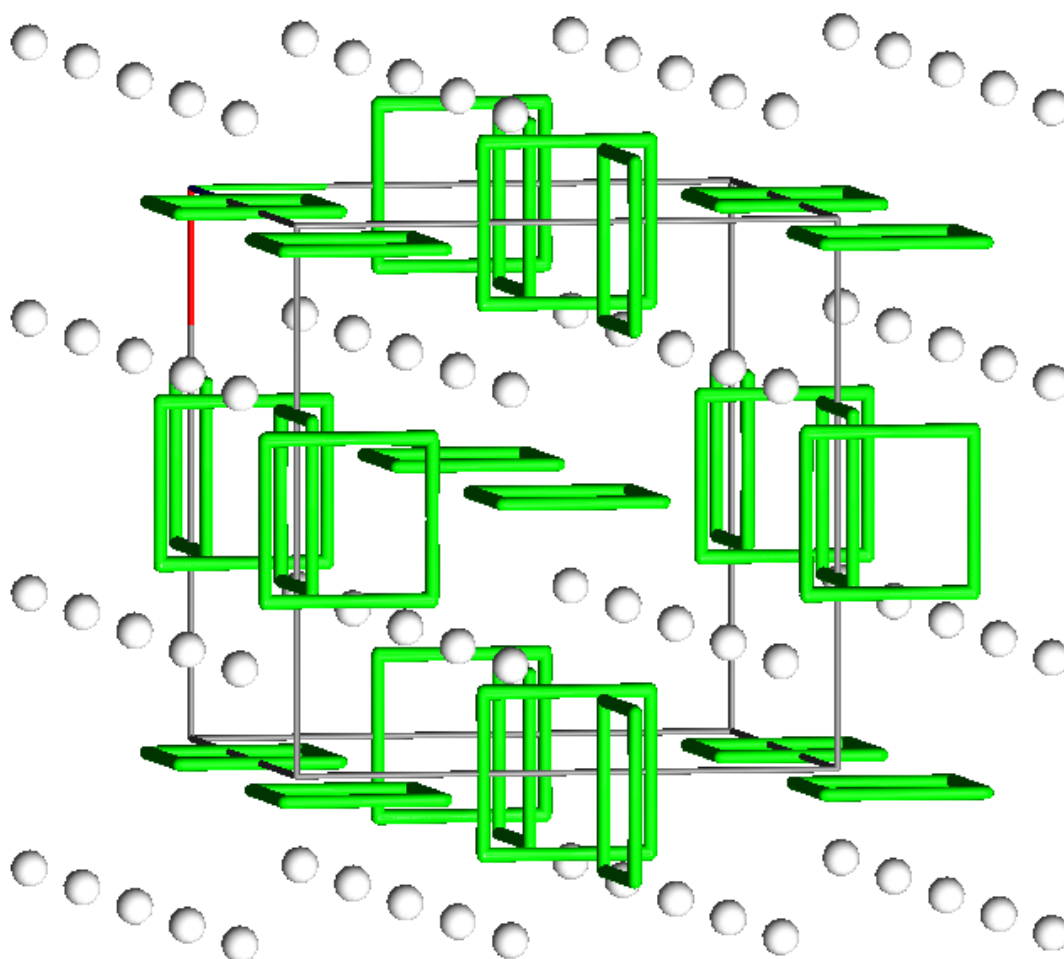


Figure 3

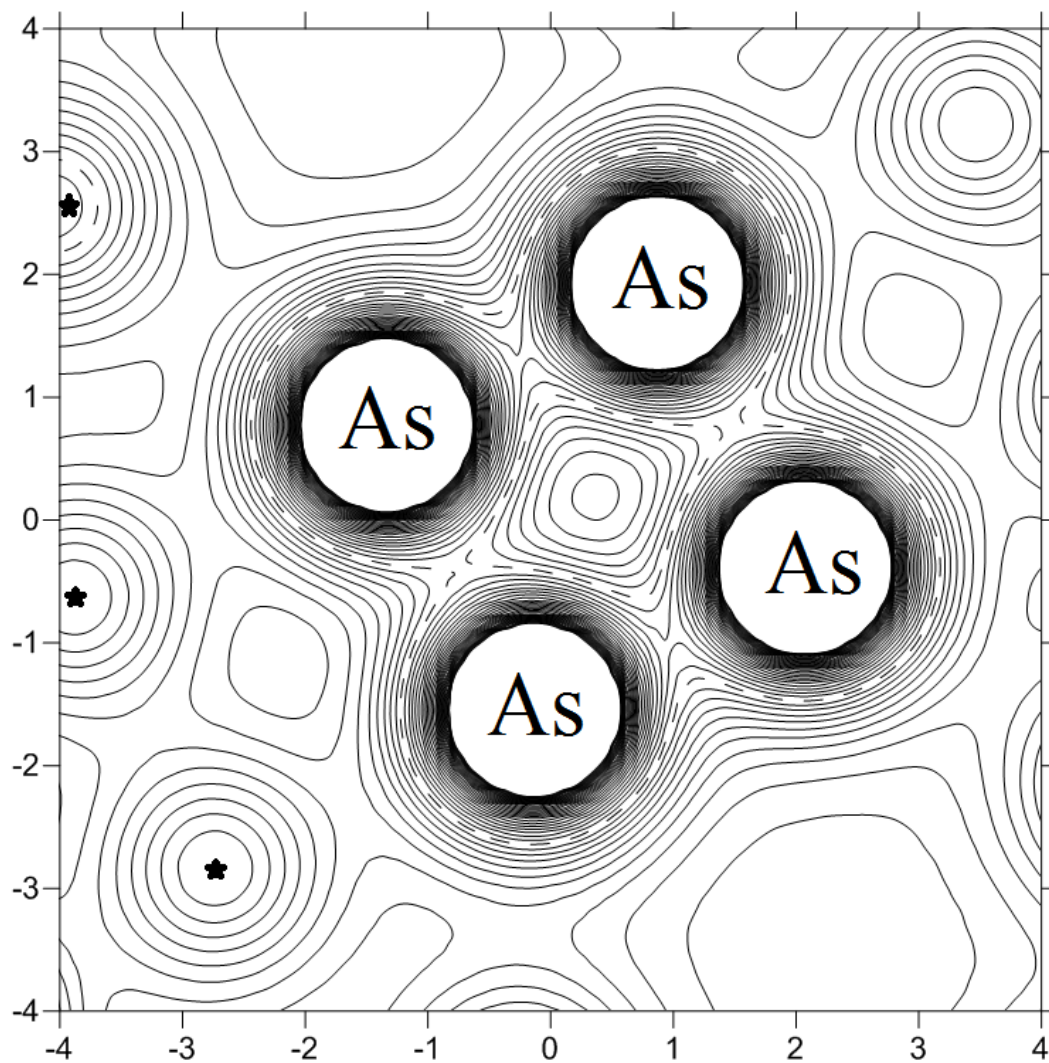
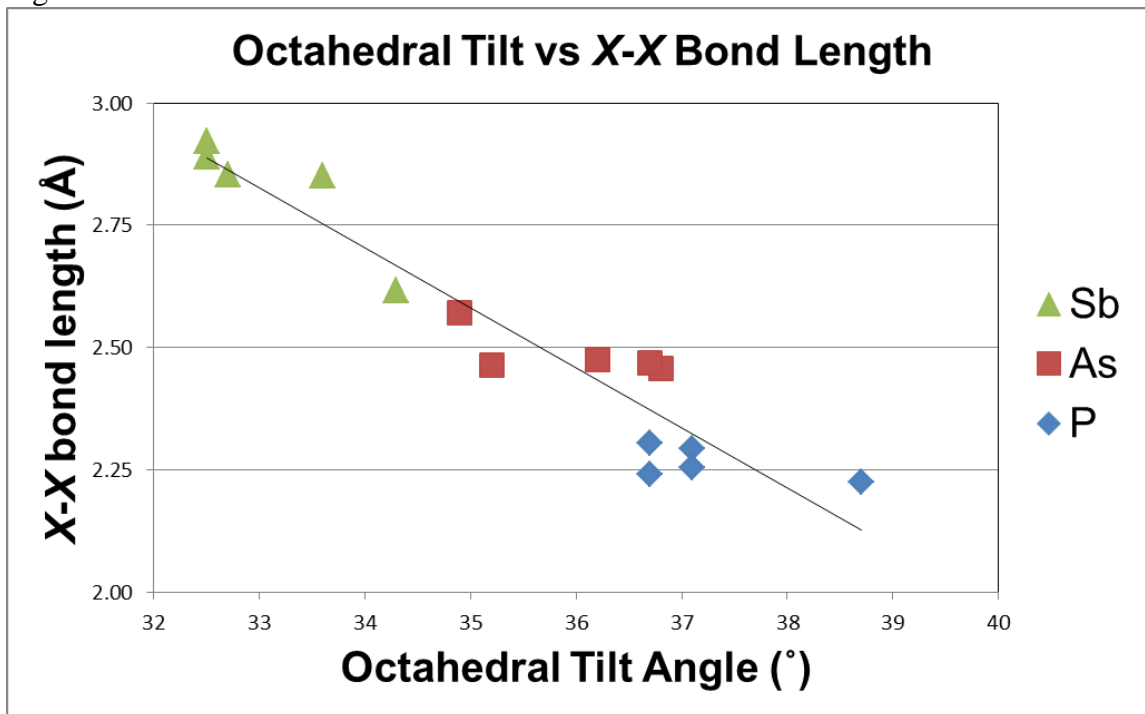


Figure 4



## TABLE EXPLANATORY NOTES

Table 1. Electron microprobe data for skutterudite and nickelskutterudite samples in weight percent.

Table 2. Summary of crystal data and refinement results for skutterudite and nickelskutterudite.

Table 3. Fractional atomic coordinates, equivalent isotropic displacement parameters, occupancies, and atomic displacement parameters ( $\text{\AA}^2$ ) for skutterudite and nickelskutterudite.

Table 4. Selected interatomic distances and angles for nickelskutterudite R100196. The Ni, Co, and Fe site is identified as *M*. The theoretical icosahedral bond length, *A*-As, is included for purposes of discussion even though *A* is not occupied.

Table 5.  $MX_6$  octahedral tilt compared by anion (*X*) and shortest *X-X* interatomic distance for both filled and unfilled skutterudite phases.

## TABLES

Table 1

Sample	R050593	R100195	R100194	R100196 Alhambra mine
Locality	Bou Azzer	Skutterud	Schneeberg	mine
a-cell, Å	8.2060(10)	8.2070(4)	8.2876(5)	8.2653(6)
Ni	1.42(18)	1.04(2)	17.82(48)	12.76(90)
Co	17.68(20)	18.54(7)	2.88(44)	5.8(48)
Fe	2.1(18)	1.52(1)	0.25(7)	2.41(51)
Bi	nd*	0.34(13)	0.27(19)	0.34(20)
As	76.32(74)	78.00(12)	78.64(22)	77.95(24)
S	0.82(9)	0.31(6)	0.06(4)	0.59(11)
Sum	98.34	99.75	99.92	99.85

## Formula

R050593  $(\text{Co}_{0.86}\text{Fe}_{0.11}\text{Ni}_{0.07})_{\Sigma=1.04}(\text{As}_{2.97}\text{S}_{0.03})_{\Sigma=3.00}$

R100195  $(\text{Co}_{0.90}\text{Fe}_{0.08}\text{Ni}_{0.05})_{\Sigma=1.03}(\text{As}_{2.97}\text{S}_{0.03})_{\Sigma=3.00}$

R100194  $(\text{Ni}_{0.85}\text{Co}_{0.14}\text{Fe}_{0.01})_{\Sigma=1.01}(\text{As}_{2.99}\text{S}_{0.01})_{\Sigma=3.00}$

R100196  $(\text{Ni}_{0.62}\text{Co}_{0.28}\text{Fe}_{0.12})_{\Sigma=1.02}(\text{As}_{2.95}\text{S}_{0.05})_{\Sigma=3.00}$

Note: \*nd = not determined

Table 2

	Skutterudite (R050593, Morocco)	Skutterudite (R100195, Norway)	Nickelskutterudite (R100194, Germany)	Nickelskutterudite (R100196, New Mexico)
IMA-defined chemical formula	CoAs <sub>3-x</sub>	CoAs <sub>3-x</sub>	NiAs <sub>2-3</sub>	NiAs <sub>2-3</sub>
Effective structural formula	<sup>M1</sup> Co <sub>1.00</sub> <sup>M2</sup> Fe <sub>0.01</sub> As <sub>2.90</sub> S <sub>0.10</sub>	<sup>M1</sup> Co <sub>1.00</sub> As <sub>3.00</sub>	<sup>M1</sup> Ni <sub>1.00</sub> <sup>M2</sup> Fe <sub>0.01</sub> As <sub>3.00</sub>	<sup>M1</sup> Ni <sub>0.59</sub> <sup>M2</sup> Co <sub>0.2499</sub> <sup>M2</sup> Fe <sub>0.14</sub> As <sub>3.00</sub>
Space group	<i>Im</i> -3 (No. 204)	<i>Im</i> -3 (No. 204)	<i>Im</i> -3 (No. 204)	<i>Im</i> -3 (No. 204)
<i>a</i> (Å)	8.2060(10)	8.2070(4)	8.2876(5)	8.2653(6)
<i>V</i> (Å <sup>3</sup> )	552.6(1)	552.78(5)	569.23(6)	564.65(7)
<i>Z</i>	8	8	8	8
$\rho_{\text{calc}}$ (g/cm <sup>3</sup> )	6.719	6.818	6.615	6.675
$\lambda$ (Å)	0.71073	0.71073	0.71073	0.71073
$\mu$ (mm <sup>-1</sup> )	40.41	41.49	41.07	41.04
2 $\theta$ range for data collection	≤68.75	≤68.28	≤68.44	≤68.65
No. of reflections collected	1279	1259	1205	1266
No. of independent reflections	232	224	231	234
No. of reflections with $I > 2\sigma(I)$	214	215	220	225
No. of parameters refined	17	12	14	13
R(int)	0.02	0.019	0.022	0.033
Final $R_1$ , $wR_2$ factors [ $I > 2\sigma(I)$ ]	0.015, 0.036	0.011, 0.023	0.010, 0.023	0.014, 0.029
Final $R_1$ , $wR_2$ factors (all data)	0.018, 0.037	0.012, 0.023	0.012, 0.023	0.015, 0.029
Goodness-of-fit	1.106	1.209	1.12	1.001
Twin law				(0 1 0/1 0 0 /0 0 1)
Twin ratio				0.88/0.12

Table 3

Element	x	y	z	$U_{eq}$ (Å <sup>2</sup> )	Occ. (<1)	$U^{11}$	$U^{22}$	$U^{33}$	$U^{12}$	$U^{13}$	$U^{23}$
R050593											
M*	0.25	0.25	0.25	0.00310(18)	0.989(4)	0.00310(18)	0.00310(18)	0.00310(18)	0.00047(11)	0.00047(11)	0.00047(11)
Fe	0	0	0	0.000(15)	0.0127(9)						
As	0.15012(4)	0.34300(5)	0	0.00452(14)	0.967(5)	0.00434(17)	0.0057(2)	0.00350(16)	0.00054(10)	0	0
S	0.121(3)	0.273(4)	0	0.009(6)*	0.033(5)						
R100195											
Co	0.25	0.25	0.25	0.00227(13)	1.00(3)	0.00227(13)	0.00227(13)	0.00227(13)	0.00013(8)	0.00013(8)	0.00013(8)
As	0	0.15024(2)	0.34280(2)	0.00316(8)	0.99(3)	0.00211(10)	0.00295(11)	0.00442(11)	0	0	0.00048(6)
R100194											
Ni1	0.25	0.25	0.25	0.00529(12)		0.00529(12)	0.00529(12)	0.00529(12)	0.00026(8)	0.00026(8)	0.00026(8)
Ni2	0	0	0	0.01(3)	0.008(6)						
As	0	0.34685(2)	0.14960(2)	0.00613(8)		0.00503(10)	0.00752(11)	0.00584(11)	0	0	0.00073(6)
R100196											
M**	0.25	0.25	0.25	0.00471(15)		0.00471(15)	0.00471(15)	0.00471(15)	0.00023(11)	0.00023(11)	0.00023(11)
As**	0.14972(3)	0.34594(3)	0	0.00585(9)		0.00562(15)	0.00734(14)	0.00459(15)	0.00074(8)	0	0

Notes: \*M = Co + Fe.

\*\*M = Ni<sub>0.59(5)</sub>Co<sub>0.280(10)</sub>Fe<sub>0.14(6)</sub>.\*\*As = As<sub>0.99</sub>S<sub>0.01</sub>.

Table 4

	Distance, Å		Angle (°)
M—As	2.3634(2)	As <sup>i</sup> —M—As	84.008(9)
As—As <sup>vii</sup>	2.4749(5)	As <sup>i</sup> —M—As <sup>ii</sup>	95.992(9)
As—As <sup>viii</sup>	2.5467(6)	As—M—As <sup>ii</sup>	84.008(9)
		As <sup>i</sup> —M—As <sup>iii</sup>	84.008(9)
		As—M—As <sup>iii</sup>	95.992(9)
		As <sup>ii</sup> —M—As <sup>iii</sup>	180.000(11)
		As <sup>iv</sup> —M—As <sup>v</sup>	84.007(9)
		M <sup>vi</sup> —As—M	121.928(11)
		M <sup>vi</sup> —As—As <sup>vii</sup>	110.531(6)
		M <sup>vi</sup> —As—As <sup>viii</sup>	109.604(6)
		As <sup>vii</sup> —As—As <sup>viii</sup>	90.0

Table 5

Formula	Anion(X)	Tilt Angle	Shortest X-X Distance	Reference
YbFe <sub>4</sub> P <sub>12</sub>	P	37.1	2.293	Shirotani et al. (2006)
La <sub>x</sub> Rh <sub>4</sub> P <sub>12</sub>	P	38.7	2.224	Takeda et al. (2007)
CeFe <sub>4</sub> P <sub>12</sub>	P	36.7	2.304	Shirotani et al. (2006)
La <sub>0.2</sub> Co <sub>4</sub> P <sub>12</sub>	P	37.1	2.254	Zemni et al. (1986)
CoP <sub>3</sub>	P	36.7	2.240	Zemni et al. (1986)
(Ni,Co,Fe)As <sub>3</sub>	As	36.2	2.475	This Study
IrAs <sub>3</sub>	As	36.8	2.456	Kjekshus and Rakke (1974)
RhAs <sub>3</sub>	As	36.7	2.468	Kjekshus and Rakke (1974)
LaFe <sub>4</sub> As <sub>12</sub>	As	34.9	2.570	Braun and Jeitschko (1980)
CoAs <sub>3</sub>	As	35.2	2.464	Mandel and Donahue (1971)
CoSb <sub>3</sub>	Sb	32.7	2.854	Schmidt, Kliche, and Lutz (1987)
Fe <sub>2</sub> Ni <sub>2</sub> Sb <sub>12</sub>	Sb	32.5	2.890	Návratil et al. (2010)
Fe <sub>2</sub> Pd <sub>2</sub> Sb <sub>12</sub>	Sb	33.6	2.852	Návratil et al. (2010)
IrSb <sub>3</sub>	Sb	34.3	2.617	Kjekshus and Rakke (1974)
NdFe <sub>4</sub> Sb <sub>12</sub>	Sb	32.5	2.921	Evers et al. (1995)

**APPENDIX C: MINERALOGICAL PROFILE OF SUPERGENE SULFIDE ORE  
IN THE WESTERN COPPER AREA, MORENCI MINE**

Benjamin N. Schumer<sup>1</sup>, Ralph J. Stegen<sup>2</sup>, J. Brent Hiskey<sup>3</sup>, Mark D. Barton<sup>1</sup>, and Robert T. Downs<sup>1</sup>

This paper was prepared for submission to the *American Mineralogist*

<sup>1</sup>*Department of Geosciences, University of Arizona, 1040 E. 4th Street, Tucson, Arizona  
85721-0077, USA*

<sup>2</sup>*18601 Stallard Pl., Oro Valley, AZ 85737*

<sup>3</sup>*Department of Mining and Geological Engineering, 1235 James E. Rogers Way,  
Tucson, AZ 85721-0012*

## ABSTRACT

The intergrowths and compositions of supergene copper sulfides from drill hole MOR-4511 in the Western Copper area of the Morenci mine, Greenlee County, Arizona, have been examined by reflected light microscopy and electron probe microanalysis (EPMA) to better understand their development with implications for hydrometallurgical processing. The supergene copper sulfides occur in three main textures: partial to complete replacement of chalcopyrite, partial replacement of pyrite, and partial to complete replacements of one another. Compositions for copper sulfides vary widely, but (Cu+Fe):S ratios of  $1.80 \pm 0.05$ ,  $1.92 \pm 0.03$ , and  $1.10 \pm 0.10$  are dominant. No stoichiometric  $\text{Cu}_2\text{S}$  was found. At shallower depths in the supergene blanket and near/within faults, high Cu:S phases  $1.80 \pm 0.05$  and  $1.92 \pm 0.03$  replacing primary chalcopyrite and pyrite or lower Cu:S supergene sulfides are dominant, and near the base of the blanket low Cu:S phases  $1.10 \pm 0.10$  replacing primary chalcopyrite or higher Cu:S supergene sulfides gradually become more dominant. This indicates high activity of  $\text{Fe}^{3+}$ ,  $\text{Fe}^{2+}$ , and  $\text{Cu}^{2+}$ , necessary to form high Cu:S phases, at shallower depths and near sources of fresh fluid such as faults. Formation of low Cu:S phases directly from chalcopyrite or from high Cu:S phases could be controlled by decreased concentrations of iron species and  $\text{Cu}^{2+}$  due to reaction with primary chalcopyrite and pyrite as fluids descend or migrate away from faults, reduced access to supergene fluids, and/or lower pyrite-chalcopyrite ratios. The compositional patterns of secondary copper sulfides observed at Morenci are similar to those observed in other supergene enrichments of porphyry copper systems worldwide, and are even more similar to compositions seen in leaching experiments of synthetic copper and copper-iron sulfides.

## INTRODUCTION

Porphyry copper deposits contain some of the largest endowments of copper on Earth. They are characterized by large tonnages of relatively low-grade Cu-bearing minerals in vein stockworks and disseminations within hydrothermally altered rock (e.g. Seedorff et al. 2005). Supergene processes acting initially on primary low-grade ore in exhumed porphyry systems produces copper as diverse sulfide, oxide, and oxysalt phases to form enriched and oxide deposits. It is common for subsequent supergene cycles to leach and enrich the prior-formed supergene deposits to produce chalcocite and oxide copper masses having significantly higher grade than the primary ore (Anderson, 1982; Titley and Marozas, 1995; Sillitoe, 2005). Processing of supergene sulfide “chalcocite” ores is typically by concentrating or leaching processes whereas the copper oxides such as chrysocolla are recovered by solvent-extraction-electrowinning (SX-EW) methods.

Mineralogical characterization of supergene processes in copper deposits is exceedingly important for mineral processing methods and recovery determinations. Supergene sulfide deposits often contain a mixture of minerals in the system Cu-S (Table 1). The secondary Cu-sulfide minerals typically occur in varying amounts with hypogene sulfides consisting principally of pyrite, chalcopyrite, bornite, and molybdenite, which each react differently to sulfuric acid-ferric sulfate leach solutions. A limited amount of laboratory studies of leaching chalcopyrite (e.g. Córdoba et al. 2008) and other copper bearing minerals provided an early framework that determined relative recovery amounts specific to individual minerals using acidic  $\text{Fe}^{3+}$  solutions that have broad application to those used in modern heap-leach operations (Sullivan 1933; Goble 1981; Whiteside and Goble, 1986).

However, there are comparatively few detailed mineralogical studies of natural supergene copper sulfides. Sillitoe and Clark (1969) studied the supergene copper and copper-iron sulfides in the Copiapó mining district, Chile, and Goble and Smith (1973) conducted an electron microprobe study on copper sulfides in red bed copper deposits of Alberta. Mineralogical descriptions of supergene copper sulfides in the southwestern United States generally consist of varying proportions of chalcocite and covellite that replaced chalcopyrite and pyrite. An example is the porphyry copper-molybdenum deposit at Morenci, Arizona where a general overview of supergene copper sulfide mineralogy was provided by Enders (2000), but a detailed mineralogical study of supergene enrichment is lacking.

The Morenci mine in Greenlee County, Arizona (Fig. 1), produces copper from supergene and hypogene deposits. Historically, the highest-grade ores at Morenci were oxide copper deposits within skarn and massive chalcocite from enriched veins and stockworks in monzonitic stocks. With the depletion of these high-grade ores, mining progressed to open-pit methods to process the immense tonnages of relatively lower-grade chalcocite by concentrators. The implementation of SX-EW technology in the late 1980s at Morenci provided for the recovery of copper from oxide copper and low-grade chalcocite that is not of sufficient grade for concentrating. Morenci currently recovers copper from concentrating, crush leaching of chalcocite, and run-of-mine leaching of oxide copper and chalcocite. The reserves at Morenci total 12.1 billion pounds of recoverable copper from 664 metric tonnes of mill ore grading 0.42% Cu, 356 million metric tonnes of crushed leach averaging 0.51% Cu, and 2,243 million metric tonnes of

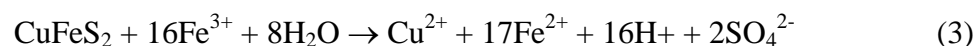
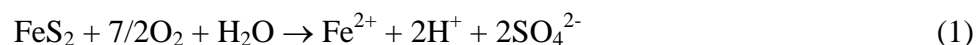
run-of-mine leach with an average grade of 0.18% Cu (Freeport McMoRan 2016 Form 10-K Report).

This study was undertaken to better understand the mineralogy of supergene sulfides at Morenci to aid ore processing and better understand the natural processes governing the formation of supergene copper sulfides. The results from this study also provide mineralogical characteristics that can potentially be useful in leach processing and recovery determinations.

### SUPERGENE PROCESSES IN PORPHYRY COPPER DEPOSITS

Formation of enriched sulfide ore in porphyry systems is broadly dependent upon hypogene ore mineralogy and lithology of host rocks and character of alteration (Titley and Mazoras 1995). Ideal conditions for formation of supergene sulfides are high pyrite-chalcopyrite ratios in hypogene ore hosted in felsic igneous rocks or quartzofeldspathic sediments, alteration assemblages consisting of sericitic or quartz-K feldspar assemblages, and sufficient permeability to allow the downward migration of supergene fluids.

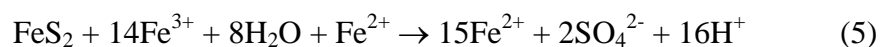
Water reacting with pyrite forms sulfuric acid and ferric ion (reactions (1) and (2)) under oxidizing conditions, which then react with chalcopyrite to dissolve copper by reaction (3):



Copper-rich solutions migrate downward and precipitate copper sulfide minerals under reducing conditions lower in the deposit. The simplified supergene profile consists of a barren leached capping where copper is leached, and is characterized by very low copper

grades occurring with varying amounts and types of iron oxides, and supergene sulfides replace pyrite and chalcopyrite beneath the leached cap in the zone of enrichment at the base of the sequence (Titley and Mazoras 1995). Oxide copper zones that include chrysocolla, malachite, and native copper occur within or proximal to the leached capping and are the product of *in situ* oxidation of hypogene or supergene sulfides that likely formed as a result of low pyrite-chalcopyrite ratios, reactive host rocks, and other factors which inhibit the leaching and transport of copper.

Additionally, bacterial action is thought to play an essential role in supergene processes. Acidithiobacillus bacteria, found by Enders et al. (2006) in the 5200 bench of the Metcalf area at Morenci, catalyze the normally very slow process of abiotic pyrite oxidation, resulting in a rate five orders of magnitude faster than abiotic oxidation alone (reactions (4) and (5)):



This reaction kinetics increase allows for formation of a supergene blanket in a reasonable time frame, whereas abiotic oxidation alone would take so long destruction of the hypogene mineralization by erosion of the deposit would be a danger (Enders et al. 2006). Reactions between supergene fluids and hypogene sulfide minerals to form enrichments can take place in tens of years under favorable conditions.

#### GEOLOGY OF THE MORENCI DEPOSIT

Morenci is located in southeastern Arizona, approximately 175 km northeast of Tucson. A laterally extensive chalcocite-enriched blanket is situated within and atop a hypogene Cu-Mo deposit associated with Early Eocene (54-56 Ma) monzonitic stocks. The monzonitic stocks were emplaced within Proterozoic granitoids and Paleozoic

sedimentary rocks as a large composite stock with numerous and extensive dikes. A notable feature of the district is the widespread sericitic stockwork veinlets and veins developed within Eocene stocks and adjacent Proterozoic granitoids that have a pyrite content of 3-7%. Beneath the sericitic alteration is a zone of K-silicate veinlets containing pyrite, chalcopyrite, and molybdenite that is best developed as ore shells proximal to the Eocene stock contacts.

The Morenci district is cut by faults of variable ages and orientations. Early faults with northwesterly trends controlled emplacement of Eocene dikes and major base metal veins. Displacing these are a set of northerly trending and a final set of northwesterly-trending faults that are leached and controlled chalcocite enrichment at depth.

A Neogene conglomerate containing discontinuous exotic copper and iron oxides was deposited in the southern part of the district and is cut by northwesterly-trending faults and a major northeasterly-trending fault named the San Francisco.

#### WESTERN COPPER STUDY AREA

The Morenci mine is currently mining and processing supergene and hypogene ores from several open pits (Fig. 1). One of these pits is Western Copper where mining is exploiting a large and extensive chalcocitic blanket that overlies hypogene ore consisting of chalcopyrite, pyrite, and molybdenite veinlets that constitute a significant portion of milling ore reserves. The chalcocite blanket at Western Copper is a continuation of a district-wide enriched zone that extends about four kilometers west and seven kilometers north, part of which was mined historically as the Clay orebody in the Morenci pit.

The Western Copper area was identified for study because it contains a large proportion of the Morenci reserves, and a significant amount of these reserves consist of

supergene chalcocitic enrichment. Diamond drill hole 4511 was selected for sampling because of its location within the enrichment blanket, a complete interval of core is available through the enriched zone, and it is within an area that will be mined and processed within the near- to medium-term.

Eocene monzonitic stocks and dikes comprise the lithologies in core hole 4511. From the hole collar to a depth of about 175 meters is leached cap consisting of a mixture of earthy goethite and hematite; no sulfide minerals are present. A transition zone containing partially leached chalcocite extends to 200 meters where the top of the supergene enrichment was encountered. Supergene copper sulfides predominate over oxide minerals and hypogene chalcopyrite between 200 and 525 meters. Copper sulfides occur as replacements of chalcopyrite in veinlets and as disseminations in porphyry, rimming or completely replacing pyrite or chalcopyrite. Faults were logged at 200, 202, 217, 252, 306, and 376 meters. Fault zones contain rounded quartz-rich grains and shattered pyrite and chalcopyrite in gray to red gouge with rounded pebbles of altered rock. All fault zones contain copper sulfides rimming and replacing chalcopyrite and pyrite. The red color of fault gouge at 200 and 202 meters is caused by finely divided hematite.

#### MATERIALS AND EXPERIMENTAL METHODS

Sulfide-containing pieces were cut from half-split HQ core from drill hole MOR-4511, cast in epoxy, and polished for analysis. Each sample was examined and interpreted under the ore microscope before electron microprobe analysis.

Electron microprobe analyses were performed at the Lunar and Planetary Laboratory at the University of Arizona using a Cameca SX50 electron microprobe, using beam conditions of 15 kV and 40 nA. Each sample was analyzed for Cu, Fe, As, and S, using

a chalcopyrite standard and  $K\alpha$  lines for Cu, Fe, and S, and a NiAs standard and  $L\alpha$  line for As. Detection limits were 0.064 wt. % Cu, 0.028 wt. % Fe, 0.038 wt. % As, and 0.018 wt. % S. Arsenic was below detection limit in every sample analyzed. Each composition was normalized to one anion, using an average of five analysis points, though as few as two to as many as eight analyses were used in some cases. Results of the electron microprobe analyses are given as (Cu+Fe)/S and are presented in Table 2 and Fig. 5.

## RESULTS

### *Hypogene Mineralogy*

The hypogene mineralogy in drill hole MOR-4511 is relatively simple. Based on polished section interpretations, the main ore mineral is chalcopyrite, always accompanied by pyrite and quartz, in veinlets and alteration envelopes. Molybdenite infrequently occurs with copper sulfide-chalcopyrite aggregates; it is not altered by supergene fluids. Some pyrite is sieve-textured, containing inclusions of chalcopyrite, bornite, sphalerite, and hematite. Wavelength-dispersive spectroscopy (WDS) analyses identified acanthite, a Cu-Bi-S phase and an Ag-Bi-Te phase (most likely volynskite,  $AgBiTe_2$ ) as blebs in pyrite. Pyrite was interpreted to have formed last in all samples examined.

Minerals in the granite host rock are K-feldspar, quartz, biotite, and minor sericite. Biotite occurs as both competent primary crystals and disarrayed “shreddy” aggregates of secondary material. Shreddy biotite occurs as overgrowths on primary biotite crystals and as massive aggregates. Chlorite infrequently occurs interlayered with non-shreddy biotite. Rutile, apatite, and zircon occur as inclusions predominantly in both primary and

secondary biotite but also within quartz and K-feldspar. Monazite occurs as inclusions in quartz and K-feldspar, rarely associated with rutile and zircon.

### *Supergene Mineralogy*

The supergene copper sulfides form as rims on pyrite and chalcopyrite or as discrete grains formed from total replacement of the primary sulfide, occurring both in veinlets and alteration envelopes/areas of pervasive alteration caused by coalesced veinlet envelopes. Three supergene ore textures are present in the samples: copper sulfides replacing chalcopyrite, copper sulfides replacing pyrite, and copper sulfides replacing one another. Using the ore microscope, high and low Cu:S phases could only be broken out based on their reflection properties: high Cu:S phases were a mottled gray or bluish gray, and low Cu:S phases all had intense sky blue to bluish white reflection pleochroism and flame orange to black anisotropy, almost identical to covellite. Herein the low Cu:S phases will be referred to as blue-remaining (*blaubleibender*) covellite phases, after their property of remaining blue after immersion in oil of refractive index 1.55 where covellite would turn reddish-violet (Goble and Smith 1973).

Where both pyrite and chalcopyrite are present in the same sample, the copper sulfides replaced the chalcopyrite first, typically leaving pyrite unaltered, regardless of location within the hole (Fig. 2). Hematite, goethite, and jarosite occur with secondary copper sulfides in some samples high in the hole, but are for the most part lacking. Fault zones contain only high Cu:S phases replacing chalcopyrite and/or pyrite typically associated with hematite. Blue-remaining covellite phases form partial to complete crystallographically oriented replacements of chalcopyrite grains (Fig. 3). Blue-

remaining covellite phases replace higher Cu:S phases and are rarely replaced by higher Cu:S phases (Fig. 4), and in one instance replaced by stoichiometric CuS (Fig. 3c,d).

Normalized compositions of copper sulfides show numerous metal-sulfur (Cu+Fe)/S ratios, but three distinct varieties are readily apparent. The most common copper sulfide variety has metal-sulfur ratios of  $1.80 \pm 0.05$ , which is the composition of digenite. Less common are the varieties of copper sulfides with metal-sulfur ratios of  $1.92 \pm 0.03$  and  $1.10 \pm 0.10$ . Five samples contained grains with compositions between 1.22 and 1.74, generally in quantities subordinate to one of the three main varieties, and generally deeper in the supergene blanket. Overall, (Cu+Fe):S ratios decrease slightly down-hole, with (Cu+Fe):S ratios  $<1.5$  predominant below 1400 ft. beneath the hole collar.

The most striking result was the lack of stoichiometric Cu<sub>2</sub>S in any sample analyzed. It is unclear if the lack of stoichiometric Cu<sub>2</sub>S is natural or, as noted by Pófsai and Buseck (1994), due to the transformation of chalcocite (Cu<sub>2</sub>S) to djurleite (Cu<sub>1.96</sub>S) when exposed to an electron beam.

Iron is present in nearly all samples analyzed from trace amounts up to 2.84 wt. %. Samples with higher metal-sulfur ratios have higher Fe content, predominantly those of 1.75 and above. The presence of Fe in more metal-rich phases is consistent with digenite, Cu<sub>1.8</sub>S, which requires Fe to be stable (Morimoto and Gyobu 1971).

The compositional paragenesis of supergene copper sulfides ranges from simple to complex. Many samples only show one generation of supergene sulfides, and therefore one generation of enrichment, which is compositionally homogeneous. In samples with multiple generations of enrichment (Figs. 3,4), sulfides of the early generation generally

have lower Cu:S ratios than those of later generation(s), but there are exceptions to the rule (Fig. 5). For example, the early generations at 1233.8 ft., 1379.6 ft., and 1615.3 ft. have higher metal-sulfur ratios than the later generations (Table 2).

Composition of supergene copper sulfides also varies down-hole. Overall, sulfides above 1514.2 ft. have a higher average metal-sulfur ratio than those at and below this depth (Fig. 5), corresponding to the chalcocite >> covellite + chalcopyrite noted by Enders (2000) in the upper portions of supergene ore. The highest metal-sulfur ratios in MOR-4511 are between 971.3 ft. and 1146.0 ft., and average 1.87.

## DISCUSSION

### *Comparison of natural and synthetic secondary sulfides*

The compositions of supergene copper sulfides in MOR-4511 are very similar to those from other copper deposits and synthetic phases seen in leach experiments. Goble and Smith (1973) show large populations of natural copper sulfides at Cu:S ratios of 1.0, 1.75, 1.2, 1.3, 1.1, and 1.6; and Whiteside and Goble (1986) show products from leaching of synthetic digenite in acidified ferric sulfate solution have large composition populations at  $1.76 \pm 0.06$ ,  $1.1 \pm 0.05$ , and  $1.31 \pm 0.03$  respectively. MOR-4511 overlaps with natural supergene copper sulfide and synthetic leach product populations at Cu:S ratios of  $1.80 \pm 0.05$ ,  $1.1 \pm 0.10$ , and  $1.25 \pm 0.05$ .

### *Ore textures as evidence of supergene fluid composition*

Descending fluids containing  $\text{Cu}^{2+}$ ,  $\text{Fe}^{2+}$ , and  $\text{Fe}^{3+}$  from high in the supergene blanket will react with hypogene pyrite and chalcopyrite to form the ore textures seen in MOR-4511. Chalcopyrite shows replacement by high and low Cu:S phases throughout the enrichment blanket. These textures are related to the activity of copper and iron ionic

species in solution. Replacement of chalcopyrite by high or low Cu:S phases is dependent on the activity of  $\text{Cu}^{2+}$  according to reactions (6) and (7) (e.g. Titley and Mazoras):



Many examples of what appears to be high Cu:S phases replacing chalcopyrite could also be high Cu:S phases replacing an initial generation of low Cu:S phases replacing chalcopyrite. In other samples, high Cu:S phases are unambiguously form as a direct replacement of chalcopyrite.

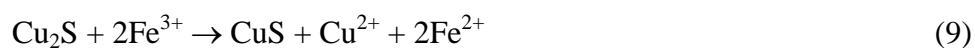
Within fault zones and high in the supergene blanket, where activity of both  $\text{Cu}^{2+}$  and  $\text{Fe}^{2+}$  could be high due to leaching and/or high pyrite-chalcopyrite ratio, the formation of high Cu:S phases directly from chalcopyrite will be favored according to reaction (6). Low Cu:S phases will be favored according to reaction (7) when the concentrations of  $\text{Cu}^{2+}$  and  $\text{Fe}^{2+}$  are low, either due to reaction of most  $\text{Cu}^{2+}$  and  $\text{Fe}^{2+}$  higher in the blanket, reduced access to supergene fluids, decreasing pyrite-chalcopyrite ratio of hypogene ore, or a combination of all three factors.

Pyrite is also replaced by copper sulfides, but only by high Cu:S phases and never to the extent of chalcopyrite when both are in close proximity, and there appears to be no relationship with depth. Titley and Mazoras (1995) suggest pyrite replacement by chalcopyrite is governed by the reaction of pyrite with dissolved Cu according to reaction (8):

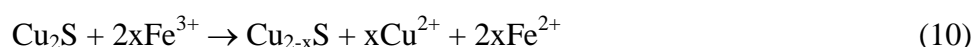


Lack of appreciable pyrite replacement by copper sulfides when both pyrite and chalcopyrite are present in the same sample, and the lack of any pyrite replacement when only low Cu:S phases replace chalcopyrite indicate a dependence of the replacement of pyrite by copper sulfides on the concentration of  $\text{Cu}^{2+}$  in solution. Without dissolved iron species in solution, pyrite replacement requires almost 3 moles of  $\text{Cu}^{2+}$  for each mole of pyrite, whereas chalcopyrite replacement requires only 1 mole of  $\text{Cu}^{2+}$ .

High and low Cu:S phases replace one another throughout MOR-4511. The most common replacement is high Cu:S phases replacing low Cu:S phases, but the reverse happens in several samples. Low Cu:S phases only replace higher Cu:S phases deep in the hole: at 1233.8 ft. and below, and in one instance, stoichiometric CuS replaces sulfides of 1.1 and 1.6 metal-sulfur ratio (1615.3 ft.). These textures are represented by the replacement of chalcocite by covellite according to (Walsh and Rimstidt 1986):



For phases in between chalcocite and covellite, the overall reaction becomes (Hiskey and Wadsworth, 1981):



Reactions (9) and (10) moving to the right are perhaps an example of progressive leaching of Cu, under oxidizing conditions, from an older generation of enrichment as the water table is lowered. More reducing conditions, or higher activity of  $\text{Cu}^{2+}$  and  $\text{Fe}^{2+}$  could move reactions (9) and (10) to the left, replacing pre-existing low Cu:S phases from an earlier period of enrichment.

## FUTURE WORK

### *Effect of crystal structure on formation of copper sulfides*

Despite the high precision of the microprobe analyses in this study, names of minerals in the Cu-S system cannot be unambiguously applied to the studied phases, because of similar optical properties of many phases and their structures remain unknown. Small grain size and thinness of rims on pyrite or chalcopyrite hampered efforts at obtaining X-ray diffraction (XRD) data. Single-crystal XRD was attempted on some of the blue-remaining covellites, but the crystals were too small and poorly formed to obtain a reasonable diffraction pattern. Future study would call for electron-backscatter diffraction (EBSD), which can show the crystal system of small grains using an SEM.

Whiteside and Goble (1986) propose the mineralogy of the phase undergoing alteration has a direct effect on which new copper sulfide will form. Their experiments show a copper sulfide with structure based on cubic close-packed (ccp) S atoms (digenite  $\text{Cu}_{1.8}\text{S}$ ) will be leached by removal of Cu atoms only, leaving the ccp S layers intact, forming a metastable polymorph of yarrowite or spionkopite (Whiteside and Goble 1986). While our results show minerals within yarrowite compositional range do indeed replace minerals within digenite compositional range, the structural identity of minerals in MOR-4511 cannot be reported. Small grain size and the porous nature of the samples renders them ill suited for X-ray crystallography.

## Conclusions

The chemistry and intergrowths of supergene sulfides in the Western Copper area of the Morenci mine have been examined in detail. Three main textures are present within the sulfides: partial to complete replacement of chalcopyrite, partial replacement of

pyrite, and partial to complete replacement of one another. Dominant (Cu+Fe):S ratios are  $1.80 \pm 0.05$ ,  $1.92 \pm 0.03$ , and  $1.10 \pm 0$ . Higher (Cu+Fe):S ratios are found higher in the blanket and within and/or near fault zones. Mineral intergrowths suggest formation of high versus low (Cu+Fe):S minerals is controlled by concentrations of  $\text{Cu}^{2+}$ ,  $\text{Fe}^{3+}$  and  $\text{Fe}^{2+}$  in supergene solutions, degree of access to supergene solutions, hypogene ore grade, and/or wallrock composition.

#### ACKNOWLEDGEMENTS

Freeport McMoRan Inc. provided samples and funding for this study. Robert A. Jenkins of FMI delivered the core and provided background information on DDH MOR-4511. BNS wishes to thank Frank K. Mazdab and Eric Seedorff for review of the manuscript and helpful comments on chemistry.

## REFERENCES

- Anderson, J.A. 1982. Leached capping and techniques of appraisal, in Titley, S.R., ed. *Advances in geology of the porphyry copper deposits, southwestern North America*: Tucson, University of Arizona Press, p. 275-295.
- Córdoba, E.M., Muñoz, J.A., Blásquez, M.L., González, F., Ballester, A. 2008. Leaching chalcopyrite with ferric ion. Part I. General aspects. *Hydrometall.* 93, 81-87.
- Dutrizac, J.E., MacDonald, R.J.C. 1974. The kinetics of dissolution of covellite in acidified ferric sulphate solutions. *Can. Metall. Q.* 13:3, 432-433.
- Enders, M.S. 2000. *The Evolution of Supergene Enrichment in the Morenci Porphyry Copper Deposit, Greenlee County, Arizona*. PhD Diss., Univ. of Arizona, 517 pp.
- Enders, M.S., Knickerbocker, C., Titley, S.R., Southam, G. 2006. The Role of Bacteria in the Supergene Environment of the Morenci Porphyry Copper Deposit, Greenlee County, Arizona. *Economic Geology* 101, 59-70.
- Ferguson, A.C., and Enders, M.S. 2000. Digital geologic map and cross sections of the Clifton-Morenci area, Greenlee County, Arizona: Arizona Geological Survey Map DGM-01, map scale 1:24,000, 14 pp, 3 map sheets and metadata.
- Goble R.J. 1981. The leaching of copper from anilite and the production of a metastable copper sulfide structure. *Can. Miner.* 19, 583-591.
- Goble R.J. 1985. The relationship between crystal structure, bonding and cell dimensions in the copper sulfides. *Can. Miner.* 23, 61-76.

- Goble, R.J., Smith, D.G.W. 1973. Electron microprobe investigation of copper sulfides in the Precambrian Lewis Series of S.W. Alberta, Canada. *Can. Miner.* 12, 95-103.
- Hiroyoshi, N., Miki, H., Hirajima, T., Tsunekawa, M. 2000. A model for ferrous-promoted chalcopyrite leaching. *Hydrometallurgy* 57, 31-38.
- Hiskey, J.B., Wadsworth, M.E. 1981. Electrochemical processes in the leaching of metal sulfides and oxides. *Jour. Macromol. Sci.-Phys.* 303-325.
- Morimoto, N., Gyobu, A. 1971. The composition and stability of digenite. *Am. Miner.* 56, 1889-1909.
- Pófszai, M., Buseck, P. 1994. Djurleite, digenite, and chalcocite: Intergrowths and transformations. *Am. Miner.* 79, 308-315.
- Seedorff, E., Dilles, J.H., Proffett, J.M. Jr., Einaudi, M.T., Zurcher, L., Stavast, W.J.A., Johnson, D.A., Barton, M.D. 2005. Porphyry Copper Deposits: Characteristics and Origin of Hypogene Features. *Econ. Geol.* 100<sup>th</sup> Anniversary Volume, 251-298.
- Sillitoe, R.H. 2005. Supergene oxidized and enriched porphyry copper and related deposits: *Economic Geology* 100<sup>th</sup> Anniversary Volume, 723-768.
- Sillitoe, R.H., Clark, A.H. 1969. Copper and copper-iron sulfides as the initial products of supergene oxidation, Copiapó mining district, northern Chile. *Am. Miner.* 54, 1684-1710.
- Sullivan, J.D. 1933. Chemical and Physical Features of Copper Leaching. *Trans. Am. Inst. Min. and Metall. Eng.* 106, 515-546.

- Titley, S.R., Mazonras, D.C. (1995). Processes and products of supergene copper enrichment: Arizona Geological Society Digest 20, 156-168.
- Walsh, C.A., Rimstidt, J.D. 1986. Rates of reaction of covellite and blaubleibender covellite with ferric iron at pH 2.0. Can. Miner. 24, 35-44.
- Whiteside, L.S., Goble, R.J. 1986. Structural and compositional changes in copper sulfides during leaching and dissolution. Can. Miner. 24, 247-2.

## FIGURE CAPTIONS

Figure 1. Location map, from Enders et al. (2006). Western Copper (WC) is at middle right in the lower right hand inset.

Figure 2. Reflected light photomicrographs (plane polarized light) demonstrating the relationship of supergene copper sulfides with pyrite and chalcopyrite in MOR-4511. (a) Chalcopyrite (brassy yellow) is mostly replaced by high Cu:S phase (bluish gray, 1.85 M:S) at 829.1 ft., while the associated pyrite (light yellow) is relatively untouched; field is 2 mm wide. (b) At 656.2 ft. no chalcopyrite is present, and pyrite (light yellow) is rimmed and partially replaced by high Cu:S phase (gray, 1.93 M:S); field is 2 mm wide.

Figure 3. Reflected light photomicrographs (plane polarized light) and BSE images (b,d) copper sulfides replacing chalcopyrite. (a) Two generations of copper sulfides (mottled gray to bluish gray and blue) veining and replacing chalcopyrite (brassy yellow) at 1445.1 ft; field is 1 mm wide. Despite the mottled appearance of the higher Cu:S phase in reflected light (gray to bluish gray), BSE imaging (b) shows the mineral to be compositionally homogeneous (brighter); metal-sulfur ratios are given on the BSE image. (c) Chalcopyrite replaced by covellite-like copper sulfides at 1615.3 ft; light gray porous area is graphite from carbon coating, field is 0.5 mm wide. Here the copper sulfides appear to be one phase under reflected light, but BSE imaging (d) shows them to be three separate phases; metal-sulfur ratios are given on BSE image. Cpy = chalcopyrite.

Figure 4. Reflected light photomicrographs showing copper sulfides replacing one another. (a) Gray, porous high Cu:S (1.80) replacing blue to light blue, low Cu:S (1.14) at 676.5 ft; plane polarized light, field is 1 mm wide. (b) Scratched grain

with rim of blue to light blue low Cu:S (1.21) replacing mottled bluish gray to gray high Cu:S (1.83); plane polarized light, field is 1 mm wide. (c) Same field of view as (b), but with crossed nicols to demonstrate the extent of replacement. Mineral with brownish internal reflections to the high right of copper sulfide grain is monazite.

Figure 5. Graph of metal-sulfur ratios down-hole in MOR-4511. High metal-sulfur phases predominate above 1514.2 ft., and overall metal-sulfur ratios are lower towards the base of the supergene blanket.

FIGURES

Figure 1

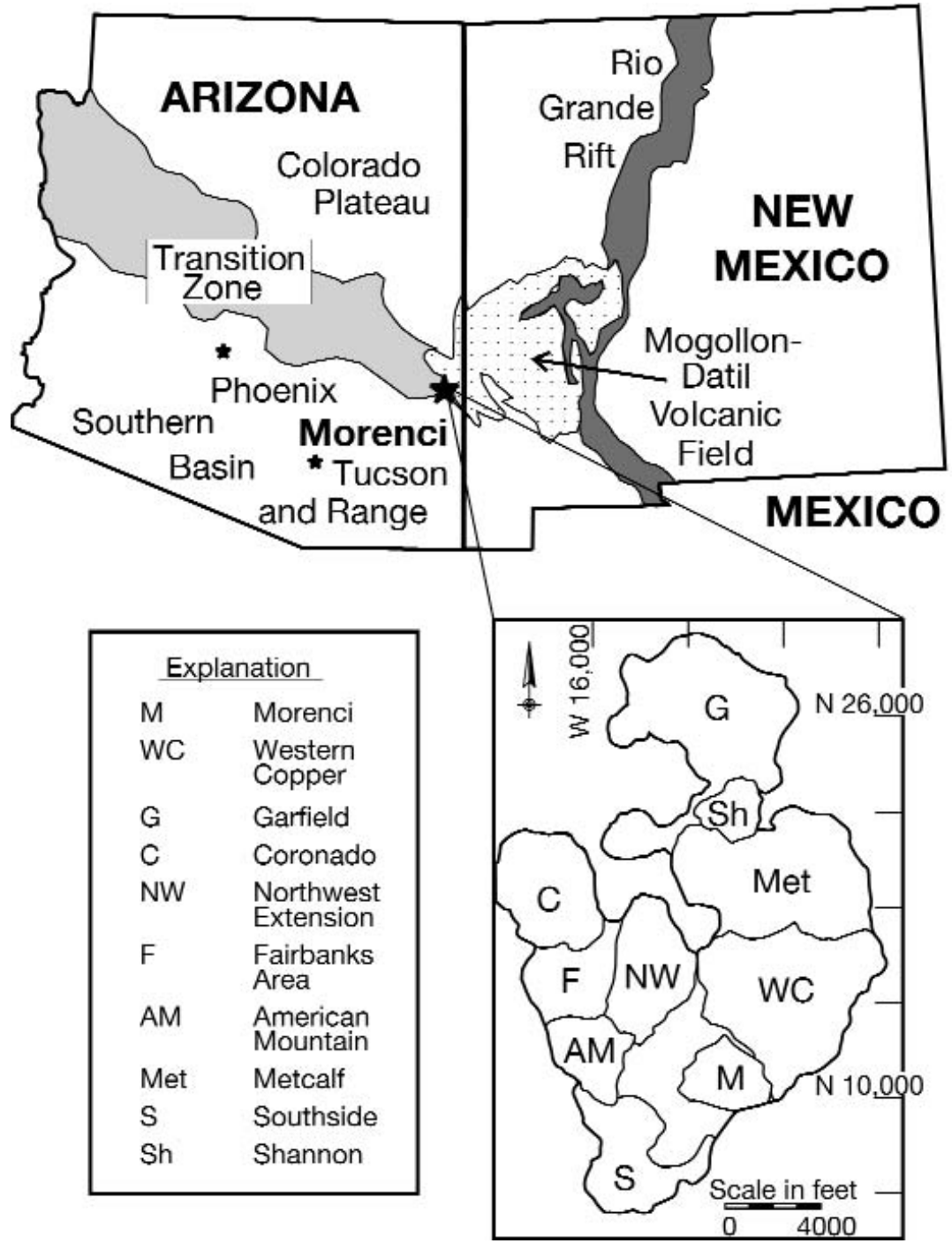


Figure 2

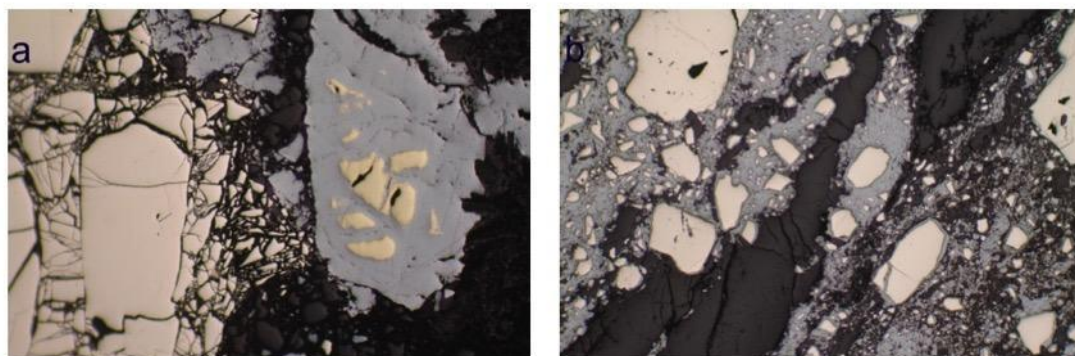


Figure 3

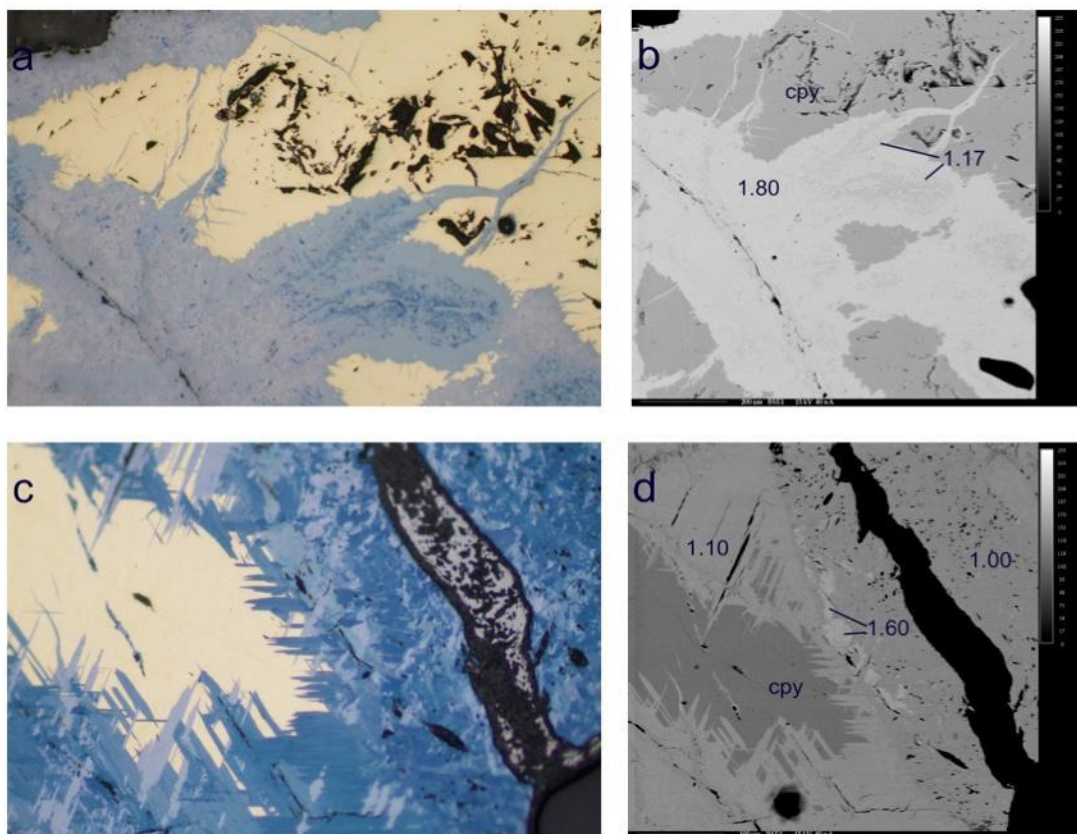


Figure 4

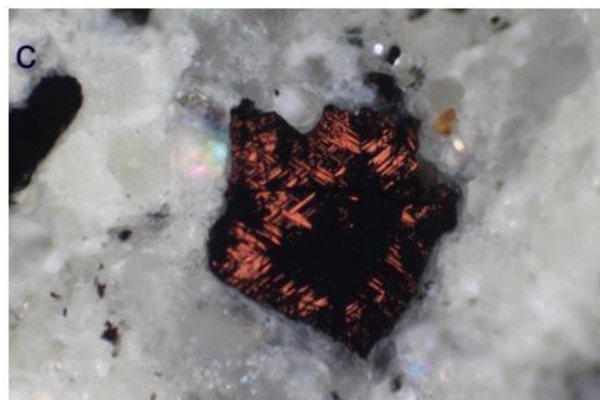
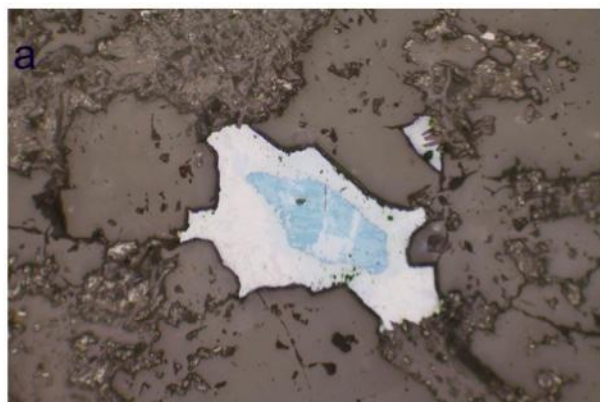
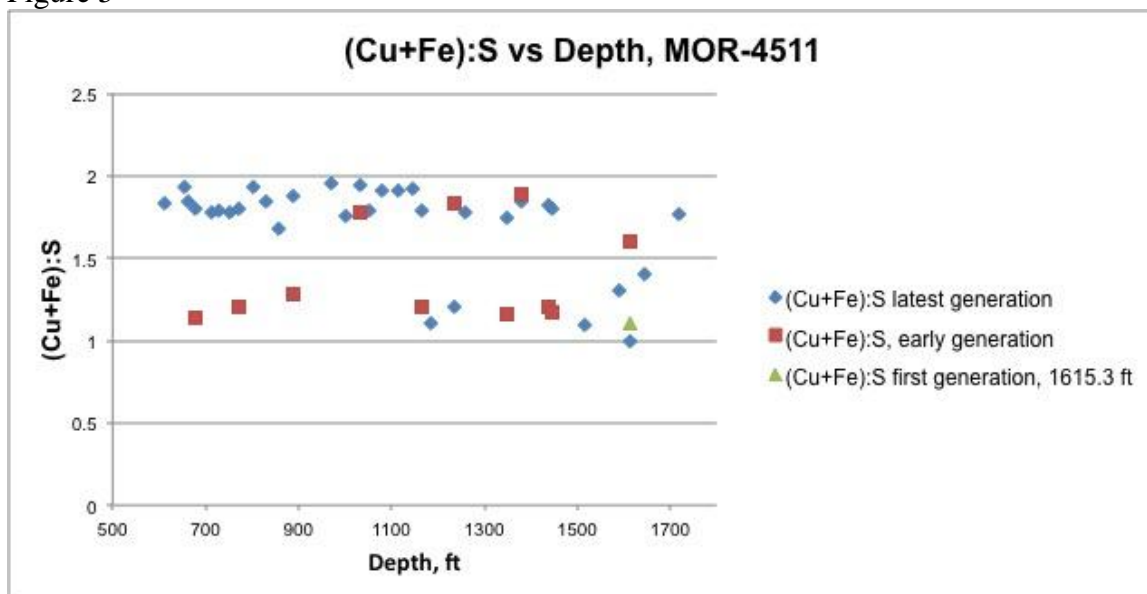


Figure 5



## TABLE EXPLANATORY NOTES

Table 1. Minerals in the system Cu-S.

Table 2. Metal-sulfur [(Cu+Fe):S] ratios by depth in MOR-4511. Data for intervals with multiple generations are listed in order of formation.

## TABLES

Table 1

Name	Formula	Cu:S	Space Group	Packing of S atoms
<b>Chalcocite</b>	<b>Cu<sub>2</sub>S</b>	<b>2</b>	<b>P2<sub>1</sub>/c</b>	<b>hcp</b>
<b>Djurleite</b>	<b>Cu<sub>31</sub>S<sub>16</sub></b>	<b>1.96</b>	<b>P2<sub>1</sub>/n</b>	<b>hcp</b>
<b>Digenite*</b>	<b>Cu<sub>9</sub>S<sub>5</sub></b>	<b>1.8</b>	<b>R-3m</b>	<b>ccp</b>
Roxbyite	Cu <sub>1.78</sub> S	1.78	C2/m?	?
<b>Anilite</b>	<b>Cu<sub>7</sub>S<sub>4</sub></b>	<b>1.75</b>	<b>Pnma</b>	<b>ccp</b>
Geerite	Cu <sub>8</sub> S <sub>5</sub>	1.6	R-3m?	hcp
Spionkopite	Cu <sub>1.32</sub> S	1.32	R-3m?	hcp
Yarrowite	Cu <sub>1.125</sub> S	1.125	P-3m1?	hcp
<b>Covellite</b>	<b>CuS</b>	<b>1</b>	<b>P6<sub>3</sub>/mmc</b>	<b>hcp</b>
Sakuraiite	Cu,Zn,Fe,In,Sn)S	1	Pm3m?	ccp?
<b>Villamaninite</b>	<b>CuS<sub>2</sub></b>	<b>0.5</b>	<b>Pa3</b>	<b>ccp</b>

Note: \*Digenite is stable only in the system Cu-Fe-S.

Bold entries have known crystal structures. Uncertain space groups are followed by "?"

Table 2

Name	Formula	Cu:S	Space Group	Packing of S atoms
<b>Chalcocite</b>	<b>Cu<sub>2</sub>S</b>	<b>2</b>	<b>P2<sub>1</sub>/c</b>	<b>hcp</b>
<b>Djurleite</b>	<b>Cu<sub>31</sub>S<sub>16</sub></b>	<b>1.96</b>	<b>P2<sub>1</sub>/n</b>	<b>hcp</b>
<b>Digenite*</b>	<b>Cu<sub>9</sub>S<sub>5</sub></b>	<b>1.8</b>	<b>R-3m</b>	<b>ccp</b>
Roxbyite	Cu <sub>1.78</sub> S	1.78	C2/m?	?
<b>Anilite</b>	<b>Cu<sub>7</sub>S<sub>4</sub></b>	<b>1.75</b>	<b>Pnma</b>	<b>ccp</b>
Geerite	Cu <sub>8</sub> S <sub>5</sub>	1.6	R-3m?	hcp
Spionkopite	Cu <sub>1.32</sub> S	1.32	R-3m?	hcp
Yarrowite	Cu <sub>1.125</sub> S	1.125	P-3m1?	hcp
<b>Covellite</b>	<b>CuS</b>	<b>1</b>	<b>P6<sub>3</sub>/mmc</b>	<b>hcp</b>
Sakuraiite	Cu,Zn,Fe,In,Sn)S	1	Pm3m?	ccp?
<b>Villamaninite</b>	<b>CuS<sub>2</sub></b>	<b>0.5</b>	<b>Pa3</b>	<b>ccp</b>

Note: \*Digenite is stable only in the system Cu-Fe-S.

Bold entries have known crystal structures. Uncertain space groups are followed by "?"

## APPENDIX 1: PETROGRAPHIC DESCRIPTIONS

This appendix contains petrographic descriptions of polished sections from each interval of drill hole MOR-4511 examined in this study. They are arranged by depth, beginning with the interval closest to the hole collar. Descriptions focus on hypogene and supergene sulfide mineralogy and degree of replacement of hypogene sulfides by supergene sulfides.

## Petrographic descriptions

**612.4 ft.** Primary pyrite and chalcopyrite replaced by a bluish gray copper sulfide, pyrite

>> chalcopyrite. Copper sulfide is isotropic, possibly digenite. Many larger copper sulfide masses contain tiny cores of chalcopyrite, indicating nearly total replacement of chalcopyrite. Some pyrite grains have thin (<0.01 mm) rims of copper sulfide, indicating incipient alteration.

**656.2 ft.** Fault zone containing irregular, sharp-edged pyrite grains in a quartz matrix, oriented along movement planes. Pyrite is the only hypogene sulfide, no chalcopyrite is present. All pyrite grains have a thin (~0.01 mm) rim of steely gray, isotropic copper sulfide. In areas with high pyrite density, copper sulfide forms the matrix. Under crossed polarizers, quartz matrix exhibits a reddish staining.

**664.0 ft.** Fault zone containing irregular, sharp-edged pyrite grains in a quartz-feldspar-mica matrix. Pyrite grains contain scattered inclusions (<5%) of hypogene chalcopyrite and hematite. No chalcopyrite present outside of pyrite. Bluish gray copper sulfide fills very thin (<<0.01 mm) fractures within pyrite grains and forms rims on some grain surfaces. Scattered grains of copper sulfide (~0.2 mm and smaller) are present in the matrix. Under crossed polarizers, the matrix exhibits reddish to brownish-yellow staining.

**676.5 ft.** Hypogene pyrite grains disseminated throughout quartz-mica-feldspar matrix accompanied by scattered grains of supergene copper sulfides. Pyrite contains scattered (<1%) inclusions of chalcopyrite, but no chalcopyrite is visible outside of pyrite grains. Blue to bluish gray copper sulfides predominantly occupy

interstices of quartz crystal aggregates, with some pyrite grains exhibiting very thin rims of bluish gray copper sulfide. Grains of pure copper sulfides are composed of pleochroic (dark blue to sky blue) rims around cores of bluish gray material, indicating bluish gray copper sulfide predates blue phase.

**714.0 ft.** Numerous irregular, sharp-edged pyrite grains in a matrix of quartz and mica.

Very rare inclusions of chalcopyrite are present in pyrite but no chalcopyrite is visible outside of pyrite grains. Steely gray copper sulfide forms thin rims ( $\ll 0.01$  mm) on pyrite grains and forms matrix of smaller pyrite aggregates.

**727.1 ft.** Shattered pyrite grains in a matrix of quartz and feldspar. No chalcopyrite is present. Steely gray copper sulfide forms discontinuous rims on pyrite grains and fills fractures within grains. Some pyrite grains appear to have been moved post-enrichment, with neighboring grains having copper sulfide rims which match across fractures.

**753.8 ft.** Hypogene chalcopyrite within quartz veinlets with feldspar envelopes. No hypogene pyrite is present. Chalcopyrite exhibits partial to total replacement by steely gray copper sulfide. Enrichment is restricted to veinlets.

**771.4 ft.** Subhedral to euhedral pyrite grains disseminated throughout a quartz-feldspar-mica matrix. Chalcopyrite is only present as inclusions within pyrite. Pyrite grains exhibit thin rims of steely gray copper sulfide. Copper sulfide forms thick fillings in interstices of pyrite aggregates.

**803.0 ft.** Scattered anhedral pyrite grains disseminated throughout a quartz-feldspar-mica matrix. Pyrite grains contain very rare inclusions of chalcopyrite. Steely

gray copper sulfide fills veinlets within matrix and forms rims on pyrite grains.

Under crossed polarizers, the matrix exhibits yellowish brown staining.

**829.1 ft.** Shattered pyrite and chalcopyrite grains occurring within a fault zone, with pyrite >> chalcopyrite. Chalcopyrite grains are 30-60% replaced by bluish gray copper sulfide as rims and veinlets. One chalcopyrite grain contains a veinlet of secondary bornite, itself mostly replaced by the bluish gray copper sulfide. Pyrite grains exhibit no replacement to the thinnest of rims of copper sulfide.

**859.3 ft.** Anhydral pyrite grains disseminated throughout a quartz-feldspar-mica matrix. The only other hypogene sulfide visible is molybdenite; no chalcopyrite is present in the sample. Pyrite grains exhibit very thin rims and fracture fillings of steely gray copper sulfide.

**888.8 ft.** Hypogene pyrite disseminated through a quartz-feldspar-mica matrix, cut by a quartz veinlet containing secondary copper sulfides. No chalcopyrite is visible in the sample. Copper sulfide grains appear to be aggregates of a pleochroic dark blue to sky blue sulfide and a steely gray sulfide. Blue copper sulfide is concave to steely gray sulfide, and occurs toward the centers of aggregates, indicating it predates the steely gray phase.

**940.8 ft.** Quartz veinlets containing laths of molybdenite with no other sulfides visible.

**971.3 ft.** Quartz veinlets containing laths of molybdenite. One ~0.2 mm grain of steely gray supergene copper sulfide is hosted in a molybdenite veinlet.

**1000.6 ft.** Fault zone containing shattered, sharp-edged pyrite grains within a matrix of quartz and mica. No other hypogene sulfides are present. Bluish gray copper sulfide occurs as rims to 0.1 mm thick on smaller pyrite grains.

- 1031.5 ft.** Anhedral pyrite disseminated throughout quartz-feldspar-mica matrix, with chalcopyrite occurring within a quartz veinlet. Secondary steely gray copper sulfide occurs as rims on or complete replacements of chalcopyrite, and incipient (very thin) rims on pyrite.
- 1054.0 ft.** Scattered anhedral pyrite grains disseminated within quartz-feldspar-mica matrix or within clayey fractures. No chalcopyrite is visible. Pyrite grains exhibit thin rims of steely gray copper sulfide.
- 1080.8 ft.** Anhedral pyrite grains disseminated throughout a quartz-mica matrix. No chalcopyrite is visible. Steely gray copper sulfide occurs as distinct masses within mica or as thin rims on pyrite grains. Distinct copper sulfide masses possibly complete replacements of chalcopyrite.
- 1115.5 ft.** Scattered anhedral grains of hypogene pyrite in a quartz matrix. Supergene copper sulfides occur as distinct grains of a steely gray phase within quartz. Pyrite is unaltered. Distinct grains of copper sulfide possibly complete replacements of chalcopyrite.
- 1146.0 ft.** Scattered anhedral grains of hypogene pyrite in a quartz-feldspar-mica matrix. No chalcopyrite is visible in the sample. Supergene copper sulfide occurs as steely gray monomineralic masses within quartz veinlets. Pyrite is unaltered. Copper sulfide possibly a replacement of chalcopyrite.
- 1166.9 ft.** Supergene copper sulfides filling interstices of quartz crystals within veinlets. No hypogene sulfides are visible in the sample. Supergene sulfides are two distinct phases: a pleochroic dark blue to sky blue phase and a steely gray phase.

The blue phase occurs as cores of aggregates and is veined by the steely gray phase, indicating it formed first.

**1184.6 ft.** Quartz-feldspar-mica matrix cut by a quartz veinlet containing hypogene chalcopyrite. Rare pyrite is disseminated throughout the matrix. The chalcopyrite is rimmed and veined by a pleochroic dark blue to sky blue copper sulfide. Isolated monomineralic grains of copper sulfide are also present. Pyrite is unaltered.

**1233.8 ft.** Fault zone containing cataclastic pyrite, chalcopyrite, and supergene copper sulfides; distal to the fault zone the quartz-feldspar matrix contains disseminated subhedral to anhedral pyrite and chalcopyrite with supergene copper sulfide grains. Copper sulfide in the fault zone occurs as monomineralic steely gray material, forming rims/replacements of chalcopyrite, discrete grains of copper sulfide, and very rarely rims on pyrite. The pyrite itself is sieve textured and contains approximately 10% inclusions of chalcopyrite, bornite, hematite, and sphalerite. Disseminated copper sulfides away from the fault zone occur predominantly as discrete grains with relict chalcopyrite cores. Two copper sulfide minerals are present: an outer rim of a covellite-like phase around a core of steely gray phase. The steely gray phase was the first to form, followed by the covellite-like phase away from the fault zone only.

**1260.0 ft.** Quartz-feldspar-mica matrix containing disseminated pyrite and supergene copper sulfide, cut by quartz veinlets containing pyrite, molybdenite, and supergene copper sulfide. Copper sulfide in both disseminated and veinlet occurrences is monomineralic, exhibiting a steely gray color. No chalcopyrite is

visible in the sample, and the pyrite is unaltered, indicating any chalcopyrite present was completely replaced. Molybdenite is unaltered.

**1350.3 ft.** Numerous 1-2 mm quartz veinlets cutting quartz-feldspar-mica matrix with disseminated pyrite. Veinlets contain blue, covellite-like supergene copper sulfide complexly intergrown with a bluish gray copper sulfide, while pyrite in the matrix exhibits rims of bluish gray copper sulfide, itself rimmed by blue copper sulfide. No hypogene sulfides are present in the quartz veinlets. Rims of blue copper sulfide around bluish gray copper sulfide indicate the bluish gray phase formed first.

**1379.6 ft.** Large (4 mm) veinlet cutting quartz-feldspar matrix containing chalcopyrite, pyrite, and supergene copper sulfide. Pyrite is unaltered, whereas chalcopyrite is rimmed and ~25% replaced by steely gray copper sulfide. Possibly two generations of copper sulfide are present: a less porous, brighter phase against chalcopyrite which is rimmed by a darker, very porous phase exhibiting a platy habit. The platy phase has the habit of covellite-like phases replacing other copper sulfides elsewhere in the DDH, possibly indicating a replacement of the covellite-like phase by the steely gray phase.

**1436.3 ft.** Quartz-feldspar-mica matrix containing disseminated pyrite and copper sulfide, and cut by a quartz veinlet with pyrite and minor chalcopyrite. Copper sulfide within matrix is small grains <0.1 mm, steely gray in color. Pyrite in matrix is unaltered, as are pyrite and chalcopyrite in veinlet.

**1445.1 ft.** Quartz veinlet cutting through rock. Veinlet contains chalcopyrite and pyrite; chalcopyrite is ~75% replaced by copper sulfides. Two copper sulfides are

present: a bluish gray phase and a blue pleochroic phase. The pleochroic phase resembles covellite, and occurs as relicts surrounded on all sides and veined by bluish gray phase, indicating the covellite-like phase formed first.

**1514.2 ft.** Quartz veinlet cutting rock. Veinlet contains pyrite and chalcopyrite. Pyrite contains <5% inclusions, predominantly chalcopyrite with rare hematite and sphalerite. Chalcopyrite is unaltered or exhibits thin rims of supergene, covellite-like copper sulfide. Pyrite is unaltered.

**1589.2 ft.** Rare anhedral grains of pyrite and chalcopyrite disseminated throughout matrix. Chalcopyrite exhibits very thin rims of supergene covellite-like copper sulfide. Pyrite is unaltered.

**1615.3 ft.** Quartz veinlet cutting rock. Subhedral pyrite is disseminated throughout matrix. Quartz veinlet contains chalcopyrite, which is altered to supergene covellite-like copper sulfides. Chalcopyrite is >75% altered, with coarse grained (~0.25-0.5 mm) covellite-like sulfides oriented along crystallographic planes of the former chalcopyrite. Along fractures the coarse grained sulfide is altered to a second generation of finer-grained material which exhibits a slightly darker blue color in its darkest position than the coarse phase. Pyrite is unaltered.

**1628.5 ft.** Quartz-pyrite-chalcopyrite veinlet cutting rock. Pyrite appears shattered; all edges are sharp. Scattered inclusions of chalcopyrite in pyrite. No supergene sulfides present.

**1643.5 ft.** Quartz veinlet cutting rock. Veinlet contains pyrite and minor chalcopyrite. Pyrite has rare inclusions of chalcopyrite. Minor pyrite and chalcopyrite grains are disseminated throughout the matrix; some chalcopyrite grains exhibit

incipient rims of supergene, bluish copper sulfide. The rims are very thin ( $\ll 0.1$  mm).

**1692.0 ft.** Quartz-feldspar-biotite rock. Two pyrite grains are visible in the sample; no chalcopyrite is present. Pyrite grains are unaltered.

**1712.8 ft.** Zone of shattered pyrite in quartz matrix. Pyrite grains exhibit sharp edges with no evidence of alteration of any kind. Pyrite contains scattered ovoid inclusions of chalcopyrite.

**1718.7 ft.** 5 mm grain of chalcopyrite in quartz matrix with no visible pyrite.

Chalcopyrite grain is heavily fractured and altered along fractures to supergene steely gray copper sulfide phase. Copper sulfide shows incipient alteration to isotropic dark gray mineral (sphalerite?).

## APPENDIX 2: MICROPROBE DATA AND NORMALIZATIONS

The data presented in Table A2-1 are the microporobe analyses for each interval containing supergene sulfides listed by interval (in feet beneath hole collar), average weight percent of elements from multiple spots, total weight percent, and atoms per formula unit (apfu) Cu and Fe normalized to 1.00 apfu sulfur. Some intervals contain multiple generations of supergene sulfides, and these are listed by the interval followed by a number (1) to (3).











Table A2-1, continued

Interval (ft)	1615.3 (2)	1615.3 (3)	1643.2	1718.7
Element				
Cu	68.59	66.34	70.45	76.93
Fe	0.06	0.02	2.13	0.76
S	31.46	33.42	26.42	22.85
Total	100.11	99.78	99.00	100.54
Atoms				
Cu	1.10	1.00	1.35	1.70
Fe	0.00	0.00	0.05	0.20
S	1.00	1.00	1.00	1.00

**APPENDIX D: HYPOGENE MINERALOGY AND ZONING OF CORDILLERAN  
POLYMETALLIC LODES AND CONSTRAINTS ON HYDROTHERMAL  
FLUID EVOLUTION AT BISBEE, COCHISE COUNTY, ARIZONA**

Benjamin N. Schumer<sup>1</sup>, Richard W. Graeme III<sup>2</sup>, and Mark D. Barton<sup>1</sup>

This paper was prepared for submission to Economic Geology

<sup>1</sup>*Department of Geosciences, University of Arizona, 1040 E. 4th Street, Tucson, Arizona  
85721-0077, USA*

<sup>2</sup>*478 Dart Rd., Bisbee, AZ 85603*

## ABSTRACT

The historic mining area at Bisbee, Arizona, USA, exploited Cordilleran base-metal lodes hosted in sandy to argillaceous carbonate rocks of Paleozoic age where they take the form of peneconcordant to discordant replacement bodies and hydrothermal breccias. The lodes surround the 199-201 Ma Sacramento stock, a composite, porphyritic granitic intrusion which was mined for supergene-enriched copper in the intensely acid altered upper part of a porphyry copper system. Using a selection of samples from large, now inaccessible underground workings, this study examines the paragenesis, zoning, and ore petrography of hypogene sulfide minerals and places them in time-space evolution of an ore-forming system.

Lode-type ores in the Bisbee district are either dominated by either Cu or Zn-Pb sulfides; both types are associated with silica-pyrite bodies. Copper ores can be further divided into three types: chalcopyrite-rich ore consisting of the assemblage chalcopyrite + chlorite + quartz  $\pm$  pyrite and accessory Cu-Bi-sulfides, tellurides, and minor oxides of U, Sn, and W; bornite-rich ore containing the assemblage bornite + pyrite + muscovite with associated tennantite and Cu-Sn-W-V sulfides; and a chalcocite-rich type containing one of three assemblages: enargite/luzonite + pyrite + kaolinite-dickite, chalcocite-digenite + pyrite + kaolinite-dickite and covellite + kaolinite-dickite. Zinc-lead mineralization consists of dominant sphalerite and galena, with minor tennantite-tetrahedrite, and minor chalcopyrite in a gangue of quartz and pyrite, or alabandite, galena, and tennantite-tetrahedrite in a gangue of quartz and rhodochrosite. District scale zoning ranges from proximal Cu-dominant ore adjacent to the Sacramento intrusive complex outwards to Zn-Pn (Mn) > Cu ores restricted to the northwestern and southeastern fringes of the district. At the scale of individual ore bodies, silica-pyrite

cores are overprinted and surrounded by zones of bornite- and/or chalcopyrite-rich ores and a discontinuous fringe of hematite  $\pm$  magnetite with or without pyrite. Within the copper-dominant zone, paragenetically late enargite/luzonite, chalcocite-digenite, and covellite rich ores have been found only the southern portion of the district. Zinc-lead ores occur distal to and stratigraphically above copper ores in individual lodes, and Mn ores occur stratigraphically above Zn-Pb bodies.

At the ore body scale, magnetite + chlorite + quartz and then hematite + anhydrite + chlorite + quartz were the first minerals to replace limestone, followed by pyrite. Chalcopyrite + chlorite + quartz  $\pm$  pyrite followed pyrite, bornite + pyrite + muscovite followed chalcopyrite and local enargite, chalcocite-digenite, or covellite followed bornite. As time progressed during mineralization, the fringe of hematite  $\pm$  magnetite moved outwards in space from fluid sources, followed by chalcopyrite and finally bornite and/or chalcocite-rich ores. Sphalerite, galena and/or alabandite with calcite  $\pm$  rhodochrosite were deposited farthest from the fluid source. Relict sphalerite and galena in chalcopyrite and bornite indicate progressive dissolution and redeposition of sphalerite and galena throughout the mineralization process. These relationships indicate the sulfidation state of fluids increased at any given point in space as time progressed during mineralization, following closely with decreasing FeS in sphalerite. Multiple mineralizing events are suggested by local reversals, such as tennantite replacing enargite and bornite exsolving from chalcocite-digenite and an overall change from Bi-dominated accessory minerals to As, Sb, and Te-dominated accessory minerals.

## INTRODUCTION

Cordilleran base-metal lodes represent an important source of Cu, Zn, and Pb. These mesothermal deposits are high-grade, commonly distal parts of larger magmatic-hydrothermal systems that also form economic skarn and porphyry deposits (Meyer et al. 1968; Einaudi, 1982). They typically form massive sulfide vein or replacement bodies showing well-developed metal zonation on a district scale, and contain mineral assemblages varying from low to high sulfidation state (Catchpole et al. 2012). Numerous well-studied examples exist worldwide, such as Elshitsa, Bulgaria (Kouzmanov et al. 2005), Colquijirca, Peru (Bendezú and Fontboté 2009), Butte, Montana (Meyer et al. 1968, Reed et al., 2013), and Magma, Arizona (Hammer and Peterson 1968; Manske and Paul, 2002).

The Bisbee district (also known as the Warren district), Cochise County, Arizona, produced 7.7 billion pounds (3.5 million tonnes) Cu, 355 million pounds (161,364 tonnes) Zn, 324 million pounds (147,273 tonnes) Pb, 10 million pounds (4,545 tonnes) Mn as well as 100 million oz (1,466 tonnes) Ag and 2.7 million oz (39.5 tonnes) Au from 1877 to 1975 (Graeme, 1981). Over the century of mining, most production came from small, (typically <25,000-ton) replacement lodes in Paleozoic limestone and breccias surrounding a Jurassic intrusive complex that contained lower-grade, supergene-enriched porphyry copper mineralization (Bryant and Metz, 1966).

Despite the long history of mining at Bisbee, only a few, limited studies on the hypogene sulfide ores have been published. Prior to the turn of the 20<sup>th</sup> century, most of the ore produced was supergene copper carbonates, oxides, and native Cu. In fact Ransome (1904) was skeptical of the value of sulfide ore in the district. Early studies focused

primarily on individual ore bodies: Schwartz and Park (1932) and Carpenter (1941) studied the mineralogy and zoning of the Campbell ore body, and Peng (1948) studied the Mountain Maid ore body in the Junction mine. Hogue and Wilson (1950) focused on Zn-Pb ores, and were the first to discuss a district-scale zonation from Cu-rich ores in the center to Zn-Pb dominated ores on the western and southern fringes. Later studies, such as Bain (1952), Bryant (1964), and Nye (1968) developed a more generalized district-wide paragenesis and zonation for ore minerals. In a number of cases, their interpretations conflict with the interpretations of Schwartz and Park (1932) and Carpenter (1941), perhaps due to the complexity and zoning of hypogene ore. The most recent studies at Bisbee are Criddle et al. (1989), who studied the diverse mineralization of the Campbell orebody and suggest tellurides were formed much later than the Cu-Zn-Pb ores, and Friehauf (1997), who studied hematite-bearing ores from a number of deposits throughout the district.

This contribution presents a new study of paragenetic relationships between ore and gangue minerals from ore bodies throughout the Bisbee district, and uses mineral chemistry to interpret the conditions and evolution of magmatic-hydrothermal fluids responsible for mineralization. The mineralogical study includes reinvestigation of paragenetic relationships from well-studied mines such as the Campbell and Cole, but also new data on sulfides from previously unstudied mines including the Copper Queen, Holbrook, and Southwest. This study also represents the first pairing of paragenetic data and mineral chemistry from the Bisbee district. The data and interpretations presented here are not intended to be comprehensive. Mines at Bisbee have been closed since 1975, rendering most exposures of hypogene sulfides inaccessible. Samples used in this study

are from public and private collections, many of which were collected by one of us (RWG) during his tenure underground at Bisbee as an engineer for Phelps Dodge, Inc. Our goal is to establish paragenetic relationships of lode ores across the entire Bisbee district and infer something about ore-forming conditions and how they may have varied in space and time.

## GEOLOGY OF THE BISBEE DISTRICT

The general geology of the Bisbee District, briefly summarized here, has been extensively studied, notably by Ransome (1904), Bryant (1964), Bryant and Metz (1966), and Nye (1968), and presented in summary here. Bisbee is located in Cochise County, Arizona, close to the US-Mexico border in the southern extension of the Basin and Range province (Fig. 1). Productive deposits are mostly located in the Copper Queen block, a fault-bounded window of deformed Paleozoic and Mesozoic igneous and sedimentary rocks and the Proterozoic Pinal Schist (Fig. 2).

Pinal Schist, the oldest rock in the district, and underlies all sedimentary rocks. Common throughout Arizona, the Pinal schist is a variably metamorphosed mix of turbidites, volcanics, and amphibolites with ages between 1650 and 1720 Ma (Lang et al., 2001; Meijer, 2014). In the Bisbee area, the Pinal Schist is predominantly quartz-sericite schists and phyllites of a pale green to white color on fresh surfaces and pinkish to tan on weathered surfaces (Stegen et al., 2005).

### *Sedimentary Rocks*

Marine and clastic sedimentary rocks unconformably overlie the Pinal Schist. The sandy to conglomeratic Middle Cambrian Bolsa Quartzite directly overlies the Pinal Schist, and is conformably overlain by the Abrigo Limestone of Middle to Upper Cambrian age (Bryant and Metz 1966). Basal Abrigo is shaly, while the middle and upper

portions are crystalline and finely bedded, becoming progressively more sandy until terminating in a sandstone layer called the Parting quartzite (Nye 1968).

Upper Devonian Martin Limestone disconformably overlies the Abrigo Limestone. Lower in the section, the Martin is shaly, becoming more massive higher in the section (Nye 1968). Conformably overlying the Martin limestone is thick bedded, crinoidal Middle Mississippian Escabrosa Limestone (Bryant and Metz 1966). Pennsylvanian-Permian rocks of the Naco Group disconformably overlie the Escabrosa. Three of six named members of the Naco Group (Gilluly et al., 1954) are present in the mining area at Bisbee: the Horquilla Limestone; clastic sediments, limestone, and dolomite of the Earp Formation, both of Middle to Upper Pennsylvanian age; and the Colina Limestone of Permian age (Bryant and Metz 1966).

Lower Cretaceous Bisbee Group sedimentary rocks unconformably overlie the Naco Group. The basal member of the Bisbee Group, the Glance Conglomerate, is composed of pebble to boulder-sized rocks of all earlier formations, notably including clasts of the intrusive rocks and gossan derived from nearby Sacramento Hill (Bryant and Metz 1966). Shale and sandstone of the Morita Formation conformably overlie the Glance, and are in turn conformably overlain by Mural Limestone and shales and sandstones of the Cintura Formation (Bryant and Metz 1966).

### *Igneous Rocks*

Igneous rocks of the Bisbee district are predominantly intrusives of quartz monzonite composition. The former Sacramento Hill area in the center of the Bisbee district gave its name to the Sacramento stock, a composite intrusive area intruding rocks on both sides of the Dividend Fault (Lang et al. 2001). Bryant and Metz (1966) describe two intrusive

units along with two distinct breccias in the Sacramento stock, however later drilling and mapping has identified another intrusive phase (Stegen et al., 2005). Crosscutting bodies of later porphyry intrusions and breccias indicate the unit exposed predominantly to the north of the Dividend Fault, and also within the Lavender pit, is the first intrusive phase (Bryant and Metz, 1966; Nye, 1968). This is the “older porphyry” or quartz-porphyry of earlier writers (e.g. Bryant and Metz, 1966; Graeme, 1981), but is in fact a quartz monzonite (Stegen et al., 2005). The second intrusive phase is the “younger porphyry” or feldspar-quartz porphyry (Bryant and Metz, 1966), which is another quartz monzonite porphyry exposed in the Lavender pit and as numerous dikes and sills in the underground workings, often termed “underground porphyry” in earlier studies.

Dating of the older and younger porphyries by U-Pb gives an age of  $198.9 \pm 1.6$  Ma for the older porphyry and  $200.0 \pm 0.6$  Ma for the younger porphyry (Lang et al., 2001). These ages are inconsistent with those interpreted by crosscutting relationships, suggesting either the crosscutting relationships were interpreted incorrectly, the U-Pb dates are in error, or perhaps both are incorrect.

Drilling programs completed after the studies of Bryant and Metz (1966) and Nye (1968) identified two other intrusive units. The Cochise Porphyry, another quartz monzonite, crops out north of the Dividend Fault and was interpreted by Lang et al. (2001) to be part of the older porphyry. Lang et al. (2001) dated the Cochise Porphyry at  $200.0 \pm 0.8$  Ma. Drilling beneath the Lavender pit identified the Warren Porphyry, a  $201.4 \pm 0.8$  Ma quartz-monzonite porphyry, which Lang et al. (2001) believe to be the source of the younger porphyry.

Each intrusive phase generated breccias. Brittle deformation during the intrusion of the older porphyry resulted in a halo of igneous-matrix breccia on the margins of the older porphyry (Lang et al., 2001). Hydrothermal activity accompanying the intrusion of younger porphyry resulted in “intrusive breccias”: heterolithic fragments of all earlier rock types, including silica-pyrite, ranging from angular to rounded in a rock flour matrix transported to its present location along preexisting structures (Bryant, 1968). These hydrothermal breccias form dikes, sills, and irregular bodies ranging in size from thin films to masses over 100 meters in diameter, and commonly contain significant Cu mineralization and advanced argillic alteration (Stegen et al., 2005).

### *Structure*

The Copper Queen block is bound to the north by the Dividend fault, a major northwest-striking, southwest-dipping normal fault, which cuts off the Sacramento intrusive complex and separates Paleozoic and older Mesozoic rocks of the Copper Queen block from a footwall block consisting mostly of Pinal Schist intruded by Jurassic igneous rocks and overlain by Cretaceous sedimentary rocks to the north (Fig. 2).

Another NW-trending normal fault, the Escabrosa (also given as White Tailed Deer by Nye, 1968), bounds the Copper Queen block to the south. Bryant and Metz (1966) interpreted the northwest-striking normal faults to doming by intrusion of the 175 Ma Juniper Flat granite (Lang et al., 2001), however this interpretation seems unlikely since the Glance Conglomerate is younger than the Juniper Flat and dramatically thickens to the S of the Dividend Fault.

Between the Dividend and White Tailed Deer faults, numerous smaller fault zones, striking roughly N20E, dip northwest and cut the Copper Queen block into many small

pieces (Fig. 2) (Bryant and Metz, 1966). Normal movement along these fault zones downdrop rocks of the Copper Queen block stepwise to the southeast (Nye 1968). Porphyry dikes emanating from the Sacramento complex followed some of these fault zones, and show some degree of brecciation indicating post-intrusion movement along the faults (Nye, 1968). Dates of 199-201 Ma on the Sacramento complex indicate the northeast-striking normal faults are the earliest period of deformation, which was followed by post-ore, northwest-striking normal faults such as the Dividend Fault dropping the Copper Queen Block.

#### GENERAL FEATURES OF MINERALIZATION AND HYDROTHERMAL ALTERATION

Mineralization in the Copper Queen block is associated spatially and genetically with the intrusive rocks of the Sacramento complex. Carbonate rocks and intrusive rocks contain distinctly different styles of alteration and mineralization. Carbonates silicified and pyritized forming large replacement bodies. In places they retain relicts of the original bedding and chert horizons (Peng, 1948). They are commonly spatially associated with dikes and irregular bodies of younger porphyry (Bryant and Metz, 1966).

Mineralizing fluids variably altered the intrusive rocks of the Sacramento complex. South of the Dividend Fault, older porphyry is intensely altered to advanced argillic assemblages of quartz-pyrophyllite and minor dickite, alunite, apatite, and rutile with over 15% pyrite (Bryant and Metz, 1966). This commonly destroys textures. Younger porphyry is altered to quartz-sericite-pyrite, with preservation of the original igneous textures (Bryant and Metz, 1966). Dikes and sills of what has been termed younger porphyry by numerous authors were frequently encountered during underground mining, sometimes associated with ore, and always significantly altered. Though often termed

quartz-sericite-pyrite alteration (e.g. Bryant and Metz, 1966), Peng (1948) describes dike rock of a green color, which was altered largely to calcite-pyrite-chlorite-quartz, indicating probable propylitic alteration. Beneath the Lavender pit, Warren Porphyry contains stockwork-controlled K-silicate alteration with minor chalcopyrite-molybdenite mineralization (Lang et al., 2001).

North of the Dividend Fault, the Cochise porphyry exhibits shallow advanced argillic alteration similar to the older porphyry south of the Dividend Fault. Deep zones of the Cochise Porphyry contain stockwork hosted to pervasive sericitic and K-silicate alteration with associated chalcopyrite-molybdenite mineralization (Stegen et al., 2005). Copper mineralization in the shallow advanced argillic zone was leached and redeposited as supergene chalcocite to form the Cochise Zone ore body (Lang et al., 2001).

Small, irregular bodies of skarn are found at the southern and northeastern margins Sacramento complex and proximal to dikes between the Cole and Dallas shafts. Lang et al. (2001) note an early, anhydrous skarn stage consisting of garnet, diopside, vesuvianite, and minor wollastonite followed by a later hydrous stage consisting of epidote, amphibole, chlorite, calcite, and quartz. Patchy chalcopyrite-magnetite mineralization is associated with the hydrous skarn stage (Lang et al. 2001). The timing of skarn alteration at Bisbee and its relationship to intrusions and Cordilleran base-metal mineralization remain enigmatic, and will be discussed further below.

South of the Dividend fault, replacement ore bodies radiate out from the Sacramento complex in a semicircular fashion, associated with the early northwest dipping normal faults (Bryant and Metz 1966). Ore was mined from every Paleozoic rock unit, but the most productive horizons were the upper Abrigo Limestone, all of the Martin Limestone,

and the lower Escabrosa Limestone, localized where the host formation underwent intense fracturing or brecciation, sometimes associated with folds in limestones and embayments in porphyry dikes (Bryant and Metz 1966). Ore bodies formed as replacements of the host limestones.

Ore bodies are localized predominantly by the degree of ground preparation by faults, fracture zones, and breccia zones, presumably because they acted as fluid conduits in contrast to what may have been lower permeabilities in the host carbonates (Nye, 1968). Many breccia zones became host to ores, especially within the Sacramento complex, though some breccias were apparently impermeable and acted as fluid traps (Bryant, 1968). Porphyry dikes and sills, many of which intruded along northeast-striking normal faults, also acted as structural traps for ore fluids, and ore bodies commonly occur in embayments or beneath igneous bodies (Peng, 1948). The shape of orebodies depends mostly on the amount of ground preparation in the Martin, Escabrosa, and Naco Group rocks, and ranges from sub-horizontal to sub-vertical pipe-like bodies (“chimneys”) and even vein-like bodies between two parallel fault zones (Bryant and Metz 1966). In some cases, tongues of ore extend laterally out along bedding planes from more vertical bodies in the host limestone forming mantos. In contrast, the Abrigo Limestone was predominantly host to mantos where thin carbonate horizons interlaminated with shaly material were selectively replaced by ore minerals (Bryant, 1964). Most orebodies are small, under 25,000 tons, but a few, such as the Campbell orebody, are over 1 million tons (Graeme, 1981).

A large fraction of the mineralization in the northern part of the district was oxidized to mixtures of supergene carbonates and oxides and was the source of many of the

mineral specimens for which the district is famous (Graeme, 1981). Nevertheless some hypogene materials remain there which when combined with the deeper unoxidized ores from the southern and western parts of the district provide the basis for this study.

## MATERIALS AND METHODS

Due to inaccessibility of nearly all sulfide stopes in the underground workings at Bisbee, samples of sulfide ore were obtained from the University of Arizona Mineral Museum and the private collection of one of us (RWG), many of them collected by the Graeme family of during mining. A conscious effort was made to use samples from as many mines across the district as possible, as well as to multiple ore types from the same mine.

A portion of each sample was cast in epoxy resin and polished for examination under the ore microscope. Special care was taken to identify stable mineral assemblages and paragenetic relationships between minerals such as caries (replacement) texture, reaction rims, and inclusion relationships. Compositions of sphalerite, tennantite-tetrahedrite series minerals, and stannoidite was measured using a CAMECA SX50 electron microprobe at the Lunar and Planetary Laboratory, University of Arizona, with beam conditions of 20 kV and 40 nA.

## ORE MINERALOGY

### *Overview*

Studying ore samples from throughout the district allowed us to further subdivide sulfide ores into one Zn-Pb type and three Cu-dominant types: a chalcopyrite-rich type, a bornite-rich type, and a chalcocite-rich type. Ore types are described in terms of mineral associations and assemblages, including gangue. In order to gain a more complete understanding of mineralogy, our data are combined with the results of previous studies

insofar as possible. Massive silica-pyrite bodies, though generally barren of ore minerals, are discussed along with the ores because of their intimate association with ores of all types.

#### *Silica-pyrite bodies*

Throughout the Bisbee district, large bodies of massive to bedded silica-pyrite formed by replacement of impure limestone and breccias. Silica-pyrite alteration is uniform throughout the district: fine-grained subhedral to euhedral (pyritohedral) pyrite, generally under 0.5 mm in maximum dimension, comprises 40 percent or more of the rock, the balance being quartz. Pyrite in silica-pyrite bodies is usually free from inclusions except for rare subhedral to anhedral quartz grains, and this paucity of inclusions serves to differentiate silica-pyrite rock from pyrite occurring in other ore types. On the basis of Bryant (1968), Bartos (1989) estimated that the Bisbee district contains over of 500 million tons of silica-pyrite.

Silica-pyrite bodies commonly form the core-zone of ore bodies, but are characteristically poorly mineralized. Extent of mineralization appears to depend on porosity and/or degree of fracturing: quartz-rich samples from the Cole shaft contain ore sulfides around the periphery of or within fractures through angular silica-pyrite blocks, while other samples from the Campbell and Junction shafts shows copper sulfides filling interstices of pyrite grains as well as cementing large fractures (Fig. 10).

#### *Chalcopyrite-rich types*

Chalcopyrite-rich ore occurs throughout the district. In this ore type, chalcopyrite is the dominant Cu-bearing phase, forming between 20% and 90% of the ore, and is always associated with pyrite, hematite, and/or magnetite; sometimes all four minerals are

present in the same sample (Fig. 7b). Quartz and chlorite are the dominant non-opaque gangue minerals. There are two assemblages in chalcopyrite-rich ore type, which share quartz, pyrite, and Bi-sulfosalts but differ in that one appears to be pyrite-destructive and has hematite and anhydrite, and the other appears to be pyrite stable. Both types contain a distinctive suite of trace element-rich accessory minerals. The pyrite-destructive assemblage predominates, and occurs on the distal edges of ore bodies. Common associates are specular hematite, partial to complete hematite pseudomorphs after magnetite, quartz, chlorite (clinochlore), and anhydrite. Within the pyrite-destructive assemblage, pyrite occurs as subhedral grains exhibiting a shattered texture. Grain edges, including internal fracture surfaces within larger aggregates, have a wavy, scalloped appearance and do not match up with one another, indicating replacement (Fig. 7b). Grains are sieve textured and contain up to 20% inclusions of quartz, anhydrite, hematite, and minor chalcopyrite. Chalcopyrite content appears to follow pyrite content: within an ore body chalcopyrite and pyrite diminish outward as hematite and magnetite content increases to the complete exclusion of sulfides, forming the barren hematite shell surrounding ore bodies. The pyrite-stable assemblage was noticed only within ores from the 2000 level of the Campbell shaft. There, pyrite occurs as euhedral cubes within chalcopyrite, and contains up to 20% ovoid inclusions of chalcopyrite and Bi-sulfosalts without hematite. Accessory minerals common to both assemblages are sphalerite, scheelite, and uraninite. Sphalerite occurs as anhedral grains within pyrite or chalcopyrite and in one case as star-shaped exsolutions in chalcopyrite from the Gardner shaft.

Sphalerite inclusions in chalcopyrite from the Gardner shaft and Higgins mine are unzoned, and contain 1.7 and 1.1 mole % FeS, respectively. The sample from the

Gardner shaft also contains sphalerite inclusions in pyrite, which are higher in iron at 7.5 mole % FeS, though separated by less than 0.5 millimeters from the sphalerite in chalcopyrite (Table 1).

#### *Telluride-bearing ore*

Ores containing precious and base metal tellurides are rare at Bisbee, historically known only from the deep levels of the Campbell ore body in the silica-pyrite core (Criddle et al., 1982). We found telluride-bearing ores in the Higgins mine in addition to the famous occurrence in the Campbell, in both cases always occurring with chalcopyrite and pyrite. Samples from the deep levels of the Campbell orebody contained two different associations: 1) chalcopyrite associated with the tellurides altaite, kostovite, sylvanite, stützite and the sulfides tennantite, stannite, and sphalerite, and 2) chalcopyrite associated with kiddcreekite, colusite, tennantite, and native Te (Fig. 7e). Both occur as inclusions in large (often to over 1 cm), subhedral to euhedral pyrite crystals and as stringers containing highly resorbed cassiterite and scheelite between pyrite crystals in a gangue of quartz and calcite. Petrography of massive silica-pyrite from the Higgins mine revealed an association of chalcopyrite, tetradymite (Table 4), sphalerite, pyrite, and scheelite in a gangue of fluorapatite, chlorite, and quartz.

Pyrite grains are concave to chalcopyrite containing tellurides from both the Campbell and Higgins, however pyrite grains from the Higgins contain inclusions of specular hematite and hematite pseudomorphs after magnetite while those from the Campbell shaft do not. The textural similarity of the telluride-bearing associations to assemblages in chalcopyrite-rich ores suggests that both are overprints of earlier pyrite,

though at different stratigraphic levels within ore bodies: a high-level overprint of pyrite (after hematite) in the Higgins and an overprint of silica-pyrite in the Campbell.

### *Bornite-rich types*

Bornite-rich ore is both widespread and uniform. The principal minerals are bornite, chalcopyrite, chalcocite and pyrite together with quartz and muscovite in two assemblages: bornite + pyrite + muscovite + quartz  $\pm$  chalcopyrite and bornite + chalcocite + muscovite + quartz  $\pm$  pyrite. In both assemblages, pyrite composes 30% or less of the ore, and occurs as anhedral to euhedral grains. Anhedral pyrite appears shattered and veined by bornite and minor chalcopyrite. Grain edges are scalloped and concave to bornite and chalcopyrite but do not appear widened where bornite has replaced the chalcopyrite, indicating pyrite is stable with respect to bornite. These anhedral grains typically contain small relict hematite grains with or without chalcopyrite as well as ovoid chalcopyrite inclusions, indicating this type of pyrite predates bornite. Euhedral crystals of pyrite are dominantly of pyritohedral habit and lesser cubic habit and average 1-2 mm in size but may reach 3 cm in maximum dimension. Pyrite crystals are sieve textured, containing up to 20% inclusions of bornite, chalcocite-digenite, tennantite, and minor chalcopyrite, in rare cases exhibit skeletal growth along one or more edges, indicating they formed in equilibrium with bornite.

Bornite-rich ore contains a very complex suite of accessory minerals, such as tennantite, numerous Cu-Sn-V-W-In sulfides, sphalerite, and galena (Fig. 9a, b). Masses and stringers of chalcocite or chalcocite-digenite are always separated from chalcopyrite by at least a thin film of bornite, but typically occur at least several centimeters distant. Chalcocite and chalcocite-digenite show oriented or froth-like exsolutions from bornite,

generally in their centers, reminiscent of those from Butte, Montana, described by Sales and Meyer (1949). Bornite-chalcocite ore from the 1600 level of the Campbell shaft contains native gold, wittichenite, and Cu-Ag sulfides (Fig. 9e).

Many of the minor sulfides including tennantite, sphalerite, galena, and the Cu-Sn-V-W sulfides occur as anhedral grains or subhedral crystals within bornite, indicating formation prior to or during bornite formation. With the exception of kiddcreekite, these sulfides are present in nearly every sample of bornite examined. Kiddcreekite forms rounded, resorbed grains in bornite associated with tungstenite laths, or as subhedral overgrowths on colusite associated with Te-rich tennantite. Stannoidite and mawsonite occur as individual grains in bornite or as intergrowths, always with mawsonite overgrowing stannoidite. Stannoidite forms as reaction rims between sphalerite and bornite, typically overgrown by mawsonite on the bornite side.

#### *Mineral compositions in bornite-rich ore*

Sphalerite in bornite-rich ore is generally iron free, with one sample containing 0.04 mole % FeS (Table X sl comp). Sphalerite grains are unzoned but chalcopyrite diseased, and contain reaction rims and/or inclusions of stannoidite, mawsonite, and colusite however no Sn was detected during analysis.

Tennantite-group minerals in bornite-rich ore are dominated by tennantite (Table 3). Average tennantite contains 10.13 apfu Cu in M1 site, 1.68 apfu Zn in M2 and 3.60 apfu As in M3, though As is commonly substituted by up to 0.32 apfu Bi, 0.38 apfu Sb or 1.88 apfu. Grains are commonly zoned, with higher Bi, Sb, and Te values in cores.

The ideal formula of stannoidite is  $\text{Cu}_8(\text{Fe,Zn})_3\text{Sn}_2\text{S}_{12}$ . Iron and/or Zn are ordered two separate sites, one accommodating  $2\text{Fe}^{3+}$  and the other  $1\text{Fe}^{2+}$  or  $1\text{Zn}^{2+}$  (Kudoh and

Takéuchi, 1976). Bisbee stannoidite contains an average of 8.10 apfu Cu, 2.01 apfu Fe<sup>3+</sup>, 0.95 apfu Zn<sup>2+</sup> with no Fe<sup>2+</sup>, and 0.93 apfu Sn (Table 2).

#### *Chalcocite-rich ore types*

Ores containing a high proportion of chalcocite occur primarily in the southern portion of the district. They are composed primarily of Cu-sulfides and/or Cu-As sulfides. Chalcocite and digenite are the dominant Cu-sulfides, with covellite occurring separately and even more restricted in extent. They are often forming intergrown, and vein and replace bornite locally to the extent of forming massive “steely chalcocite” bodies containing islands of bornite (Fig. 10g). The dominant mineral assemblage is chalcocite/digenite + pyrite + kaolinite/dickite + quartz. Though macroscopically similar to the chalcocite-bornite ore from the bornite-rich zones, “steely chalcocite” is differentiated by a significantly lower bornite content of typically less than 10% and without distinct bornite exsolutions.

Hypogene covellite was recognized in samples from the Campbell, Junction, Cole, and Lavender pit mines. It occurs as striking botryoidal masses including minor pyrite and chalcopyrite with kaolinite on the edges of aggregates and between layers (Fig. 10c). Botryoidal covellite from the Lavender pit cements breccia composed of angular chalcopyrite and altered rock fragments. Chalcopyrite commonly overgrows the edges of covellite aggregates and in some cases completely surrounds individual covellite blades with scalloped edges concave to the chalcopyrite, indicating replacement.

Copper-arsenic sulfosalts (excluding tennantite) are very restricted in occurrence, recognized only in samples from the Campbell, Junction, and Cole shafts. Massive

enargite, luzonite, and tennantite-group minerals occur in the assemblage enargite/luzonite + pyrite + kaolinite/dickite + quartz.

Pyrite occurs as subhedral to euhedral crystals within massive enargite, chalcocite-digenite, and luzonite. The grains average 0.5 mm in size, but may attain sizes of over 1 cm. Grain edges often appear rounded, and the grains themselves may contain stringers and ovoid inclusions of bornite, tennantite, enargite, or digenite, however where these crystals border open spaces, the vug side is lined by mirror-bright pyrite crystals.

Every sample of enargite shows veining and replacement by tennantite (Fig. 10e,f). Relicts of bornite-chalcopyrite-pyrite intergrowths are scattered throughout enargite, indicating their formation prior to the bulk of enargite deposition. Luzonite is found in only one sample (R1166) from the Junction shaft as massive material containing scattered euhedral quartz and pyrite crystals. Grains of chalcostibite included in have reaction rims of Sb-rich enargite and tetrahedrite.

Chemical analyses of tennantite-group minerals from chalcocite-rich ores show compositions ranging from tennantite to tetrahedrite to goldfieldite (Fig. 5, 6). Tennantite-tetrahedrite from chalcocite-rich ore is unzoned and rich in Cu, Fe, and Ag but low in Zn, averaging 10.98 apfu Cu, 0.29 apfu Ag, 0.65 apfu Fe, 2.84, and 0.08 apfu Zn, with As averaging 3.66 apfu in tennantite and Sb 2.78 apfu/1.24 apfu As in tetrahedrite. Arsenian goldfieldite is rare, occurring primarily as resorbed, relict grains in enargite, and is zoned from between 1.98 and 2.58 apfu Te.

*Zn-Pb association*

Bodies rich in sphalerite and galena with abundant accessory pyrite and quartz are widespread at Bisbee, particularly in distal zones, where they directly replace carbonate rocks. Sphalerite, galena, and pyrite are the most common minerals, with subordinate chalcopyrite, alabandite, and rare tennantite-tetrahedrite. Quartz and the carbonates calcite, siderite, and rhodochrosite are the most common non-opaque gangue minerals. No hematite or magnetite was seen associated with Zn-Pb or Mn ores in this study.

Chalcopyrite disease (Barton and Bethke, 1987) is present in sphalerite from throughout the district, but is not present in all samples. The chalcopyrite blebs are often concentrated in distinct zones and oriented in a linear fashion, ranging from very fine-grained in earlier sphalerite to coarse-grained in later, vug-filling sphalerite. Sphalerite formed after pyrite, and galena appears to be concurrent to or later than sphalerite, growing on sphalerite and filling vugs in gangue. Tennantite group minerals form intimate intergrowths with sphalerite, indicating deposition at the same time or just after sphalerite.

Chalcopyrite disease is widespread, being more common in ores with carbonate-quartz-pyrite gangue than for ores with quartz-pyrite gangue. Zonation within sphalerite grains can be seen under the petrographic microscope as large bodies of chalcopyrite at the center of a sphalerite grain getting progressively smaller toward the edges, as well as growth bands rich in euhedral pyrite deposited on crystal faces before being overgrown by a later generation of sphalerite. This physical zonation is closely followed by chemical zonation, with grain centers containing up to 1.9 mole % FeS compared to a maximum of

0.3 mole % FeS at the rim (Table 1). In addition to Fe, sphalerite from the Zn-Pb orebodies also contains up to 1.5 wt. % Mn. Manganese content is relatively constant regardless of Fe zoning. Chemical analyses of tennantite-group minerals identified both tennantite and tetrahedrite in Zn-Pb ore. Tennantite is associated with zoned, low to moderate FeS sphalerite, galena, and chalcocopyrite in a distal extension of the Campbell ore body on the south side of the Campbell fault, and tetrahedrite is associated with unzoned, low FeS sphalerite and galena, also from the Campbell ore body but from the north side of the Campbell fault in the main ore body.

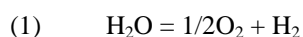
#### CONSTRAINTS ON CONDITIONS OF MINERALIZATION

Paragenetic relationships, zoning, mineral chemistry, and geology are used to interpret the conditions of formation including temperature, pressure, redox, sulfidation state, and possible reaction path(s) of fluids responsible for the formation of ores. Constraints on pressure are poor, however the late Paleozoic sedimentary cover at 200 Ma would have been no more than 2 km (Bryant and Metz, 1966) with the possibility of several km of early Mesozoic volcanic rocks as observed elsewhere in southern Arizona (Riggs and Busby-Spera, 1990). Likely pressures would have therefore been  $\leq 1$  km lithostatic. Maximum temperatures in the aureole were probably  $\leq 450^{\circ}\text{C}$  based on the dearth of skarns and extensive hornfels at the present level of exposure (Einaudi, 1982; Bowman, 1998). The ores themselves were probably a bit cooler, beginning with the early-formed silica-pyrite bodies and hydrothermal breccias formed prior to ore deposition (Bryant, 1964). A temperature of  $325^{\circ}\text{C}$  was used as an approximate temperature of ore deposition because of the dominance of enargite over its dimorph luzonite, the transition being approximately  $275^{\circ}\text{-}300^{\circ}\text{C}$  (Manske and Skinner, 1971), which correlates well with temperatures of  $302^{\circ}$  and  $325^{\circ}\text{C}$  (Table X, Tn comp.)

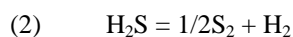
estimated using Fe-Zn exchange between unzoned tennantite-tetrahedrite and unzoned sphalerite as outlined by O'Leary and Sack (1987) and Sack et al. (1987). Similarly, the bornite-rich ores likely formed at  $T > \sim 250^\circ\text{C}$  based on exsolution of digenite from bornite (Grguric et al., 2000).

The sequence of sulfide and oxide bearing assemblages allows a first approximation of the oxidation and sulfidation states, and inferences about possible fluid evolution.

Figure 11 (cf. Einaudi et al., 2003) shows oxidation state in terms of the parameter  $R_H = \log (f_{\text{H}_2}/f_{\text{H}_2\text{O}}) \approx (X_{\text{H}_2}/X_{\text{H}_2\text{O}}) \propto \log f_{\text{O}_2}$  via:



and sulfidation state in terms of the parameter  $R_S = \log (f_{\text{H}_2}/f_{\text{H}_2\text{S}}) \approx (X_{\text{H}_2}/X_{\text{H}_2\text{S}}) \propto \log f_{\text{S}_2}$  via:



where  $X$  = mole fraction. As discussed in greater detail in the following section, the evolutionary sequence of fluids is uncertain. Silica-pyrite bodies are indicative of relatively sulfidized conditions and are commonly linked to igneous-hosted sericitic or advanced argillic alteration (e.g., James, 1976; Einaudi, 1982). The temperatures and relationship of silica-pyrite fluids to later mineralization is unknown.

For the Cu-Zn-Pb ores, the early proximal assemblages have magnetite and chalcopyrite with or without pyrite. These would be consistent with relatively high-T, S-rich fluids near the  $\text{SO}_2$ - $\text{H}_2\text{S}$  buffer (Fig 11a). Paragenetically later, pyrite-chalcopyrite, pyrite-bornite, and digenite/covellite-pyrite assemblages are considerably more sulfidized but consistent with similar moderately oxidized sulfur-rich fluids (Fig 11b). Such fluids are also compatible with enargite in place of tennantite, and the sulfidation of Sn and W

to make the accessory sulfides of these phases (stanoidite, tungstenite, etc.) in place of earlier cassiterite and scheelite. At varying stages, neutralization of these fluids by progressive reaction with carbonate-bearing rocks would drive them to lower sulfidation states consistent with the stability of late and distal pyrite, sphalerite, and hematite (cf. Einaudi et al., 2003).

The assemblage bornite + pyrite + muscovite + quartz replacing chalcopyrite + Mg-chlorite + quartz  $\pm$  pyrite coincides with the appearance of tennantite. Though the assemblage bornite + pyrite is above the tennantite +  $S_2$  = enargite buffer (Fig. 11a), Einaudi et al. (2003) note that the buffer may be several log units too low or that elevated concentrations of several elements, such as the Zn and Te found in Bisbee tennantite, could stabilize tennantite relative to enargite (Einaudi et al., 2003). Tennantite and enargite are soluble in low  $R_S$  and/or low  $H_2S$  and very oxidized or very reduced fluids, and therefore their precipitation require fluids with moderate  $R_H$  and  $R_S$  with low-moderate to moderate  $H_2S$  (Friehauf, 1998).

Native tellurium, tellurides, and sulfotellurides are associated with chalcopyrite, pyrite, and cassiterite or scheelite. These are consistent with relatively high  $fTe_2$  to form tellurides such altaite and stützite or very high to form native tellurium (Afifi et al., 1988a). Relative sulfidation state of these is suggested by the presence of altaite, which is limited by the altaite-galena buffer to the lower end of chalcopyrite + pyrite stability (Afifi et al., 1988a, b).

Sphalerite relicts show decreasing FeS from chalcopyrite-rich to bornite-rich ores, and massive sphalerite in Zn-Pb ore bodies shows a decrease in FeS with time from the cores of grains to rims or vug walls to vug fillings. The decreasing FeS is also associated

with increasing chalcopyrite disease. Increasing dissolved  $\text{Cu}^+$  would form chalcopyrite disease from Fe-rich sphalerite according to the reaction  $\text{ZnFeS}_2(\text{sphalerite}) + \text{Cu}^+ = \text{CuFeS}_2(\text{“disease”}) + \text{Zn}^{2+}$  (Barton and Bethke, 1987). Decreasing FeS with increasing chalcopyrite disease in sphalerite in Zn-Pb bodies, when correlated with decreasing FeS with time in sphalerite associated with Cu-rich ores is interpreted as progressive decrease of  $R_H$  and  $R_S$ .

### TIME-SPACE RELATIONSHIPS

Because replacement ores in the Bisbee district are predominantly from small, separate bodies, interpreting time-space relationships for the entire district becomes difficult because most samples are isolated in space from one another due to being collected over the span of 75 years, and certain types of ore (e.g. chalcocite-rich types) are found only in certain parts of the district. To combat these difficulties, we first examine the similarities in broad-scale zoning and paragenetic relationships in the northern part of the district and the southern part of the district, divided along an east-west line just below the Gardner shaft, and then discuss the differences. Notes on ore body scale zonation in the northern part of the district are taken from work done prior to 1975 (e.g. Hewett and Rove, 1930; Bryant, 1964).

#### *Zonation*

Ores are zoned at a broad scale from dominant Zn-Pb (-Mn) at the northwesterly and southern fringes, becoming more Cu-rich closer to the Sacramento complex. Copper and Zn-Pb ore bodies are predominantly sub-vertical, pipe or pod-like replacements tens to hundreds of meters in length with or without a centimeter to meter-thick shell of hematite  $\pm$  pyrite-chalcopyrite. Deposits are zoned inward from the hematite shell to massive Cu-sulfide ores around a core of silica-pyrite. Hematite content decreases steadily into the

Cu-sulfides until it is present only in the cores of pyrite crystals and finally lacking entirely. Within the massive sulfides, bornite-rich ore replaces chalcopyrite-rich ore. Rare tellurides and sulfotellurides are associated with chalcopyrite-rich ore. Where zinc-lead sulfides occur with Cu-sulfides in the same ore body, they are distal and/or stratigraphically above Cu-ores. Manganese ores occur stratigraphically above Zn-Pb and Cu ores (Hewett and Rove, 1930).

In the northern part of the district, ores were highly to completely oxidized however some sulfide-bearing material remained. Samples used in this study come from the Higgins, Copper Queen, Southwest, Holbrook, Sacramento, and Gardner mines in the Abrigo, Martin, and Escabrosa Limestones. Copper ores are limited to chalcopyrite-rich and bornite-rich types, though most bornite ores contain at least some hypogene chalcocite. Tellurides are very rare and only identified in samples from the Higgins mine. Tellurium is, however, present in tennantite substituting for As. Ores from the southern part of the district are much less oxidized. Samples used in this study originate from the breccias of the Lavender pit and replacements in the Cole, Dallas, Briggs, Denn, Junction, and Campbell mines in the Abrigo, Martin, and Escabrosa Limestones and Naco Group rocks. The main difference between ores from the southern part of the district and those from the northern part are the occurrence of chalcocite-rich ores in addition to chalcopyrite-rich and bornite-rich types.

The similarities between ores in the northern and southern parts of the district outweigh the differences. Mineralogical and paragenetic uniformity of ore zones from deposit to deposit suggests similar hydrothermal processes were at work over a wide area. Overall, the zonation in time (Fig. 3) and space is one of inner zones encroaching on

outer zones: magnetite replaced by hematite, hematite replaced by pyrite, chalcopyrite replaced by bornite + pyrite, in certain areas enargite/luzonite, digenite, or covellite replacing bornite, and finally Zn-Pb deposited distal to Cu ores (Fig. 4).

The most plausible explanation for the observed paragenetic relationships and zonation is several pulses of magmatic-hydrothermal fluid resulting from distinct intrusive events. The first intrusive event is the older porphyry. The associated fluid pulse would then be responsible for pervasive advanced argillic alteration of the older porphyry and formation of the silica-pyrite bodies throughout the district. A second intrusive event, the younger porphyry and associated dikes, resulted in the fluid pulse responsible for the hydrothermal breccias found throughout the district and sericitic alteration of the younger porphyry. Fluids associated with a possible third intrusive event were responsible for the formation of the Cu-Zn-Pb lodes.

One evolving fluid is most likely responsible for formation of the ore deposits. As this fluid cools and departs from its rock buffer, it could progressively form hematite, pyrite, chalcopyrite and bornite. Trace tellurium associated with all three ore types indicates one fluid of constant composition is responsible for their deposition. Tellurium is found as tellurides associated with chalcopyrite and is incorporated into tennantite associated with bornite or goldfieldite associated with enargite, indicating Te, and possibly As and Sb, were present in the fluid all along (cf. Friehauf, 1998). In areas where fluid flow was sufficiently high and/or wall rocks pervasively altered, enough sulfur may have been present to favor precipitation of enargite, digenite, or covellite, analogous to the Central Zone at Butte, Montana (Einaudi et al., 2003). This same fluid could also be responsible for formation of Zn-Pb ore bodies distal to Cu ores. Reduced

sulfur is required to saturate a solution with respect to sphalerite (Friehauf, 1998), thus Zn would stay in solution until activity of reduced sulfur reached the proper level, resulting in deposition of shalerite progressively farther away from the fluid source as mineralization progressed. The retrograde relationships tennantite replacing enargite, bornite exsolving from chalcocite-digenite, and chalcopyrite replacing covellite are present throughout high sulfidation assemblages at Bisbee. These indicate collapse of the system at the cessation of hydrothermal activity and declining sulfidation state as fluids cool.

Multiple fluid pulses could also have formed Cu-Zn-Pb ores. The observed retrograde relationships could be due to cooling of ore fluids in between distinct pulses of fluid. Separate fluid pulses could also be responsible for the change in accessory mineralogy from Bi-dominated chalcopyrite-rich ore to As, Sb, and Te-dominated bornite- and chalcocite-rich ores. This interpretation is unlikely, however, because fluids with low concentrations of reduced sulfur can deposit chalcopyrite and carry sufficient dissolved As to form tennantite or enargite at the correct conditions (Friehauf, 1998).

#### COMPARISON WITH OTHER Cu LODE SYSTEMS

Bisbee is similar to many other Cu-dominant Cordilleran polymetallic deposits worldwide (Table 7). Association in space and time of lodes and mineralized porphyry intrusions seems to be a common, but not necessary feature of these districts. Though the overall mineralogy of Cu lode systems may vary, especially from carbonate-hosted lodes to those hosted in igneous rocks, they share a broadly similar paragenesis and mineralogical/metallogenic zoning, indicating similar evolution of magmatic-hydrothermal fluids. Geometry of ore bodies also varies from carbonate-hosted to

igneous-hosted deposits, and even within the carbonate-hosted lodes. Accessory mineralogy is also broadly similar and characteristically complex.

#### *Carbonate rock hosted lodes*

Copper lodes hosted in carbonate rocks, or in districts containing both carbonate-hosted and intrusive-hosted lodes, exhibit broadly similar mineralogy and paragenetic relationships indicative of formation from oxidized, sulfur-rich fluids (Table 7). Pyrite-quartz replacement bodies, or vein fill in the Magma vein, are the earliest features noted in each district, and are followed by polymetallic mineralization. Geometry of pyrite-quartz and ore replacements are dependent on host rock permeability, and range from pipes/chimneys in massive limestone such as Bisbee and Morococha or mantos in more permeable limestones such as at Colquijirca, Magma, and locally at Bisbee. All districts exhibit zonation from Cu (center) to mixed Cu-Zn-Pb to outer Zn-Pb-Mn (Ag) except Magma, which is telescoped within the Magma fault vein from Cu at depth to Zn only at the very highest levels (Hammer and Peterson, 1968). Accessory mineralogy is also broadly similar: early Sn, W oxides followed by later sulfides of As, Sb, Bi as well as tellurides and sulfides of Sn, W, V. Replacement bodies at Magma, Colquijirca, and Bisbee also contain zones rich in iron oxides distal to major ore bodies. Only two of the carbonate-hosted lode systems compared here, Bisbee and Morococha, are related to porphyry Cu deposits.

#### *Igneous rock hosted lodes*

Copper lodes hosted in igneous rocks also exhibit similar mineralogy, paragenesis, and zoning to Bisbee, indicative of similar formation conditions from oxidized, high sulfidation state fluids. In the deposits compared here, ores occur as veins in intrusive

rocks of monzonitic composition, while at Elshitsa, Bulgaria, ores occur as massive replacement lodes and minor disseminations in andesitic to dacitic tuffs (Kouzmanov, 2009). Pyrite-quartz vein fill or replacement is the earliest mineralization in all districts, and is followed by polymetallic mineralization. Ores are zoned from central Cu to Cu-Zn-Pb to Zn-Pb-Mn (Ag) at Butte and Elshitsa, whereas Chuquicamata only has very minor Zn at the periphery of Cu ores, similar to the Magma vein. Accessory mineralogy is similar to the carbonate-hosted Cu lodes, with early Sn and/or W oxides and later sulfides of As, Sb, Bi, Sn, W, and V at Chuquicamata and Elshitsa, whereas the early Sn, W oxides and the later tellurides are absent or undocumented at Butte. All three igneous-hosted Cu lode systems compared here are related in time and space to a mineralized Cu porphyry deposit.

## CONCLUSIONS

Base metal lode deposits at Bisbee, Arizona, exploited Cu and lesser Zn-Pb ores. Lodes predominantly occur as chimney-like replacements of massive, argillaceous to sandy limestone and lesser mantos in highly argillaceous limestone or along bedding plane faults. Copper dominated ores are further subdivided into chalcopyrite-rich, bornite-rich, and chalcocite-rich types. Chalcopyrite-rich ores contain the assemblage chalcopyrite + chlorite + quartz  $\pm$  pyrite associated with lesser hematite, magnetite, and anhydrite, with accessory minerals dominated by Bi-sulfosalts or sulfotellurides and minor uraninite, scheelite, or cassiterite. Tellurides occur in chalcopyrite + pyrite assemblages in deep levels of the Campbell and Higgins mines. Bornite-rich ore is dominated by the assemblage bornite + pyrite + muscovite, and contains accessory tennantite and Cu-Sn-V-W sulfides. Chalcocite-rich ore is composed of three

assemblages: digenite-chalcocite + pyrite + kaolinite-dickite + quartz, enargite or luzonite + pyrite + quartz, and covellite + kaolinite-dickite + quartz. Zinc-lead ores are composed of the association sphalerite, galena, quartz, pyrite, tennantite-tetrahedrite, chlorite and/or lesser siderite. Manganese occurs as the association alabandite, rhodochrosite, and galena.

Iron oxides occur at the boundary between ores and limestone and were progressively followed by pyrite, which was in turn followed by the assemblages chalcopyrite  $\pm$  pyrite and finally bornite + pyrite. In the southern part of the district, enargite-luzonite, digenite-chalcocite, and covellite assemblages followed bornite assemblages. Bornite exsolves from digenite, late tennantite replaces enargite and late chalcopyrite replaces covellite. Relict sphalerite becomes depleted in FeS from chalcopyrite-rich ore to bornite-rich ore, and sphalerite grains in Zn-Pb ore bodies are zoned from higher FeS cores to lower FeS rims. Ores are zoned from Cu-rich proximal to the Sacramento intrusive complex to Zn-Pb (Mn) > Cu along the northwestern and southeastern margins of the district. At a small scale, zinc-lead ores occur stratigraphically higher and distal to Cu ores, and Mn ores occur stratigraphically higher than Zn-Pb ores. Sulfide ores form as discontinuous shells around a core of silica-pyrite, and a thin zone dominated by iron oxides occurs between Cu ores and unaltered limestone.

Paragenetic relationships, mineral chemistry, and zoning indicate oxidized magmatic-hydrothermal fluids were responsible for mineralization at temperatures between 450° and 325°C. Early replacements of impure limestone occurred at low  $R_H$ , high  $R_S$ , and low  $\Sigma S$  forming first magnetite, hematite, and finally pyrite. Ore formation began with

chalcopyrite + chlorite + quartz  $\pm$  pyrite, with bornite + pyrite + muscovite replacing the chalcopyrite assemblage, and finally enargite/luzonite + pyrite + kaolinite-dickite, chalcocite-digenite + pyrite + kaolinite-dickite and covellite + kaolinite-dickite to replace bornite and chalcopyrite. Despite the lack of tennantite in most chalcopyrite ores, fluids may still have contained arsenic in solution at conditions unfavorable tennantite precipitation. Iron content in sphalerite decreases from chalcopyrite-rich ore to bornite rich ore and from core to rim in sphalerite from Zn-Pb ore bodies. These relationships indicate a decrease in  $R_H$  and  $R_S$  at a given location within an orebody as time progressed, and fluids which deposited iron oxide assemblages at the edge of an ore body may have precipitated bornite + pyrite + tennantite in the core. Zinc-lead ores formed distal to Cu ores where  $H_2S$  concentrations again became high, progressively farther from fluid sources as time progressed. Lode deposits at Bisbee are broadly similar to many other Cu lode districts worldwide, including Butte and Magma in the USA, Morococha and Cerro de Pasco, Peru, and Elshitsa, Bulgaria.

#### ACKNOWLEDGEMENTS

The authors wish to thank Douglas Graeme and Richard Graeme IV for their recollections of underground geology at Bisbee. Eric Seedorff and Frank K. Mazdab of the University of Arizona gave many helpful comments on the manuscript. Hexiong Yang and Robert Downs of the University of Arizona Mineral Museum provided access to ore samples from the museum's collection and helped with Raman spectroscopy and single-crystal X-ray diffraction of samples. Kenneth Domanik of the Lunar and Planetary Laboratory provided invaluable help for microprobe analyses.

## REFERENCES

- Afifi, A.M., Kelly, W.C., and Essene, E.J. (1988a) Phase Relations among Tellurides, Sulfides, and Oxides: I. Thermochemical Data and Calculated Equilibria. *Economic Geology*, 83, 377-394.
- Afifi, A.M., Kelly, W.C., and Essene, E.J. (1988b) Phase Relations among Tellurides, Sulfides, and Oxides: II. Applications to Telluride-Bearing Ore Deposits. *Economic Geology*, 83, 395-404.
- Bain, G.W. (1952) Age of the "Lower Cretaceous" from Bisbee, Arizona uraninite. *Economic Geology*, 47, 305-315.
- Barton, P.B. Jr., Bethke, P.M. (1987) Chalcopyrite disease in sphalerite: Pathology and epidemiology. *American Mineralogist*, 72:5, 451-467.
- Bartos, P.J. (1989) Prograde and retrograde base metal lode deposits and their relationship to underlying porphyry copper deposits. *Economic Geology*, 84, 1671-1683.
- Baumgartner, R., Fontboté, L., Vennemann, T. (2008) Mineral Zoning and Geochemistry of Epithermal Polymetallic Zn-Pb-Ag-Cu-Bi Mineralization at Cerro de Pasco, Peru. *Economic Geology*, 103, 493-537.
- Bendezú, R., Fontboté, L. (2009). Cordilleran Epithermal Cu-Zn-Pb-(Au-Ag) Mineralization in the Colquijirca District, Central Peru: Deposit Scale Mineralogical Patterns. *Economic Geology*, 104, 905-944.
- Bonillas, Y.S., Tenney, J.B., Feuchere, L. (1916) Geology of the Warren mining district. *A.I.M.E. Transactions*, 55, 285-355.
- Bowman, J.R. (1998) Basic Aspects and Applications of Phase Equilibria in the Analysis of Metasomatic Ca-Mg-Al-Fe-Si Skarns; in *Mineralized Intrusion-Related Skarn*

- Systems, edited by D.R. Lentz. Mineralogical Association of Canada Short Course 26, p. 1-49.
- Bryant, D.G. (1964) Intrusive Breccias and Associated Ore of the Warren (Bisbee) Mining District, Cochise County, Arizona. Unpublished PhD (Dissertation, Stanford, California, Stanford University). 149 pp.
- Bryant, D.G. (1968) Intrusive Breccias Associated with Ore, Warren (Bisbee) Mining District, Arizona. *Economic Geology*, 63, 1-12.
- Bryant, D.G., Metz, H.E. (1966) Geology and ore deposits of the Warren mining district; in *Geology of the porphyry copper deposits, Southwestern North America*, edited by S. Titley and C. Hicks. University of Arizona Press, Tucson, Arizona, 189-204.
- Catchpole, H., Kouzmanov, K., Fontboté, L. (2012) Copper-excess stannoidite and tennantite-tetrahedrite as proxies for hydrothermal fluid evolution in a zoned Cordilleran base metal district, Morococha, Central Peru. *Economic Geology*, 50, 719-743.
- Criddle, A.J., Stanley, C.J., Eady, C.S. (1982) Ore mineralization of the Campbell orebody, Bisbee, Arizona. Unpublished report, Freeport McMoRan files.
- Czamanske, G. (1974) The FeS Content of Sphalerite Along the Chalcopyrite-Pyrite-Bornite Sulfur Fugacity Buffer. *Economic Geology*, 69, 1328-1334.
- Einaudi, M.T. (1977) Environment of ore deposition at Cerro de Pasco, Peru. *Economic Geology*, 72, 893-924.
- Einaudi, M.T. (1982) Skarns associated with porphyry copper plutons, I. Description of deposits, southwestern U.S., II. General features and origin, *in* Titley, S.R., ed.,

- Advances in geology of the porphyry copper deposits, southwestern North America:* Tucson, University of Arizona Press, pp. 139-183.
- Einaudi, M.T., Hedenquist, J.W., Inan, E.E. (2003) Sulfidation state of fluids in active and extinct hydrothermal systems: transitions from porphyry to epithermal environments. Special Publication-Society of Economic Geologists, 10, 285-314.
- Fontboté, L., and Bendejú, R. (2009) Cordilleran or Butte-type veins and replacement bodies as a deposit class in porphyry systems, *in* Williams, P.J., ed., Proceedings of the 10<sup>th</sup> Biennial Society of Geology Applied to Ore Deposits Meeting, 2009, 521-523.
- Friehauf, K. (1997 May 31) Petrographic Comparison of Carbonate-hosted Hematite-bearing Massive Replacement Ores of the Bingham, Superior, and Bisbee Districts. Retrieved from <https://pangea.stanford.edu/research/ODEX/kurts-images/bingham/main-text.htm>.
- Friehauf, K. (1998) Geology and geochemistry of porphyry-related, carbonate hosted, massive replacement Cu-Au deposits: a case study of the Superior District, Arizona. Unpublished PhD (Doctoral dissertation, Stanford, California, Stanford University).
- Gilluly, J., Cooper, J.R., Williams, J.S. (1954). Late Paleozoic stratigraphy of central Cochise County, Arizona. *USGS Professional Paper* 266, 49 p.
- Graeme, R.W. (1981) Famous mineral localities: Bisbee, Arizona. *Mineralogical Record*, 12:5, 259-319.
- Grguric, B.A., Harrison, R.J., and Punis, A. (2000) A revised phase diagram for the bornite-digenite join from *in situ* neutron diffraction and DSC experiments. *Mineralogical Magazine*, 64:2, 213-231.

- Gustafson, L.B. (1961) Paragenesis and hypogene zoning at the Magma mine, Superior, Arizona. Unpublished Ph.D. (Doctoral dissertation, Cambridge, Massachusetts, Harvard University).
- Hammer, D.F., Peterson, D.W. (1968) Geology of the Magma Mine area, *in* Ridge, J.D., ed., *Ore deposits of the United States, 1933-1967 (Graton-Sales Volume)*: American Institute of Mining, Metallurgical, Petroleum Engineers, v. 2, pp. 1282-1310.
- Hewett, D.F., and Rove, O.N. (1930) Occurrence and relations of alabandite. *Economic Geology*, 25, 36-56.
- Hogue, W.G., and Wilson, E.D. (1950) Bisbee or Warren District. *Arizona Bureau of Mines Bulletin*, 156, pp. 17-29.
- James, L.P. (1976) Zoned alteration in limestone at porphyry copper deposits, Ely, Nevada. *Economic Geology* 72, 488-512.
- Kojima, S., and Sugaki, A. (1985) Phase Relations in the Cu-Fe-Zn-S System between 500° and 300°C under Hydrothermal Conditions. *Economic Geology*, 80, 158-171.
- Kouzmanov, K., Bogdanov, K., Ramboz, C. (2005) Te- and Bi-bearing assemblages in the Elshitsa and Radka epithermal deposits, Central Srednogorie, Bulgaria: Mineralogy and genetic features. *Geochemistry, Mineralogy, and Petrology*, 43, 108-112.
- Kouzmanov, K., Moritz, R., von Quadt, A., Chiardia, M., Peytcheva, I., Fontinge, D., Ramboz, C., Bogdanov, K. (2009) Late Cretaceous porphyry Cu and epithermal Cu-Au association in the Southern Panagyurishte District, Bulgaria: the paired Vlaykov Vruh and Elshitsa deposits. *Mineralum Deposita*, 44, 611-646.

- Kudoh, Y., and Takéuchi, Y. (1976) The superstructure of stannoidite. *Zeitschrift für Kristallographie*, 144, 145-160.
- Lang J., Thompson J., Mortensen J., Baker T., Coulson I., Duncan R., Maloof T., James J., Friedman R., Leprite M. (2001) The Arizona porphyry province, *in* Lang, J., ed., *Regional and System-Scale Controls on the Formation of Copper and/or Gold Magmatic-Hydrothermal Mineralization*, p. 53-76. The Mineral Deposit Research Unit, The University of British Columbia, British Columbia.
- Lewis, M. (1996) Characteristics of hypogene covellite assemblages at the Chuquicamata porphyry copper deposit, Chile, Section 4500N. Unpublished MS (Masters thesis, Halifax, Nova Scotia, Dalhousie University).
- López, V.M. (1939) The primary mineralization at Chuquicamata, Chile, S.A. *Economic Geology*, 34, 674-711.
- Manske, S., and Skinner, B.J. (1971) Studies of the Sulfosalts of Copper I. Phases and Phase Relations in the System Cu-As-S. *Economic Geology*, 66, 901-918.
- Manske, S.L., and Paul, A.H. (2002). Geology of a Major New Porphyry Copper Center in the Superior (Pioneer) District, Arizona. *Economic Geology*, 97, pp. 197-220.
- Meijer, A. (2014) The Pinal Schist of southern Arizona: A Paleoproterozoic forearc complex with evidence of spreading ridge-trench interaction at ca. 1.65 Ga and a Proterozoic arc obduction event. *GSA Bulletin*, 126:9-10, pp. 1145-1163.
- Meyer, C., Shea, E.P., Goddard, C.C. Jr., and staff (1968) Ore deposits at Butte, Montana, *in* Ridge, J.D., ed., *Ore deposits of the United States, 1933-1967 (Graton-Sales Volume)*: American Institute of Mining, Metallurgical, Petroleum Engineers, v. 2, pp. 1373-1416.

- Nye, T.S. (1968) The relationship of structure and alteration to some orebodies in the Bisbee (Warren) District, Cochise County, Arizona: Unpublished PhD thesis, University of Arizona, 212 pp.
- O'Leary, M.J., and R.O. Sack (1987) Fe-Zn exchange reaction between tetrahedrite and sphalerite in natural environments. *Contributions in Mineralogy and Petrology*, 96, 415-425.
- Ossandón, G.C., Fréaut, R.C., Gustafson, L.B., Lindsay, D.D., Zentilli, M. (2001) Geology of the Chuquicamata Mine: A Progress Report. *Economic Geology*, 96, 249-270.
- Peng, C. (1948) The Mountain Maid ore body, Bisbee, Arizona: Unpublished master's thesis, University of Arizona, 36 pp.
- Ransome, F.L. (1904) The geology and ore deposits of the Bisbee Quadrangle, Arizona. *US Geological Survey Professional Paper 21*, 168 pp.
- Ray, J.C. (1914) Paragenesis of the ore minerals in the Butte District, Montana. *Economic Geology*, 9, 463-482.
- Reed, M., Rusk, B., Palandri, J. (2013) The Butte Magmatic-Hydrothermal System: One Fluid Yields All Alteration and Veins. *Economic Geology*, 108, 1379-1396.
- Riggs, N.A., and Busby-Spera, C.J. (1990) Evolution of a multi-vent volcanic complex with in a subsiding arc graben depression: Mount Wrightson Formation, Arizona. *GSA Bulletin*, 102, 1114-1135.
- Rusk, B.G., Miller, B.J., Reed, M.H. (2008) Fluid-inclusion evidence for the formation of Main Stage polymetallic base-metal veins, Butte, Montana, USA, in Spencer, J.E. and

- Titley, S.R. (eds.) *Ores and Orogenesis: Circum-Pacific Tectonics, Evolution, and Ore Deposits*. Arizona Geological Society Digest 22, 573-582.
- Sack, R.O., Ebel, D.S., O'Leary, M.J. (1987) Tennahedrite thermochemistry and metal zoning, *in* Helgeson, H.C. (ed.), *Chemical transport in metasomatic processes*. Springer Netherlands, 701-731.
- Sales, R.H., Meyer, C. (1949) Results from preliminary studies of vein formation at Butte, Montana. *Economic Geology*, 44, pp. 465-484.
- Schwartz, G.M., Park, C.F., Jr. (1932) A microscopic study of ores from the Campbell mine, Bisbee, Arizona. *Economic Geology*, 26, 39-51.
- Scott, S.D., and Barnes, H.L. (1971) Sphalerite geothermometry and geobarometry. *Economic Geology*, 66, 653-669.
- Tenney, J.B. (1913) Unpublished report on 2,200 hand specimen and thin section determinations. Freeport McMoRan files.
- Trischka, C. (1938) Bisbee district. *Arizona Bureau of Mines Bulletin*, 145, 32-41.
- Trudu, A.G., and Knittel, U. (1998) Crystallography, mineral chemistry and chemical nomenclature of goldfieldite, the tellurian member of the tetrahedrite solid-solution series. *Canadian Mineralogist* 36, 1115-1137.

## FIGURE CAPTIONS

Figure 1. Location map.

Figure 2. Geologic map of the Bisbee district, modified from Graeme (1981).

Figure 3. Paragenesis of mineral assemblages at Bisbee.

Figure 4. Time-space diagram showing the interpreted evolution of magmatic-hydrothermal system responsible for formation of Cu lodes at Bisbee. Vertical arrows represent fluid flow paths through space within an ore body at a given point in time. An infinite number of fluid paths are possible; arrows on the diagram are for the sake of discussion.

Figure 5. Compositions of tennantite group minerals by ore type, classified according to semimetal (X-site) cations. Species are named on a basis of two or more atoms As, Sb, or Te per formula unit, demarcated by 50% lines on the ternary plot.

Figure 6. Variations in composition of tennantite group minerals by ore type, classified according to variations in M1 and M2 cations. (a) Excess Cu ( $\text{Cu}^*$ ) over 10 apfu ( $\text{Cu} + \text{Ag}$ ) in tennantite group minerals versus Zn in M2 site. Note that nearly all Cu-excess tennantite occurs as a replacement of enargite. (b) Fe versus Zn concentration by ore zone. High Fe content, with the exception of one sample from a Zn-Pb stope, is restricted to enargite-rich ore and corresponds to higher  $\text{Cu}^*$ . (c) Ag versus Sb in tennantite group minerals. Silver content follows Sb: tetrahedrites from Bisbee are high in Ag, whereas tennantites have very low Ag contents.

Figure 7. Typical chalcopyrite-rich ore: (a) Quartz hosts disseminated magnetite (mt), specular hematite (hm) and pyrite (py), representative of the Fe-oxide shell around ore bodies. This sample exhibits early-stage chalcopyrite deposition (ccp),

1.0 mm wide field (Campbell shaft). (b) Chalcopyrite and pyrite (“exploded bomb” texture), with equant grains of hematite showing relict cores of brownish magnetite (hem-mag), 2.0 mm wide field (Sacramento shaft). Note how fractures filled with chalcopyrite do not exhibit even edges; they always appear scalloped, concave to pyrite. (c) Chalcopyrite containing “sphalerite stars” (sp) associated with specular hematite, 1.0 mm wide field (Gardner shaft). (d) Small irregular grains of chalcopyrite and euhedral pyrite in a mixture of cupropavonite and krupkaite (cpv-kru, unresolved), 0.75 mm wide field (Campbell shaft). Pyrite from this association is always euhedral and contains inclusions of chalcopyrite and cupropavonite-krupkaite, indicating equilibrium deposition. (e) Chalcopyrite associated with kiddcreekite (kid), colusite (col), tennantite (tn), and native tellurium (Te) in pyrite. This is typical of telluride-rich pyritic ores from below the 2100 level of the Campbell shaft. Field is 1 mm wide. (f) Magnetite almost completely pseudomorphed to hematite, associated with chalcopyrite, pyrite, and quartz. Note the ends of some bladed, non-pseudomorphic hematite within pyrite and chalcopyrite display caries texture concave to pyrite, indicating replacement. Field is 0.75 mm wide (Campbell Shaft).

Figure 8. Representative images of ore from Zn-Pb ore bodies. (a) Sphalerite (sp) and galena (gn) with quartz (qtz) and pyrite (py), field is 2 mm wide. Sphalerite and galena are concave to pyrite and quartz, indicating replacement. Fine inclusions of quartz and chalcopyrite are in both sphalerite and pyrite (Higgins mine, Tunnel Level). (b) Galena and sphalerite throughout silica-pyrite and showing replacement by quartz, field is 2 mm wide (Campbell shaft). (c) Argentinian, Zn-

rich tetrahedrite (tt) associated with sphalerite, galena, minor pyrite and quartz, field is 1 mm wide (Campbell shaft). (d) Sphalerite with chalcopyrite disease, associated with pyrite, siderite (sd), and chalcopyrite (ccp), field is 2 mm wide. Sphalerite is zoned from high FeS against chalcopyrite-pyrite (fine chalcopyrite disease) to low FeS and coarse chalcopyrite disease (Campbell shaft). Figure 9.

Representative images of bornite-rich ore. Bornite is always associated with either chalcopyrite or chalcocite. (a) Chalcopyrite (ccp) concave to bornite (bn) with euhedral pyrite (py), sphalerite (sp), Zn-rich tennantite (tn), field is 2 mm wide (Campbell shaft). This caries texture of bornite against chalcopyrite with euhedral pyrite is indicative of chalcopyrite being replaced by bornite + pyrite. (b) Bornite showing caries texture against chalcopyrite with Zn,Te-rich tennantite, muscovite (msc) and barite (brt), field is 2 mm wide (Holbrook extension, Lavender pit). (c) Relict hematite laths (hem) in pyrite, with bornite and sphalerite, field is 0.25 mm wide (unknown mine). This is an overprint of chalcopyrite, hematite, pyrite association; compare figure 7b above. (d) Bornite exhibiting caries texture against chalcopyrite, and sphalerite. Sphalerite exhibits caries texture against bornite. Sphalerite contains inclusions of stannoidite (stn); field is 1 mm wide (mine unknown). (e) Bornite with chalcocite containing exsolutions of native gold (Au) and myrmekitic stromeyerite (str) and wittichenite (wt), field is 1 mm wide (1600 level, Campbell Shaft). (f) Subhedral, sieve textured pyrite in bornite with minor chalcocite. Note “grating texture” of bornite exsolutions from chalcocite. Pyrite grains contain small chalcopyrite (labeled) and bornite inclusions. Field is 1 mm wide (Junction Shaft). (g) Bornite and chalcocite containing inclusions of galena

(gn), mawsonite (mw), and dolomite (dol). Field is 0.5 mm wide (Junction shaft).

(h) Bornite veined by chalcocite, containing anhedral stannoidite grains, one of which has a core of colusite (col). Field is 1 mm wide (Junction shaft).

Figure 10. Representative images of chalcocite-rich ore. (a) Relict pyrite (py), bornite (bn), and chalcopyrite (ccp) with enargite-tennantite (en-tn), field is 2 mm wide. Chalcopyrite is convex to, and veined by, bornite, indicating replacement, while bornite is convex to enargite. The enargite underwent retrograde alteration to argentian, Fe-rich tennantite (Junction shaft). (b) Close-up of Ag,Fe-rich tennantite replacing enargite in the previous image, field is 0.5 mm wide. (c) Digenite (dg) with minor bornite concave to digenite, indicating replacement. Field is 0.5 mm wide (1300 level Cole shaft, 39-A stope). (d) Intergrowth of subhedral enargite with digenite-chalcocite-bornite exsolution (dg-cc) in the same sample as (c), establishing chalcocite as being later than enargite, field is 0.25 mm wide. This assemblage contains digenite-chalcocite and kaolinite, whereas bornite-dominated ore contains muscovite. (e) Enargite containing fracture-filling Fe-rich tennantite, field is 0.25 mm wide (Junction shaft). (f) Chalcostibite (ch) concave to luzonite (luz) containing irregular enargite, which is also concave to luzonite. The sequence of deposition is chalcostibite-enargite-luzonite. Field is 1 mm wide (Junction Shaft). (g) Spectacular example of botryoidal covellite, field is 2 mm wide. The pitted band between covellite layers contained kaolinite-dickite (now mostly plucked) and quartz (Campbell Shaft). (h) Covellite (cv) enclosing an intergrowth of low-FeS sphalerite (sp) and galena (gn), field is 2 mm wide (Cole shaft).

Figure 11. Isobaric phase diagrams (500 bars) at 450°C (a) and 325°C (b) in terms of redox state ( $R_H$ ) and sulfidation state ( $R_S$ ), where  $R_H \approx (XH_2/XH_2O)$  and  $R_S \approx \log (XH_2/XH_2S)$ . The variables  $R_H$  and  $R_S$  were chosen because they represent actual reaction due to disproportionation of magmatic  $SO_2$  (Einaudi et al., 2003), and best explain the observed mineralogy and paragenesis seen at Bisbee. Diagram (a) shows stability fields of  $H_2S$  and  $SO_2$ , iron sulfides and oxides, Cu-Fe sulfides, as well as mole fraction FeS in sphalerite at 450°C. The yellow circle represents a  $10^{-1}$  molal total sulfur concentration. Diagram (b) shows stability fields of  $H_2S$  and  $HSO_4^-$ , iron sulfides and oxides, Cu-Fe sulfides, and mole fraction FeS in sphalerite as well as stability fields for the tennantite + sulfur = enargite and tetrahedrite + sulfur = famatinite buffers at 325°C. See text for descriptions of reaction paths.

FIGURES

Figure 1

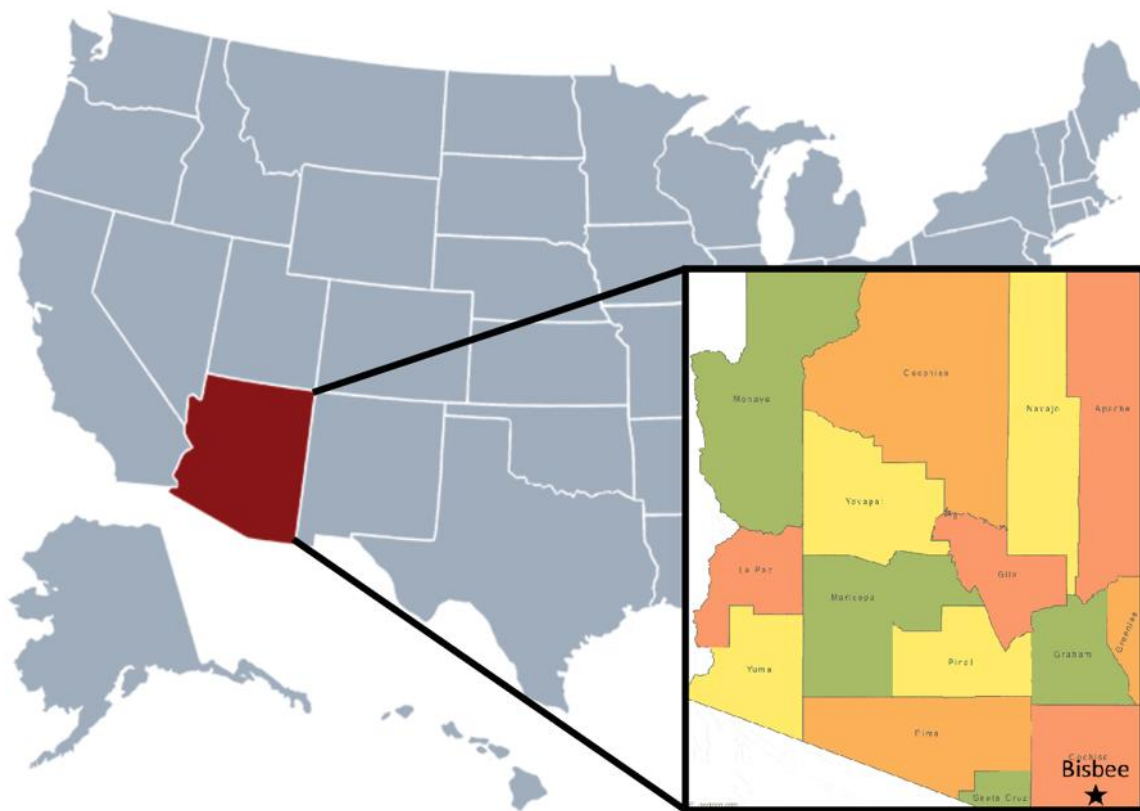


Figure 2

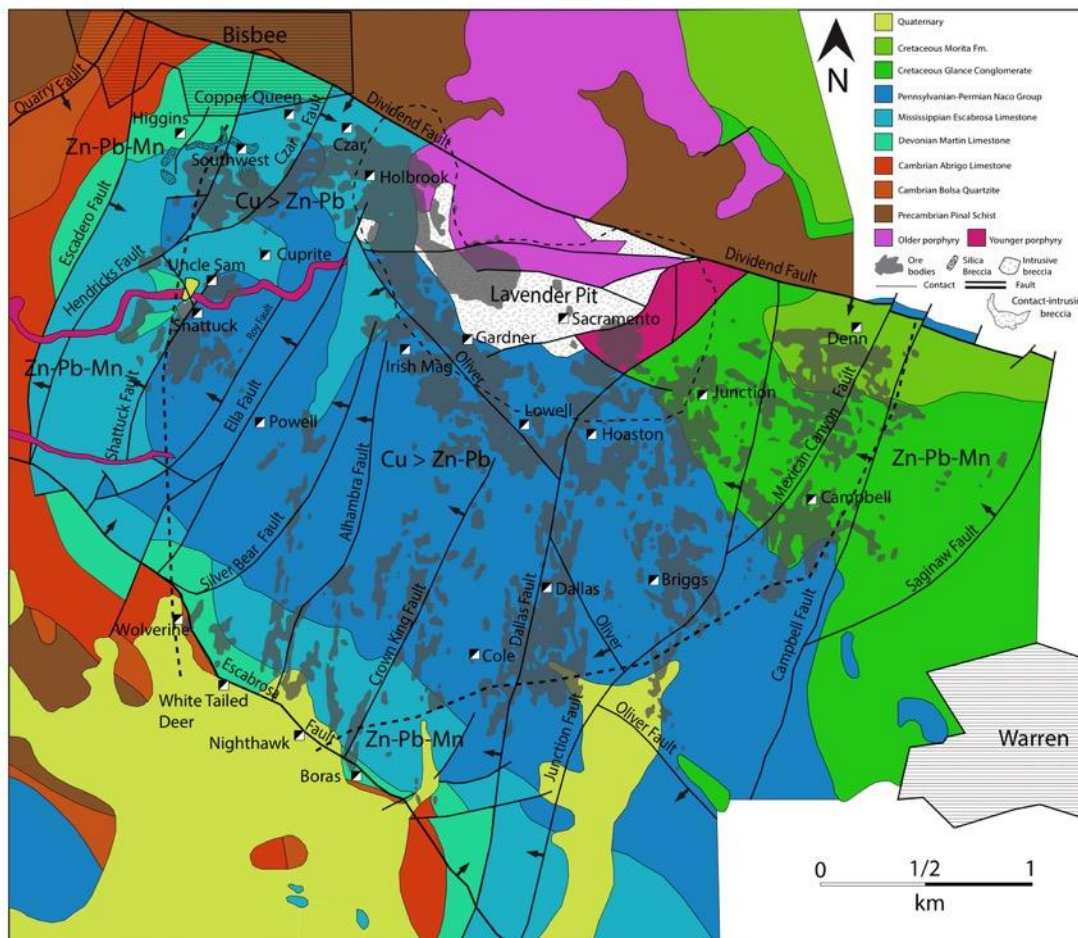


Figure 3

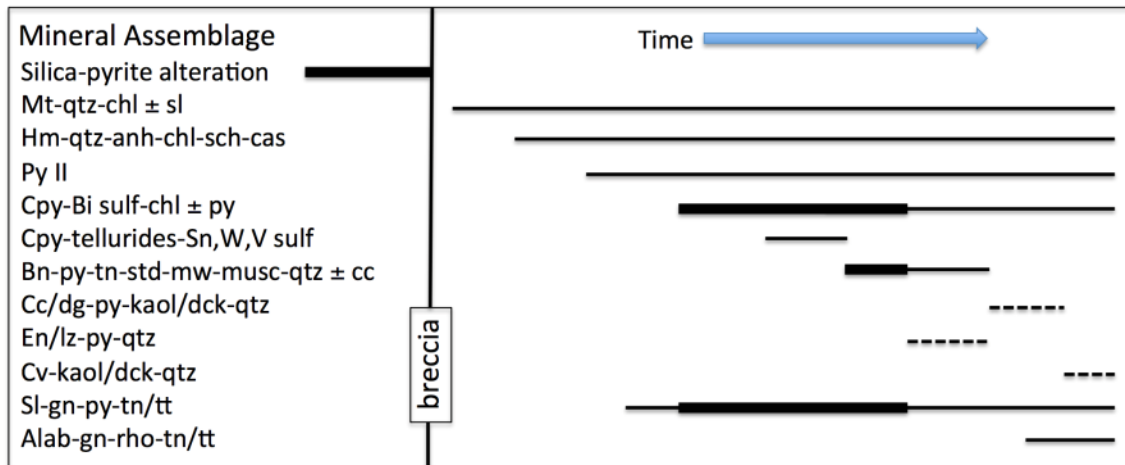


Figure 4

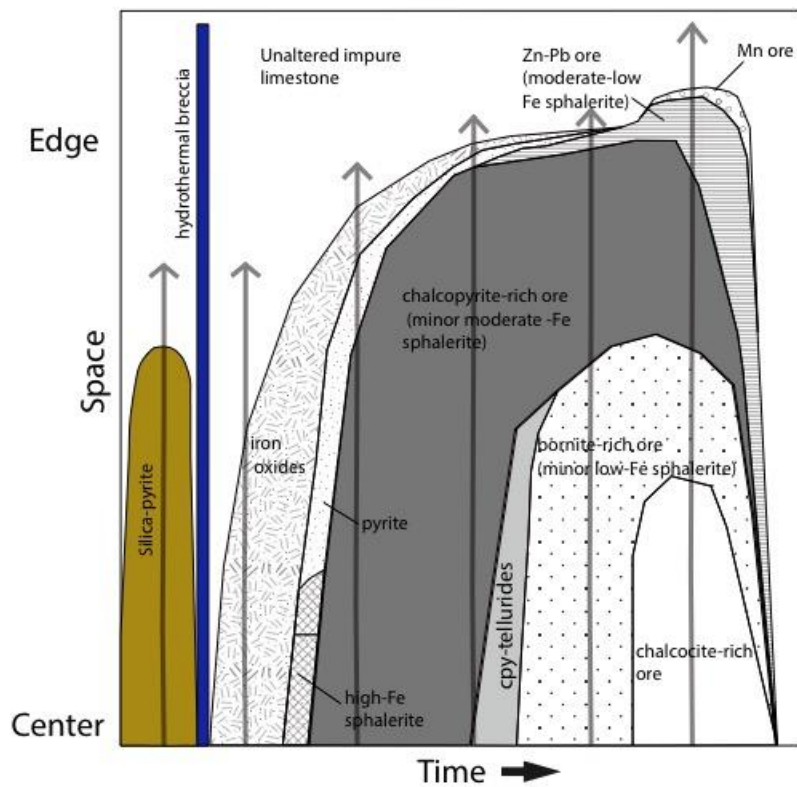


Figure 5

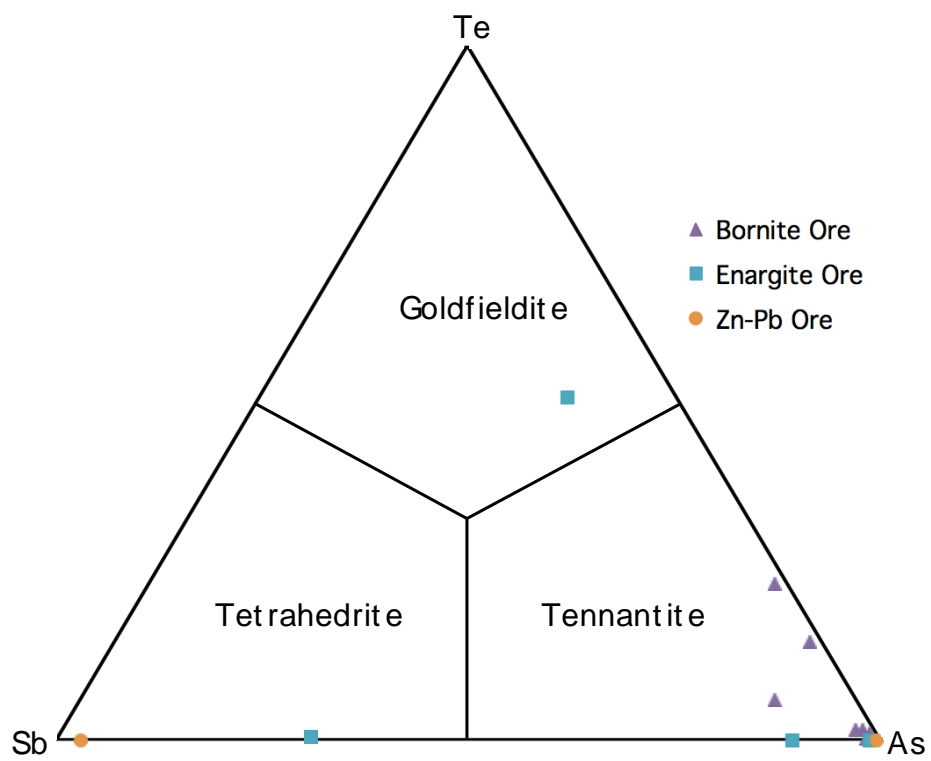


Figure 6

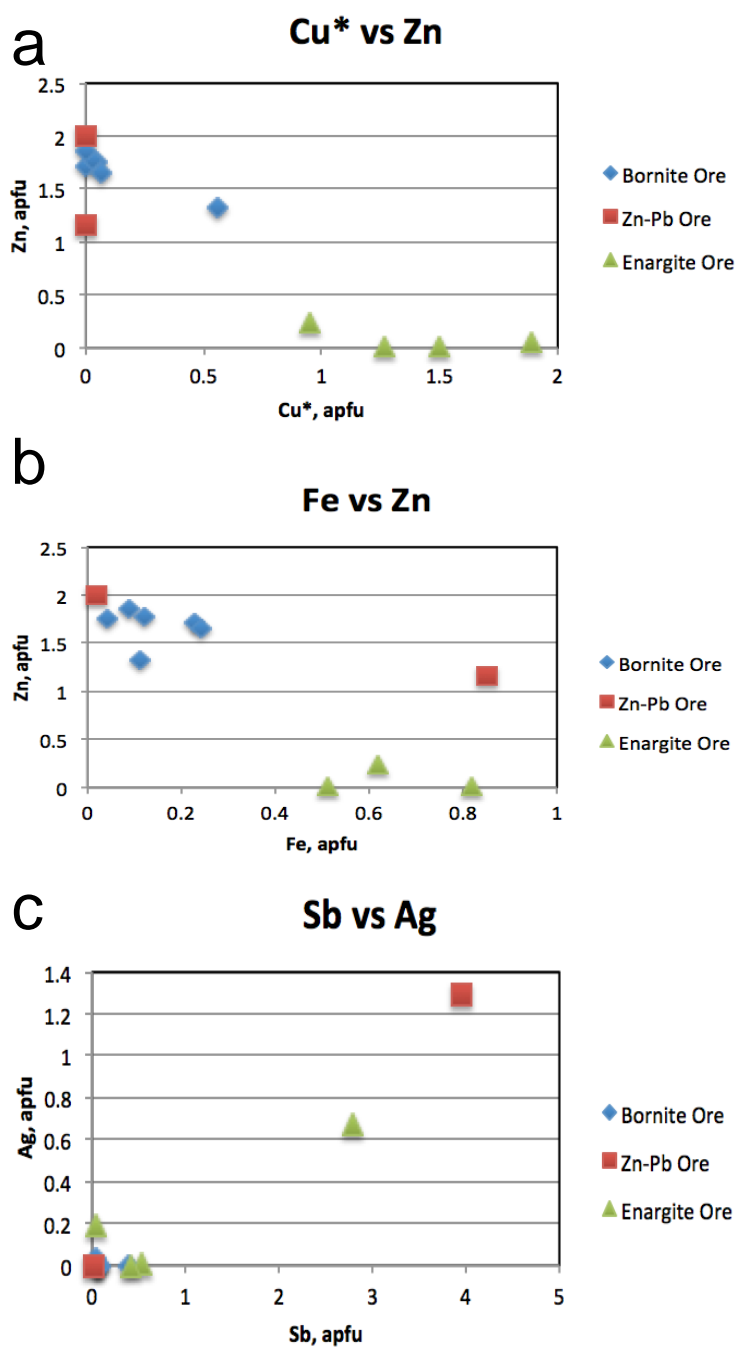


Figure 7

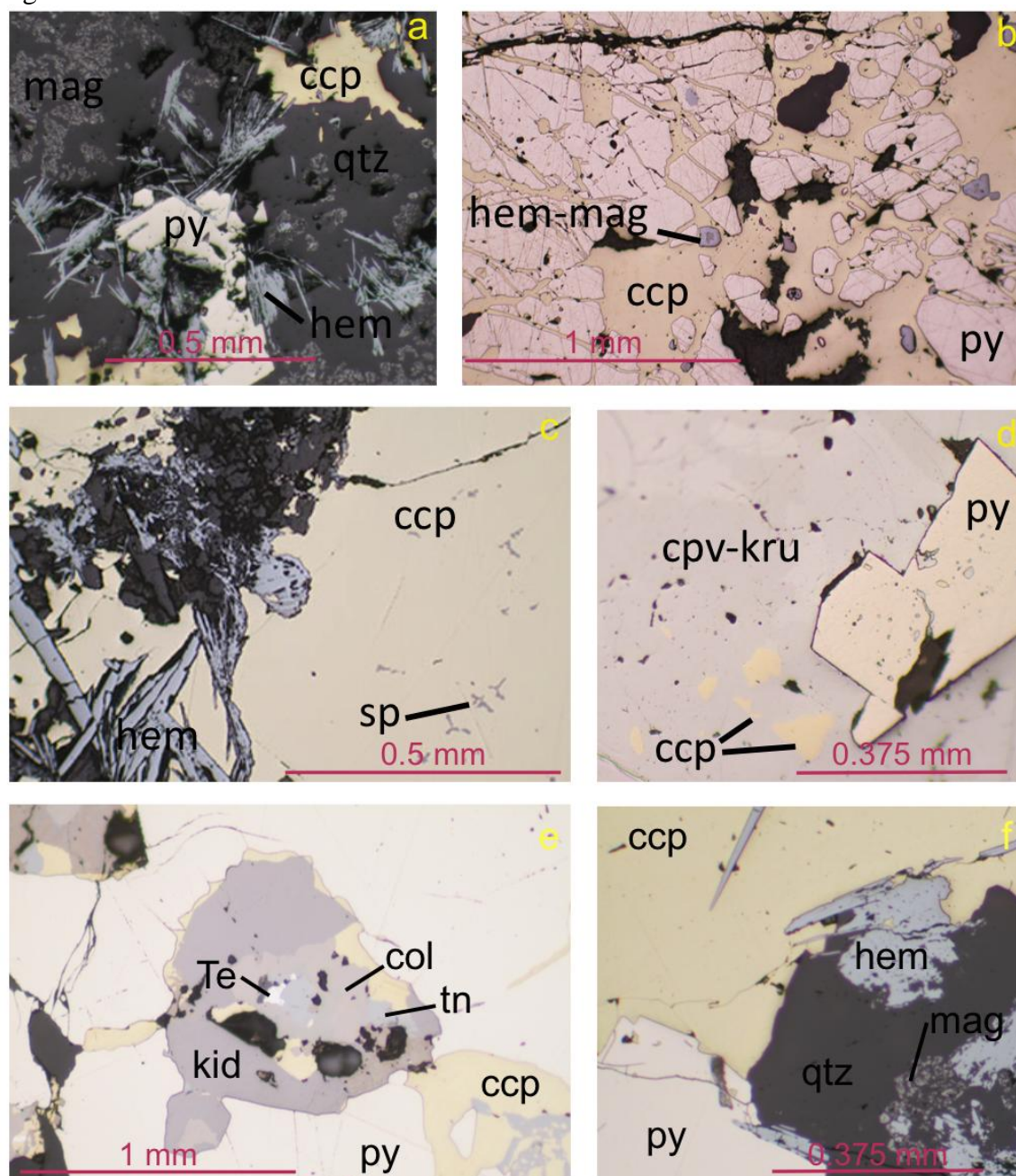


Figure 8

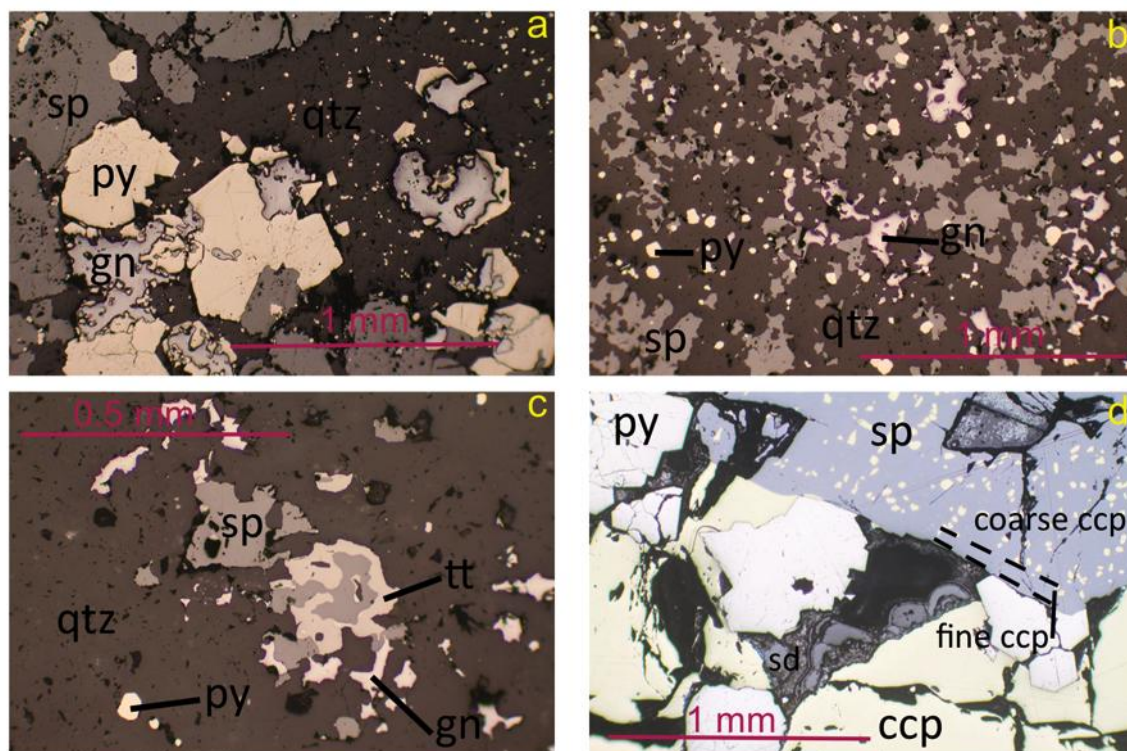


Figure 9

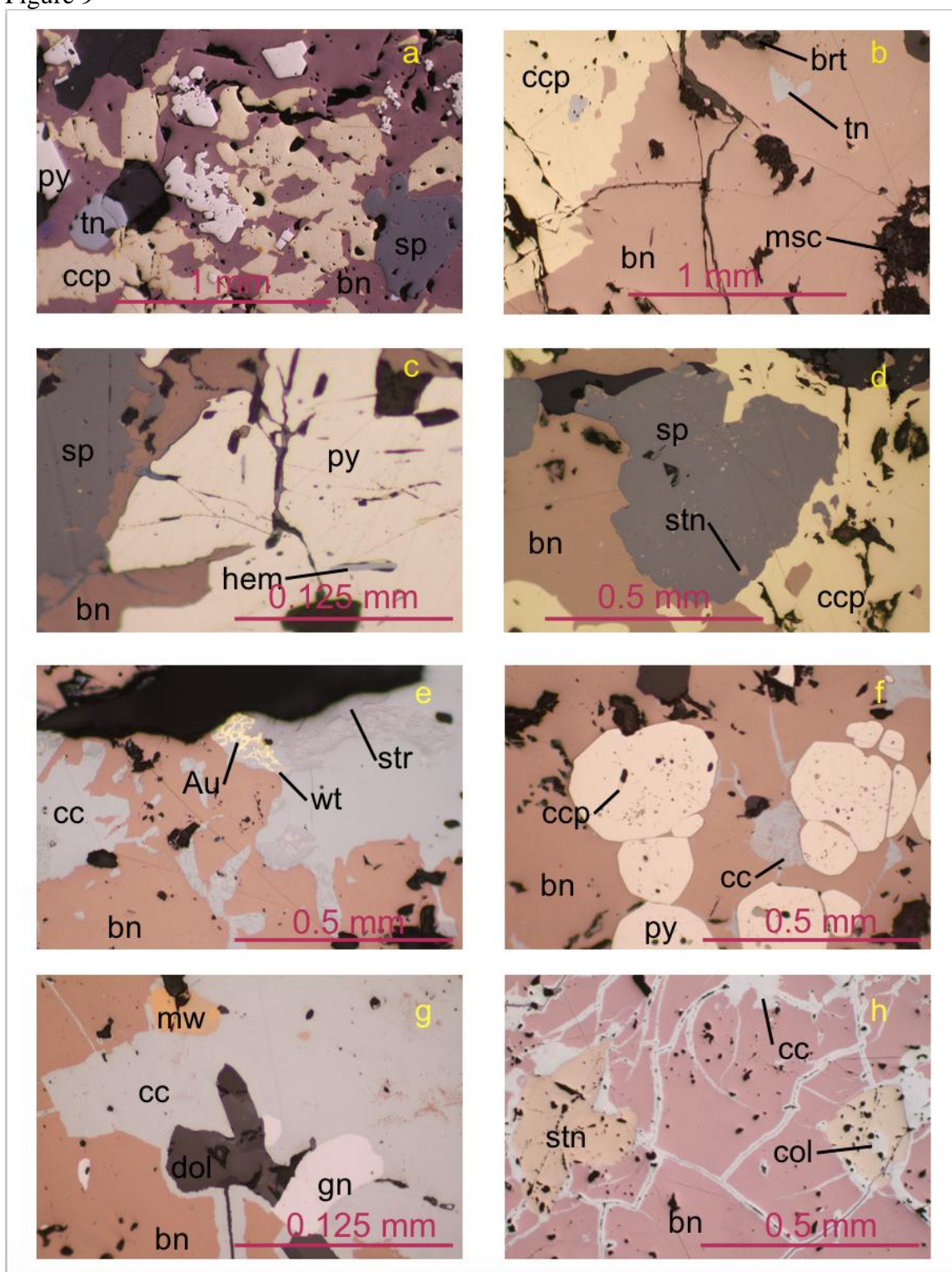


Figure 10

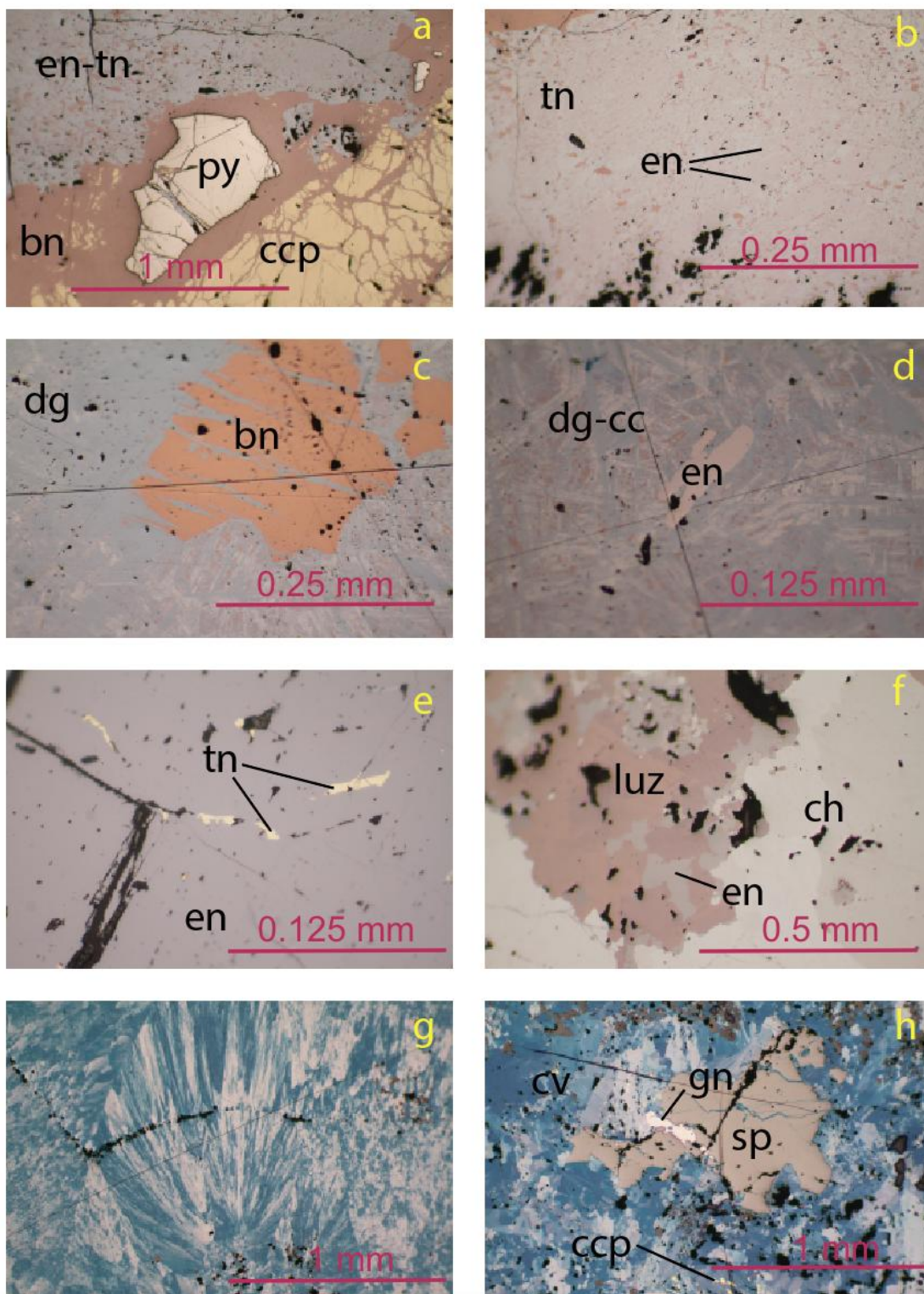
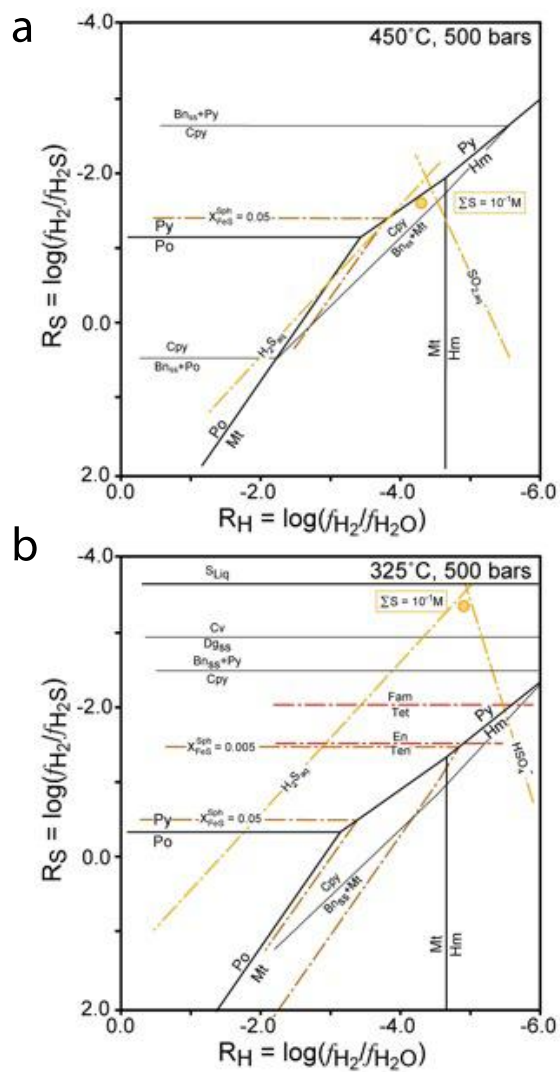


Figure 11



## TABLE EXPLANATORY NOTES

Table 1. Compositions of sphalerite in the three ore types at Bisbee. Note that zoning only occurs in sphalerite from Zn-Pb ore.

Table 2. Compositions of stannoidite. The ideal chemical formula of stannoidite is  $\text{Cu}_8(\text{Fe},\text{Zn})_3\text{Sn}_2\text{S}_{12}$ , however  $\text{Fe}^{2+}$  and Zn occupy a site distinct from  $\text{Fe}^{3+}$  (Kudoh and Takeuchi, 1976), therefore a crystal-chemical formula may be written  $\text{Cu}_8\text{Fe}^{3+}_2(\text{Fe}^{2+},\text{Zn})\text{Sn}_2\text{S}_{12}$ .

Table 3. Compositions of tennantite-tetrahedrite from bornite- and chalcocite-rich ore types. Note that tennantite-tetrahedrite from the chalcocite-rich ore contains  $\text{Zn} < \text{Fe}$  and more copper than tennantite-tetrahedrite from bornite-rich ore.  
Abbreviation: nd = not detected.

Table 4. Compositions of selected accessory minerals from various ore types at Bisbee.  
Abbreviations: nd = not detected, na = not analyzed.

Table 5. Ore minerals identified in Bisbee Cu-Zn-Pb lodes.

Table 6. Gangue minerals identified in Bisbee Cu-Zn-Pb lodes.

Table 7. Comparison of Bisbee with selected worldwide districts containing base metal lodes.

Table 1

Ore Type	Chalcopyrite	Chalcopyrite	Chalcopyrite	Bornite	Bornite	Zn-Pb	Zn-Pb	Zn-Pb	Zn-Pb
Sample	R1329	R1329	R1224	5518	R1204	R1235	R1959 rim	R1959 core	R1197
Element									
Zn	60.46	62.88	64.95	64.94	66.72	66.04	64.96	64.00	66.33
Fe	5.31	2.40	1.20	0.27	0.02	0.13	0.28	1.25	0.30
Cu	0.08	1.69	0.65	0.96	0.07	0.06	0.14	0.20	0.08
Mn	nd	nd	nd	nd	0.05	0.30	1.49	1.49	0.08
S	33.85	33.43	33.80	33.45	33.25	33.15	33.59	33.65	33.19
Total	99.70	100.40	100.60	99.62	100.11	99.68	100.46	100.59	99.98
Atoms*									
Zn	0.92	0.97	0.97	0.98	0.99	0.99	0.96	0.95	0.99
Fe	0.07	0.02	0.01	0.00	0.00	0.00	0.00	0.02	0.00
Cu	0.00	0.00	0	0.00	0.00	0.00	0.00	0.00	0.00
Mn	-	-	-	-	0.00	0.01	0.03	0.03	0.00
S	1.00	1.00	1.03	1.01	1.02	1.01	1.01	1.03	1.03
X <sub>FeS</sub>	0.075	0.017	0.011	0.000	0.0004	0.0012	0.003	0.019	0.004
Mol % Fe	7.5	1.7	1.1	0.0	0.0	0.1	0.3	1.9	0.4

\*Note: corrected for interference from chalcopyrite disease by subtracting a 1:1:2 molar ratio of Cu:Fe:S

Table 2

Sample	3169	5518	R1204	R1893	R2336
Element					
Cu	38.76	39.88	39.33	39.08	40.09
Fe	8.47	8.75	8.48	8.66	8.88
Zn	4.42	4.30	5.58	5.39	4.25
Sn	17.57	17.34	18.01	17.27	17.43
S	29.25	29.70	29.08	29.76	29.55
As	0.38	na	na	na	na
Total	98.85	99.97	100.48	100.16	100.20
Cu	8.05	8.16	8.08	7.98	8.22
Fe	2.00	2.04	1.98	2.01	2.01
Zn	0.89	0.85	1.12	1.06	0.85
Sn	1.95	1.90	1.98	1.89	1.91
As	0.07	-	-	-	-
S	12.04	12.05	11.84	12.05	12.01
$\Sigma_{\text{Cat}}$	12.96	12.95	13.16	12.94	12.99

Table 3

Ore Type	Bornite	Bornite	Bornite	Bornite	Bornite	Zn-Pb	Zn-Pb	Chalcocite	Chalcocite	Chalcocite
Sample	3919	5518	R2336 rim	R2336 core	6SW	R1235	R1959	R1152	R1166	R1164
Element										
Cu	42.80	43.11	44.61	44.32	43.02	31.72	42.68	47.73	42.30	46.88
Fe	0.87	0.46	0.40	0.21	0.90	0.08	3.23	3.11	1.75	2.33
Zn	7.55	7.88	5.79	6.79	7.26	7.66	5.21	0.04	0.05	1.01
As	19.10	18.81	16.39	17.68	16.39	0.52	20.60	18.97	5.71	17.97
Sb	0.26	0.68	0.49	0.27	3.09	28.08	0.15	0.39	20.79	3.47
Te	0.32	0.54	4.65	2.93	1.93	nd	nd	0.01	0.13	nd
Bi	nd	0.14	0.15	0.15	nd	nd	nd	0.10	0.13	nd
Pb	nd	nd	nd	nd	nd	nd	nd	nd	nd	nd
Ag	nd	0.03	nd	nd	nd	8.09	0.06	1.40	4.41	nd
Se	nd	nd	nd	nd	nd	nd	nd	nd	nd	nd
S	28.69	28.62	27.89	27.94	28.43	24.26	28.32	28.52	25.47	28.57
Total	99.58	100.25	100.37	100.29	101.02	100.41	100.25	100.27	100.74	100.23
Cu	9.97	10.03	10.56	10.44	10.07	8.58	9.89	11.08	10.83	10.95
Fe	0.23	0.12	0.11	0.06	0.24	0.02	0.85	0.82	0.51	0.62
Zn	1.71	1.78	1.33	1.55	1.65	2.01	1.17	0.01	0.01	0.23
As	3.77	3.71	3.29	3.53	3.25	0.12	4.05	3.73	1.24	3.56
Sb	0.03	0.08	0.06	0.03	0.38	3.96	0.02	0.05	2.78	0.42
Te	0.04	0.06	0.55	0.34	0.22	0	0	0	0.02	0
Bi	0	0.01	0.01	0.01	0	0	0	0.01	0.01	0
Pb	0	0	0	0	0	0	0	0	0	0
Ag	0	0	0	0	0	1.29	0	0.19	0.67	0
Se	0	0	0	0	0	0	0	0	0	0
S	13.24	13.2	13.09	13.04	13.19	13.01	13.01	13.11	12.93	13.22
$\Sigma_{\text{Cat}}$	15.75	15.79	15.91	15.96	15.81	15.98	15.98	15.89	16.07	15.78
Temp, C*		325				302				

\*Note: Temperature data estimated using the tennantite-sphalerite Fe-Zn exchange method of Sack et al. (1987) and O'Leary and Sack (1987)

Table 4

Mineral Sample	Chalcostibite R1166	Luzonite R1166	Cupropavonite R1147	Krupkaite R1147	Tetradymite R1224*	Goldfieldite R1164	Mawsonite R2336	Wittichenite R1577
Element								
Cu	25.5	46.22	4.45	5.76	2.64	47.32	44.38	33.17
Fe	nd	nd	0.01	0.02	2.02	0.04	13.09	0.59
Zn	nd	nd	nd	nd	0.35	0.21	0.02	0.04
Sn	nd	nd	nd	nd	nd	nd	13.62	nd
As	0.44	9.66	nd	nd	nd	6.93	na	nd
Sb	46.56	14.27	0.01	0.06	0.29	3.98	na	0.03
Te	nd	0.01	0.24	nd	34.31	15.53	na	0.02
Bi	3.09	nd	60.22	57.8	57.14	0.51	na	45.83
Pb	nd	nd	8.93	20.63	nd	nd	na	0.31
Ag	nd	0.04	10.06	nd	0.08	0.04	na	0.59
Se	nd	0.01	0.06	0.01	1.18	nd	na	0.03
S	25.29	30.96	17.86	17.73	4.47	26.28	29.73	18.97
Total	100.87	101.17	101.83	102.07	102.66	100.84	100.86	99.51
Cu	1.02	3.01	0.63	0.98	0	11.88	6.03	2.70
Fe	0	0	0	0	0	0.01	2.02	0.05
Zn	0	0	0	0	0	0.05	0	0
Sn	0	0	0	0	0	0	0.99	0
As	0.01	0.53	0	0	0	1.47	0	0
Sb	0.97	0.49	0	0	0.02	0.52	0	0
Te	0.00	0	0.02	0	1.95	1.94	0	0
Bi	0.04	0	2.59	3.00	1.92	0.04	0	1.14
Pb	0	0	0.39	1.08	0	0	0	0.01
Ag	0	0	0.84	0	0.01	0.01	0	0.03
Se	0	0	0.01	0	0.10	0	0	0
S	2.00	4.00	5.00	6.00	0.96	13.07	8.00	3.07
Ore Type	Chalcocite	Chalcocite	Chalcopyrite	Chalcopyrite	Chalcopyrite	Chalcocite	Bornite	Chalcopyrite

Table 5

Mineral (abbreviation)	Formula	Ore Minerals	
		Ore Type	Abundance
Chalcopyrite (ccp)	CuFeS <sub>2</sub>	Chalcopyrite	Very abundant
Bornite (bn)	Cu <sub>5</sub> FeS <sub>4</sub>	Bornite	Abundant
Pyrite (py)	FeS <sub>2</sub>	All	Very abundant
Sphalerite (sp)	ZnS	Zn-Pb, chalcopyrite, bornite	Abundant
Galena (gn)	PbS	Zn-Pb, bornite	Abundant
Chalcocite (cc)	Cu <sub>2</sub> S	Bornite, chalcocite	Common
Digenite (dg)	Cu <sub>1.8</sub> S	Bornite, chalcocite	Common
Covellite (cv)	CuS	Chalcocite	Common
Tennantite (tn)	Cu <sub>12</sub> As <sub>4</sub> S <sub>13</sub>	Bornite, chalcocite	Common
Enargite (en)	Cu <sub>3</sub> AsS <sub>4</sub>	Chalcocite	Rare
Tetrahedrite (tt)	Cu <sub>12</sub> Sb <sub>4</sub> S <sub>13</sub>	Chalcocite, Zn-Pb	Rare
Alabandite (ala)	MnS	Zn-Pb	Common
Stannoidite (stn)	Cu <sub>8</sub> Fe <sub>2</sub> ZnSn <sub>2</sub> S <sub>12</sub>	Bornite	Common
Mawsonite (mw)	Cu <sub>6</sub> Fe <sub>2</sub> SnS <sub>8</sub>	Bornite	Common
Wittichenite (wt)	Cu <sub>3</sub> BiS <sub>3</sub>	Chalcopyrite, bornite	Common
Uraninite (UO <sub>2</sub> )	UO <sub>2</sub>	Chalcopyrite	Common
Colusite (col)	Cu <sub>12</sub> VAs <sub>3</sub> S <sub>16</sub>	Chalcopyrite, bornite	Common
Krupkaite (kru)	PbCuBi <sub>3</sub> S <sub>6</sub>	Chalcopyrite	Common
Goldfieldite (gfd)	Cu <sub>10</sub> Te <sub>4</sub> S <sub>13</sub>	Chalcocite	Rare
Cupropavonite (cpv)	AgPbCu <sub>2</sub> Bi <sub>5</sub> S <sub>10</sub>	Chalcopyrite	Rare
Tetradymite (ttd)	Bi <sub>2</sub> Te <sub>2</sub> S	Chalcopyrite	Very rare
Scheelite (sch)	CaWO <sub>4</sub>	Chalcopyrite	Rare
Cassiterite (cst)	SnO <sub>2</sub>	Chalcopyrite	Rare
Roquesite (roq)	CuInS <sub>2</sub>	Bornite	Very rare
Tungstenite (tun)	WS <sub>2</sub>	Bornite	Very rare
Luzonite (luz)	Cu <sub>3</sub> (As,Sb)S <sub>4</sub>	Chalcocite	Very rare
Chalcostibite (ch)	CuSbS <sub>2</sub>	Chalcocite	Very rare
Stromeyerite (str)	AgCuS	Bornite	Very rare
Furutobeite (fur)	Cu <sub>5</sub> AgPbS <sub>4</sub>	Bornite	Very rare
Tellurium (Te)	Te	Chalcopyrite	Very rare
Stützite (stu)	Ag <sub>7</sub> Te <sub>4</sub>	Chalcopyrite	Very rare
Kostovite (kos)	AuCuTe <sub>4</sub>	Chalcopyrite	Very rare
Sylvanite (syl)	AgAuTe <sub>4</sub>	Chalcopyrite	Very rare
Stannite (st)	Cu <sub>2</sub> FeSnS <sub>4</sub>	Chalcopyrite	Very rare
Kësterite (kes)	Cu <sub>2</sub> ZnSnS <sub>4</sub>	Chalcopyrite	Very rare
Kiddcreekite (kid)	Cu <sub>6</sub> WSnS <sub>8</sub>	Chalcopyrite, bornite	Very rare

Table 6

Gangue Minerals			
Mineral (abbreviation)	Formula	Ore Type	Abundance
Hematite (hem)	$\text{Fe}_2\text{O}_3$	Fringe, chalcopyrite	Very abundant
Magnetite (mag)	$\text{Fe}_3\text{O}_4$	Fringe, chalcopyrite	Abundant
Quartz (qtz)	$\text{SiO}_2$	All	Very abundant
Chlorite (clinochlore) (chl)	$\text{Mg}_5\text{Al}(\text{AlSi}_3\text{O}_{10})(\text{OH})_8$	Fringe, chalcopyrite	Abundant
Anhydrite (anh)	$\text{CaSO}_4$	Chalcopyrite	Abundant
Barite (brt)	$\text{BaSO}_4$	Chalcopyrite	Rare
Apatite (ap)	$\text{Ca}_5(\text{PO}_4)_3(\text{F},\text{Cl},\text{OH})$	Chalcopyrite	Rare
Calcite (cal)	$\text{CaCO}_3$	Chalcopyrite, Zn-Pb	Abundant
Dolomite (dol)	$\text{CaMg}(\text{CO}_3)_2$	Chalcopyrite, bornite	Abundant
Siderite (sd)	$\text{FeCO}_3$	Zn-Pb	Common
Rhodochrosite (rds)	$\text{MnCO}_3$	Zn-Pb	Common
Muscovite (ms)	$\text{KAl}_2(\text{Si}_3\text{Al})\text{O}_{10}(\text{OH})_2$	Bornite, Zn-Pb	Abundant
Kaolinite-Dickite (kln)	$\text{Al}_2\text{Si}_2\text{O}_5(\text{OH})_4$	Chalcocite	Abundant

Table 7

Deposit	Age	Host Rocks	Associated Porphyry Cu	Types of Ore bodies	Early Minerals	Ore Stage	Minor Element Mineralogy	References
Bisbee, Arizona, USA	Jurassic	argillaceous limestones and quartzite	Yes	Replacements	Py-qtz bodies	Mt, hm, qtz, anh, chl, py, cpy, sl, gn, bn, cc, dg, en, lz, tn-tt, cv, ala	Early: cas, sch, uraninite; Late: tellurides, Bi-sulfosalts, Cu-Sn-W-V sulfides	This study, Trischka (1938), Bryant (1964), Bryant and Metz (1966), Criddle et al. (1982)
Magma, Arizona, USA	Paleocene	limestones, diabase and schist	No	Veins and replacements	Py, qtz	Mt, hm, anh, qtz, chl, py, cpy, bn, cc, dg, en, tn-tt, sl, gn	Early: wlf; Late: cas, uraninite, tellurides, Bi-sulfosalts, Cu-Sn-V sulfides,	Gustafson (1961), Hammer and Peterson (1968), Frieauf (1998)
Butte, Montana, USA	Paleocene	Quartz monzonite	Yes	Veins	Py, qtz	Py, cpy, sl, gn, bn, cc, dg, en, tn, cv	Late: Cu-V sulfides	Sales and Meyer (1949), Meyer et al. (1968), Rusk et al. (2008)
Morococha, Peru	Late Miocene	carbonate and volcanic rock, granodiorite to diorite	Yes	Veins and replacements	Py-qtz bodies, po, asp	Mt, hm, qtz, py, cpy, tn-tt, en, sl, gn, ala	Early: sch, wlf, stn; Late: tellurides, Bi-sulfosalts, Cu-Sn-V sulfides	Catchpole et al. (2012)
Cerro de Pasco, Peru	15-11 Ma	Conglomerate, phyllite, carbonate rocks	No	Veins and replacements	Py-qtz body, po, asp, sl	En, fm, tn-tt, sl, gn	Early: wlf, cas, stn; Late: Bi-sulfosalts, Cu-Sn-V sulfides	Einaudi (1977), Baumgartner et al. (2008)
Colquijirca, Peru	Miocene	carbonate rocks and clastic sediments	No	Replacements	Py, qtz, sl	Mt, hm, sid, py, cpy, bn, tn-tt, en, lz, cc, dg, cv, sl, gn	Early: wlf; Late: Bi-sulfosalts, Cu-Sn-V sulfides	Bendezú and Fontboté (2008)
Chuquicamata, Chile	Eocene-Oligocene	quartz-feldspar porphyries	Yes	Veins	Py, qtz	Anh, py, cpy, bn, cc, dg, cv, en, tn, sl, id	Early: wlf; Late: col	López (1939), Lewis (1997), Ossandón et al. (2001)
Elshitsa, Bulgaria	Late Cretaceous	Dacitic to andesitic volcanic and subvolcanic rocks	Yes	Replacements	Py, qtz	Py-mar, anh, cpy, bn, tn-tt, en, cv, sl, gn	Early: cas; Late: tellurides, Bi-sulfosalts, Cu-Sn-V sulfides	Kouzmanov et al. (2005), Kouzmanov et al. (2009)

## APPENDIX 1: PETROGRAPHIC DESCRIPTIONS

This appendix contains petrographic descriptions of samples used in this study. Each entry begins with a header containing the sample's identification number, collection to which it belongs, and locality information, followed by a description.

**Sample ID:** 108 (UAMM)

**Locality:** Denn shaft

**Description:** Massive bornite (70%) containing a copper sulfide (25%) and minor amounts of accessory minerals as small, rounded grains, and dolomite gangue (5% or less). Copper sulfide occurs as veinlets and irregular masses within bornite, the larger masses exhibiting an “emulsion” texture of tiny bornite blebs within the copper sulfide. The copper sulfide is non-pleochroic and weakly anisotropic, indicating chalcocite. Accessory minerals include orangey mawsonite (orange to blue anisotropy), greenish-gray isotropic tennantite, buff colusite, and several tiny grains of native Au.

**Sample ID:** 3169 (UAMM)

**Locality:** Junction shaft

**Description:** Bornite (65%) containing a Cu-S mineral (30%) and various accessory minerals with minor dolomite gangue (5% maximum). Copper sulfide shows no pleochroism, but is weakly anisotropic, indicating chalcocite. Copper sulfide occurs as veins and irregular masses within bornite, with the larger veins and masses containing oriented (along {111}?) “grating” and/or “emulsion” texture of bornite in their centers, most likely exsolution textures. Bornite and chalcocite contain numerous accessory minerals. Most common accessories are rounded grains of brownish sulfides interpreted as stannoidite (red to yellow anisotropy) to 0.3 mm, mawsonite (orange to blue anisotropy) to 0.1 mm. Other phases are also found as rounded grains in both bornite and chalcocite, and are greenish-gray isotropic tennantite-tetrahedrite, galena, buff-colored colusite (EDS verified) either alone or overgrown by a purplish-gray isotropic phase (kiddcreekite by WDS).

**Sample ID:** 3919 (UAMM)

**Locality:** Junction shaft

**Description:** Sample predominantly composed of tiny intergrown subhedral to euhedral pyrite crystals averaging 0.1 mm (80%), interstices and veinlets filled with bornite (10%), chalcopyrite

(2%), and copper sulfides (7%). Chalcopyrite is rare, occurring as irregular grains within and concave to bornite. Copper sulfides never occur in direct contact with chalcopyrite. Masses of copper sulfides occur within bornite, often in direct contact with pyrite, and contain oriented “grating” texture of bornite. Two distinct copper sulfides present: a steel gray, non-pleochroic and weakly anisotropic phase interpreted as chalcocite, and a bluish-gray, non-pleochroic and isotropic phase interpreted as digenite. They occur in direct contact with one another. Rounded grains of greenish-gray tennantite-tetrahedrite (EPMA), orangey mawsonite (orange to blue anisotropy), and a pale buff, isotropic phase interpreted as colusite (EDS verified); accessories are all smaller than 0.01 mm and compose 1% or less of the sample.

**Sample ID:** 5518 (UAMM)

**Locality:** Campbell shaft

**Description:** Massive bornite (40%) and chalcopyrite (35%) intergrown with subhedral to euhedral pyrite (20%) and numerous other sulfides (2%) in a quartz-mica gangue (2%). Pyrite predominantly occurs as angular masses to several mm, the edges of which exhibit sharp crystal faces to almost 0.5 mm and the cores made up of irregular subhedral pyrite intergrown with quartz and Cu-Fe sulfides. Chalcopyrite appears moth-eaten with edges of chalcopyrite masses exhibiting caries texture chalcopyrite concave to bornite. Chalcopyrite shows polysynthetic twinning under crossed polars. Accessory phases consist of tennantite-tetrahedrite, stannoidite, mawsonite, sphalerite, and galena. Accessory sulfides occur as rounded, often resorbed grains predominantly within bornite, only scattered galena and sphalerite occur in chalcopyrite.

**Sample ID:** 5833 (UAMM)

**Locality:** Sacramento shaft

**Description:** Large grains of pyrite (30%) intergrown with chalcopyrite (50%), hematite (5%), and magnetite (5%) in a gangue (10%) of quartz and minor sheet silicate. Green internal reflections indicate sheet silicate is a chlorite (Raman spectrum = clinocllore). Pyrite grains reach 4 mm and

appear shattered and cemented by chalcopyrite. Edges of pyrite grains and fracture surfaces show smooth, scalloped edges against chalcopyrite. Pyrite is sieve textured, with 20% or less inclusions of chalcopyrite, hematite, magnetite, and quartz. Equant iron-oxide grains within chalcopyrite are composed of hematite rims with magnetite cores, indicating magnetite predates hematite. Hematite also occurs as long blades to 2 mm within chalcopyrite and pyrite. Small, irregular grains of a bright white, non-pleochroic and anisotropic mineral occur as inclusions in chalcopyrite (WDS = Cu-Bi-Pb-S phase). One transparent grain intergrown with quartz and exhibiting perfect cleavage was identified by Raman spectroscopy as barite.

**Sample ID:** 12783 (UAMM)

**Locality:** Copper Queen mine

**Description:** Massive chalcopyrite (90%) cut by 2-4 mm thick veinlet of alabandite (8%) and rhodochrosite (2%). Veinlet walls are wavy, uneven (replacement?). Alabandite exhibits greenish internal reflections, and is concave to rhodochrosite. Rhodochrosite forms the centerline of the veinlet, either as anhedral aggregates or euhedra lining vugs. Scattered, irregular galena grains in alabandite of ambiguous position.

**Sample ID:** 1202 (BNS collection, now in UAMM)

**Locality:** Unknown mine, Bisbee district

**Description:** Massive bornite (50%) and chalcopyrite (15%) occurring with pyrite (20%) grains to 3 mm in a gangue of quartz and mica (10%). Chalcopyrite is twinned under crossed polars, and exhibits caries texture against bornite; chalcopyrite is concave to bornite. Pyrite grains appear shattered and cemented by bornite and/or chalcopyrite. Grain edges and fracture surfaces appear smooth and scalloped against bornite and chalcopyrite. Pyrite grains are sieve textured, containing 20% or less ovoid inclusions of bornite, chalcopyrite, and/or euhedral inclusions of quartz and hematite. Accessory minerals include sphalerite (up to 5% of the sample), galena, stannoidite (yellow to red anisotropy) mawsonite (orange to blue anisotropy), tennantite-tetrahedrite, and

colusite. One very tiny (<0.1 mm) resorbed grain of kiddcreekite is present, with scattered low-reflectivity tungstenite in association.

**Sample ID:** R1080 (BNS collection)

**Locality:** Campbell shaft

**Description:** Irregular grains of pyrite to 2 mm (70%) with chalcopyrite (20%) and numerous other sulfides (5%) in a gangue of quartz (5%). Chalcopyrite surrounds pyrite grains, whose edges are rounded and scalloped against the chalcopyrite. The accessory sulfides occur as inclusions in chalcopyrite within the interstices of pyrite grains or as inclusions within the pyrite itself.

Accessory phases are dominated by kiddcreekite (2%), colusite (1%) and a phase tentatively identified as stannoidite (3% of the sample; pinkish brown, pleochroic, anisotropic in shades of yellow and red). Less common accessory phases in the sample are native tellurium (low hardness, high reflectivity, and white to blue anisotropy) and tennantite. Kiddcreekite rims colusite, and colusite contains inclusions of tennantite and chalcopyrite. Native tellurium occurs as fracture fillings within all sulfides.

**Sample ID:** R688 (Graeme family collection)

**Locality:** Campbell shaft

**Description:** Subhedral to euhedral pyrite crystals to 1 cm (40%) in a gangue of quartz (30%) and calcite (30%). Chalcopyrite and tellurides occur as ovoid inclusions within and as fracture fillings between pyrite crystals. Telluride inclusions are very small, generally <0.1 mm. Some complex inclusions in pyrite are composed of tennantite and sphalerite cores overgrown by stannoidite (EDS) and tellurides. Very high relief grains with a poor polish and reflectivity only slightly higher than quartz were identified by EDS as cassiterite. Cassiterite grains are embayed by other minerals except gangue, and exhibit no reaction rims. EDS results show the tellurides are sylvanite, altaite, stützite, and kostovite. Altaite and kostovite are far more common than either sylvanite or stützite.

**Sample ID:** R1147 (Graeme family collection)

**Locality:** Campbell shaft

**Description:** Euhedral pyrite crystals (25%) to 3 mm within a matrix of silvery white sulfides (45%) and chalcopyrite (30%). Pyrite grains are sieve-textured, containing 20% or less inclusions of chalcopyrite and other sulfides. Pyrite grains exhibit sharp edges against all other minerals. Two phases compose the masses of silvery white sulfides. One of the other phases, composing approximately 30% of the sample, is bright silvery white in color, reflectivity higher than pyrite, exhibiting low to moderate pleochroism, distinct anisotropy in gray, brown, and reddish shades and exhibiting strong polysynthetic twinning (EPMA = cupropavonite). The second phase (15% of the sample) is grayish, lower reflectivity than chalcopyrite and pyrite, weakly pleochroic and anisotropic in red, bluish-purple, and white shades and is untwinned, suggestive of aikinite (EPMA = krupkaite).

**Sample ID:** R1152 (Graeme family collection)

**Locality:** Junction shaft

**Description:** Massive enargite (35%) and tennantite (50%) containing small amounts of pyrite (5% or less), chalcopyrite (2%), and bornite (2%) with quartz gangue (5%). Enargite and tennantite are complexly intergrown. Tennantite completely rims and cuts across enargite masses, in places nearly forming a complete replacement. Enargite is optically continuous through tennantite veining, indicating tennantite post-dates enargite formation. The scattered pyrite grains are often surrounded by chalcopyrite and bornite. Pyrite grains exhibit uneven, scalloped edges against chalcopyrite and bornite. Chalcopyrite occurs between bornite and pyrite wherever it is found. Pyrite was the earliest mineral to form, followed by chalcopyrite, bornite, enargite, and finally tennantite.

**Sample ID:** R1159 (Graeme family collection)

**Locality:** Campbell shaft, 1600 level

**Description:** Massive bornite (65%) with a copper sulfide (20%), and subhedral pyrite (10%).

Accessory sulfides compose the balance (5%) of the sample. The copper sulfide (chalcocite) occurs as veins and masses within bornite, often with several smaller blebs outside of larger masses. Stromeyerite forms masses within the chalcocite, often in myrmekitic intergrowths with wittichenite. Bladed crystals with optical properties similar to wittichenite cut across the stromeyerite-wittichenite intergrowths (EDS = furutobeite). Tennantite, native Au, and galena are also present in order of decreasing content.

**Sample ID:** R1164A (Graeme family collection)

**Locality:** Junction shaft

**Description:** Massive enargite (60%) with pyrite (35%) and quartz (5%). Accessory minerals compose less than 1% of the sample. Pyrite occurs as anhedral grains and is sieve textured, containing 15% or less inclusions of bornite, chalcopyrite, and tennantite. Bornite shows incipient exsolution of chalcopyrite. Massive enargite contains inclusions of brownish-gray tennantite-tetrahedrite (EPMA = goldfieldite), exhibiting caries concave to enargite. Enargite is veined by tennantite; vein walls are smooth and scalloped indicating replacement.

**Sample ID:** R1166 (Graeme family collection)

**Locality:** Junction shaft

**Description:** Massive luzonite (65%) with enargite (5%), tennantite-tetrahedrite (5%), chalcostibite (10%), pyrite (5%), quartz (5%), and a white sheet silicate (5%). Pyrite and quartz occurs as subhedral to euhedral crystals frozen within massive luzonite. Chalcostibite occurs as

irregular grains exhibiting caries texture concave to luzonite. Enargite and tennantite-tetrahedrite occur as partial rims on chalcostibite between it and luzonite.

**Sample ID:** R1180B (Graeme family collection)

**Locality:** Campbell shaft

**Description:** Massive hematite (70%) with magnetite (5%) and calcite (25%). Hematite shows well-developed polysynthetic twinning and contains irregular blebs of magnetite in the centers of grains. Magnetite exhibits caries texture concave to hematite, indicating hematite post-dates magnetite.

**Sample ID:** R1197 (Graeme family collection)

**Locality:** Higgins mine, Tunnel level

**Description:** Massive quartz (45%) containing massive sphalerite (35%), galena (15%), euhedral pyrite (5%), and mica (5%). Sphalerite exhibits dark reddish-brown internal reflections (high-Fe??), and has chalcopyrite disease. Galena is anhedral and typically associated with pyrite, with pyrite forming rims on some smaller galena grains and larger galena masses concave to pyrite, indicating pyrite post-dates galena. Euhedral pyrite (as pyritohedra) is disseminated throughout quartz groundmass, and some grains contain a dusting of very tiny ( $\ll 0.1$  mm) chalcopyrite inclusions in a central zone of the grains. Tiny framboidal pyrite grain, or pyritized fossil (need 1000x magnification).

**Sample ID:** R1204 (Graeme family collection)

**Locality:** Campbell shaft

**Description:** Massive bornite (50%) with a copper sulfide (20%), pyrite (10%), and sphalerite (20%). Copper sulfide is grayish white, non-pleochroic and anisotropic – chalcocite. Chalcocite occurs as large zones within bornite as “graphic” texture intergrowths suggestive of exsolution. Pyrite is euhedral (pyritohedra), and sieve-textured, with  $<15\%$  bornite-chalcocite inclusions in a central zone. Sphalerite is anhedral, concave to bornite and bornite-chalcocite, and contains inclusions of euhedral pyrite. Edges of sphalerite grains have alteration rim of brownish sulfide =

stannoidite (red to yellow anisotropy). Scattered galena and mawsonite in bornite. Two brownish gray, anisotropic grains in chalcocite (WDS = Cu-In-S; roquesite).

**Sample ID:** R1224A (Graeme family collection)

**Locality:** Higgins mine, Tunnel level

**Description:** Massive pyrite (70%) containing chalcopyrite (20%), quartz (5%), mica (3%) and a transparent mineral with slightly higher reflectivity than quartz (2%; WDS = Ca, P, O, F, Cl; apatite). Pyrite appears shattered and cemented by chalcopyrite: fracture surfaces are smooth and scalloped, embayments in many grains concave to chalcopyrite. One ~0.05 mm grain of a very highly reflective white mineral, non-pleochroic slightly anisotropic (EPMA = tetradymite). Three grayish grains in chalcopyrite and quartz with brownish internal reflections are sphalerite (EDS shows some are actually uraninite!).

**Sample ID:** R1226 (Graeme family collection)

**Locality:** Campbell shaft

**Description:** Massive pyrite (80%) and minor chalcopyrite (2%) and hematite (2%) with a gangue of quartz (10%) and calcite (5%). Quartz is euhedral and contains ~0.025 mm two-phase fluid inclusions (liq-gas, liq > gas phase). Pyrite is sieve textured, containing 10% or less inclusions of chalcopyrite and hematite, predominantly on the edges of grains. Fractures are filled with quartz, hematite, and minor chalcopyrite. Calcite occurs in larger spaces between grains filling vugs. Pyrite predates hematite, chalcopyrite, calcite; quartz predates pyrite.

**Sample ID:** R1230 (Graeme family collection)

**Locality:** Gardner shaft

**Description:** Anhedral galena (40%) in a matrix of quartz (20%) and carbonates (40%; fizz in 36% HCl). Galena is concave to carbonates, contains inclusions of euhedral quartz and anhedral sphalerite (red internal reflections). Scattered tennantite-tetrahedrite associated with galena, concave to galena (EDS = tennantite). Carbonates have pink or white internal reflections:

rhodochrosite and calcite, rhd > cal in abundance. Tiny fractures in galena show incipient replacement by covellite and sphalerite (supergene?).

**Sample ID:** R1235 (Graeme family collection)

**Locality:** Campbell shaft

**Description:** Anhedral sphalerite (30%) and galena (20%) in a quartz matrix (50%) with accessory (<1%) pyrite and tennantite-tetrahedrite and mica. Sphalerite is chalcopyrite free, and has numerous greenish to yellowish internal reflections. Sphalerite is concave to galena, as is pyrite. Both galena and sphalerite have pyrite and sheet silicate inclusions. Tennantite-tetrahedrite (Ag-rich tetrahedrite, see EMP tables) has ambiguous intergrowth texture with sphalerite and galena, but more often than not sphalerite is concave to tn-tt. Tn-tt appears to be same relative age as galena.

**Sample ID:** R1329 (Graeme family collection)

**Locality:** Gardner shaft

**Description:** Massive chalcopyrite (70%) with euhedral pyrite (10%), hematite (5-7%), magnetite (1%), quartz (10%), anhydrite (1%), sphalerite (1%). Chalcopyrite exhibits polysynthetic and minor oleander-leaf twinning. Massive chalcopyrite is host to numerous four-pointed, skeletal inclusions of low reflectance (>quartz) and reddish-brown internal reflections. Pyrite cubes contain anhedral inclusions in distinct zones, between core and edge, with identical properties. Inclusions = sphalerite. Hematite occurs predominantly as specular blades to 3 mm, one with a sphalerite inclusion. Blobby aggregates of hematite contain relict cores of magnetite. Anhydrite occurs as inclusions in chalcopyrite and quartz to 0.5 mm with colorless internal reflections and well-developed cleavage.

**Sample ID:** R1347 (Graeme family collection)

**Locality:** Campbell shaft

**Description:** Massive covellite (95%) with minor white sheet silicate (kaolinite-dickite?) (5%) and minor (>1%) quartz and pyrite. Spectacular botryoidal covellite occurring as a solid, layered mass with layers to 3 mm thick. White sheet silicate (EDS = kaolinite-dickite) and quartz occur in between layers. Pyrite occurs as scattered anhedral grains (concave to covellite) not restricted to any part of the sample.

**Sample ID:** R1375 (Graeme family collection)

**Locality:** Campbell shaft

**Description:** Massive bornite (60%) chalcocite (5%) with subhedral pyrite (15%) in a gangue of quartz (5%) and sheet silicate (10%) with minor (5%) accessory minerals. Scattered zones of graphic chalcocite-bornite intergrowths. Pyrite is sieve-textured, containing 10-20% ovoid inclusions of chalcopyrite or bornite-chalcocite. Accessory phases = tennantite-tetrahedrite, mawsonite, stannoidite, galena, and colusite.

**Sample ID:** R1387 (Graeme family collection)

**Locality:** Dallas shaft

**Description:** Massive bornite (50%) containing subhedral pyrite (20%), and chalcocite (5%) with a gangue of quartz (20%) and a sheet silicate (5%). Chalcocite occurs as graphic masses within massive bornite. Pyrite grains are sieve-textured, containing approximately 20% ovoid inclusions (in decreasing abundance) of bornite, chalcopyrite, and bornite-chalcocite intergrowths. Bornite contains small rounded inclusions of a large suite of accessory minerals: tennantite-tetrahedrite, sphalerite, mawsonite, stannoidite, colusite, galena, and native Au. Gold occurs intergrown with chalcocite in fractures and in one instance is intergrown with colusite. Inclusions of cpy in py indicate bn + py replaced earlier cpy; however py is concave to bn. Accessory phases appear to be later than cpy but earlier than bn.

**Sample ID:** R1562 (Graeme family collection)

**Locality:** Campbell shaft

**Description:** Laminated shaly limestone (Abrigo Ls) composed of 5 mm thick sulfide-quartz layers separated by 1-2 mm sheet-silicate layers. Sulfide layers are approximately 40% quartz and 60% sulfide: 50% bornite, 40% chalcopyrite, and 10% pyrite with <1% stannoidite, mawsonite, sphalerite, and galena. Quartz appears red (hematite inclusions?). Chalcopyrite is concave to bornite, pyrite is concave to both bornite and chalcopyrite. Accessory phases are rounded and occur only in bornite.

**Sample ID:** R1577B (Graeme family collection)

**Locality:** Campbell shaft

**Description:** Massive quartz (60%) containing magnetite (20%), specular hematite (10%), pyrite (3%), chalcopyrite (5%), and bright-white sulfides (~1%). Magnetite occurs as disseminated grains throughout quartz, in places pseudomorphed to hematite. Specular hematite occurs as clots of blades, often associated with sulfides. Sulfides always occur together. Pyrite is subhedral to euhedral, and contains inclusions of hematite blades, the ends of which are concave to pyrite. Pyrite is concave to chalcopyrite. Bright sulfides are composed of two phases: one distinctly anisotropic, the other very weakly anisotropic. Neither show twinning, and the distinctly anisotropic phase (reddish, orangey, white) matches descriptions of aikinite (EPMA = krupkaite; other phase = wittichenite). Magnetite-quartz was earliest, followed by hem, then pyrite, and finally chalcopyrite.

**Sample ID:** R1893 (Graeme family collection)

**Locality:** Holbrook shaft

**Description:** Massive bornite (60%) with chalcopyrite (30%) and supergene goethite (10%).

Chalcopyrite shows selective replacement over bornite. Chalcopyrite is concave to bornite. Both chalcopyrite and bornite contain rounded inclusions of tennantite-tetrahedrite and sphalerite

(<1%). Bornite contains rounded inclusions (<1%) of stannoidite, mawsonite, galena, and colusite. Stannoidite occurs as much larger grains against sphalerite. Sphalerite exhibits colorless to faintly yellow internal reflections. Chalcopyrite formed first, followed by bornite. Tn-tt, sph, before/cpy; gl, stn, mw, col after cpy but before bn.

**Sample ID:** R1959 (Graeme family collection)

**Locality:** Campbell shaft

**Description:** Hand sample shows mixed galena, sphalerite, pyrite against a zone of silicified limestone containing pyrite cubes to 4 mm, which contacts sharply against coarsely-crystalline calcite marble. Microscopy shows intergrowth of sphalerite (40%), galena (30%), pyrite (10%), and chalcopyrite (20%). Sphalerite is concave to all other sulfides except pyrite. Sphalerite is heavily chalcopyrite diseased, with a fine dusting of tiny cpy grains as a border zone against other sulfides and very coarse, linearly oriented cpy grains away from other sulfides. Reddish internal reflections. Chalcopyrite also occurs as distinct monomineralic masses of irregular outline. Galena occurs as distinct masses often with rounded grains of chalcopyrite or tennantite along its boundary with sphalerite, and is concave to chalcopyrite. Pyrite occurs as subhedral to euhedral crystals, often intergrown, in chalcopyrite. One pyrite aggregate is intergrown with tennantite-tetrahedrite and showing no replacement textures. Botryoidal siderite fills vugs. Sphalerite formed first, followed by galena, and lastly chalcopyrite. Pyrite predates chalcopyrite.

**Sample ID:** R2073 (Graeme family collection)

**Locality:** Cole shaft, 1300 level, 39-A stope

**Description:** Massive steely chalcocite (80%) containing scattered pyrite grains (15%) and bornite (5%). Chalcocite is composed of graphic intergrowth (triangular) of a grayish phase (weakly anisotropic) = chalcocite and a bluish phase (isotropic) = digenite. Chalcocite-digenite encloses anhedral bornite grains (concave to cc-dg) and scattered subhedral laths of a low reflectivity mineral with distinct reddish to greenish anisotropy = enargite. Enargite is concave to cc-dg.

Bornite grains contain spindle-shaped laths of digenite. Supergene covellite replaces cc-dg near fractures. Pyrite contains colusite inclusions, and interstitial whitish sheet silicate (EDS = kaolinite-dickite). Bn formed first, followed by cc-dg. Enargite occupies ambiguous position, as it is not observed in direct contact with bornite, but definitely predates cc-dg.

**Sample ID:** R2115 (Graeme family collection)

**Locality:** Cole shaft, 1300 level, 39-A stope

**Description:** Granular pyrite (50%) cemented by bornite (30%) in a gangue of quartz (20%), and a sheet silicate (5%). Bornite contains zones (10-20% of bornite) of bluish, isotropic copper sulfide = digenite. Accessory tennantite-tetrahedrite and mawsonite occur within bornite. Pyrite is anhedral to subhedral and contains inclusions (<5%) of bornite, bornite-digenite, and chalcopyrite. Pyrite is concave to bornite. Vugs in bornite contain rare blebs of native Au to several mm. Pyrite appears to be earlier than or coeval to bornite, perhaps as a replacement of cpy as bn + py (cpy inclusions in py). Accessories predate bornite, except digenite which exsolved from bn on cooling.

**Sample ID:** R2336 (Graeme family collection)

**Locality:** Lavender pit, Holbrook extension

**Description:** Massive sulfides (90%) containing fragments of altered shaly limestone (10%), themselves partially replaced by sulfides (intrusive breccia ore). Massive sulfide composed of bornite (80%), chalcopyrite (15%), and pyrite (5%). Chalcopyrite is concave to bornite, and contains scattered inclusions of tennantite-tetrahedrite. Away from chalcopyrite, bornite contains zones of graphic chalcocite-bornite exsolutions. Pyrite contains rare inclusions of bornite. Tiny inclusions of mawsonite, stannoidite, and galena occur throughout bornite, regardless of proximity to chalcopyrite. Mawsonite occurs as rims on most stannoidite grains. Chalcopyrite earlier than bornite, pyrite coeval with bornite, accessories earlier than or slightly later than cpy but earlier than bn.

**Sample ID:** R2412 (Graeme family collection)

**Locality:** Sacramento shaft

**Description:** Bornite (15%) and chalcopyrite (30%) with granular pyrite (50%), cut by a veinlet of dolomite (5%). Chalcopyrite is concave to bornite. Pyrite grains exhibit one or more skeletal faces partially to fully enclosing bornite; the other faces are rounded. Bornite contains rare inclusions of tennantite-tetrahedrite and colusite. At the borders of dolomite veinlet, enargite-tennantite intergrowths replace bornite. Tennantite always rims enargite on the bornite side. Chalcopyrite formed first, followed by bornite + pyrite. A later mineralization episode formed the dolomite vein and replaced bornite with enargite, which was in turn replaced by tennantite.

**Sample ID:** R4818 (Graeme family collection)

**Locality:** Cole shaft

**Description:** Massive covellite (90%) with sphalerite (5%), pyrite (1%), galena (1%), with quartz (2%) and kaolinite-dickite (1%) gangue. Covellite is coarse, with individual blades to 1 mm long and 0.1 mm wide. Some areas of more finely crystalline covellite exhibit banding of alternating coarse and fine layers. Inclusions of sphalerite and galena are present throughout the sample at both microscopic and macroscopic scale. At the micro scale, monomineralic sphalerite grains are concave to sphalerite, while sphalerite-galena aggregates exhibit sharp cleavages filled with covellite. Pyrite is skeletal, the grains containing covellite cores or exhibiting one-directional growth from a base of covellite blades with sharp contacts on the bottom side. Covellite + pyrite formed after sphalerite-galena.

**Sample ID:** 6SW (Graeme family collection, now in UAMM)

**Locality:** Southwest mine, 6 level

**Description:** Massive chalcopyrite (70%) with pyrite (20%) and bornite (10%). Pyrite and bornite occur in veinlets or concave zones within massive chalcopyrite. Pyrite is subhedral to euhedral (cubic) and in nearly all cases heavily fractured. Fractures filled with bornite and/or tennantite-tetrahedrite. One tennantite-tetrahedrite grain is mostly included in chalcopyrite, with only a small

corner in bornite. Chalcopyrite formed first, followed by bornite, tn-tt and py either formed before or contemporaneous with bornite.

**Sample ID:** BCQ (Graeme family collection, now in UAMM)

**Locality:** Copper Queen mine, B level

**Description:** Massive sphalerite (60%) with galena (10%), pyrite (5%) in a gangue of quartz

(20%) and carbonate (5%). Pyrite occurs as subhedral to euhedral crystals (pyritohedra) within sphalerite and quartz, often occurring as distinct zones mimicking sphalerite crystal forms. Faint chalcopyrite disease accompanies the pyrite-rich zones. Galena occurs as irregular grains within quartz and carbonate outside of sphalerite aggregates, often filling vugs. Sphalerite (with or without pyrite) formed first, followed by galena and gangue.

## APPENDIX 2: MICROPROBE DATA AND MINERAL NORMALIZATIONS

This appendix contains a complete record of microprobe analyses completed in the course of this study. The results are presented by mineral, with weight percent of each element above normalization.

## TABLE EXPLANATORY NOTES

Table A2-1. Sphalerite compositions from Bisbee. Elements Ge, Ga, and Cd were analyzed for but not detected.

Table A2-2. Compositions of stannoidite. Note: na = not analyzed.

Table A2-3. Compositions of tennantite-tetrahedrite group minerals. Note: nd = not detected.

Table A2-4. Compositions of other minerals analyzed during the course of the study.

## TABLES

Table A2-1

Ore Type	Pyrite	Chalcopyrite	Chalcopyrite	Bornite	Bornite	Bornite	Bornite
Sample	R1329	R1329	R1224	5518	R1204	R1893	1202
Element							
Zn	60.46	62.88	64.95	64.94	66.72	67.01	66.56
Fe	5.31	2.40	1.20	0.27	0.02	0.04	0.10
Cu	0.08	1.69	0.65	0.96	0.07	0.11	0.29
Mn	nd	nd	nd	nd	0.05	nd	0.06
S	33.85	33.43	33.80	33.45	33.25	33.67	33.20
Total	99.70	100.40	100.60	99.62	100.11	100.83	100.21
Atoms*							
Zn	0.92	0.97	0.97	0.98	0.99	0.99	0.99
Fe	0.07	0.02	0.01	0.00	0.00	0	0.00
Cu	0.00	0.00	0	0.00	0.00	0.00	0.00
Mn	-	-	-	-	0.00	0.00	0.00
S	1.00	1.00	1.03	1.01	1.02	1.03	1.02
X <sub>FeS</sub>	0.075	0.017	0.011	0.000	0.0004	0	0.000
Mol % Fe	7.5	1.7	1.1	0.0	0.0	0	0

\*Note: corrected for interference from chalcopyrite disease by subtracting a 1:1:2 molar ratio of Cu:Fe:S during normalization.

Table A2-1, continued

Ore Type	Zn-Pb	Zn-Pb	Zn-Pb	Zn-Pb	Zn-Pb	Zn-Pb	Zn-Pb
Sample	R1235	R1959 rim	R1959 core	R1197	BCQ rim	BCQ mid	BCQ core
Element							
Zn	66.04	64.96	64.00	66.33	66.06	66.20	65.53
Fe	0.13	0.28	1.25	0.30	0.02	0.16	0.40
Cu	0.06	0.14	0.20	0.08	0.04	0.03	0.03
Mn	0.30	1.49	1.49	0.08	0.45	0.34	0.46
S	33.15	33.59	33.65	33.19	33.16	33.13	33.20
Total	99.68	100.46	100.59	99.98	99.73	99.86	99.62
Atoms*							
Zn	0.99	0.96	0.95	0.99	0.98	0.98	0.98
Fe	0.00	0.00	0.02	0.00	0.00	0.00	0.01
Cu	0.00	0.00	0.00	0.00	0.00	0.00	0.00
Mn	0.01	0.03	0.03	0.00	0.01	0.01	0.01
S	1.01	1.01	1.03	1.03	1.02	1.00	1.02
X <sub>FeS</sub>	0.0012	0.003	0.019	0.004	0.0004	0.002	0.007
Mol % Fe	0.12	0.3	1.9	0.4	0.04	0.2	0.7

Table A2-2

Sample	3169	5518	R1204	R1893	R2336	1202
Element						
Cu	38.76	39.88	39.33	39.08	40.09	38.45
Fe	8.47	8.75	8.48	8.66	8.88	8.38
Zn	4.42	4.30	5.58	5.39	4.25	6.71
Sn	17.57	17.34	18.01	17.27	17.43	17.89
S	29.25	29.70	29.08	29.76	29.55	29.33
As	0.38	na	na	na	na	na
Total	98.85	99.97	100.48	100.16	100.20	100.76
Atoms						
Cu	8.05	8.16	8.08	7.98	8.22	7.87
Fe	2.00	2.04	1.98	2.01	2.01	1.95
Zn	0.89	0.85	1.12	1.06	0.85	1.33
Sn	1.95	1.90	1.98	1.89	1.91	1.96
As	0.07	-	-	-	-	-
S	12.04	12.05	11.84	12.05	12.01	11.89
$\Sigma_{\text{Cat}}$	12.96	12.95	13.16	12.94	12.99	13.11

Table A2-3

Ore Type Sample	Bornite 3169 Rim	Bornite 3169 Core	Bornite 3919	Bornite 5518	Bornite R2115	Bornite R2336 rim	Bornite R2336 core	Bornite 6SW
Element								
Cu	42.72	41.65	42.80	43.11	42.67	44.61	44.32	43.02
Fe	0.14	0.22	0.87	0.46	0.34	0.40	0.21	0.90
Zn	7.74	7.80	7.55	7.88	8.22	5.79	6.79	7.26
As	19.49	18.11	19.10	18.81	18.66	16.39	17.68	16.39
Sb	0.41	0.21	0.26	0.68	0.50	0.49	0.27	3.09
Te	0.53	0.13	0.32	0.54	0.08	4.65	2.93	1.93
Bi	0.66	4.37	nd	0.14	0.58	0.15	0.15	nd
Pb	nd	nd	nd	nd	nd	nd	nd	nd
Ag	0.18	0.30	nd	0.03	nd	nd	nd	nd
Se	nd	nd	nd	nd	nd	nd	nd	nd
S	28.24	27.29	28.69	28.62	28.92	27.89	27.94	28.43
Total	100.11	100.08	99.58	100.25	99.97	100.37	100.29	101.02
Atoms								
Cu	10.02	10.01	9.97	10.03	9.93	10.56	10.44	10.07
Fe	0.04	0.06	0.23	0.12	0.09	0.11	0.06	0.24
Zn	1.76	1.82	1.71	1.78	1.86	1.33	1.55	1.65
As	3.88	3.69	3.77	3.71	3.68	3.29	3.53	3.25
Sb	0.05	0.03	0.03	0.08	0.06	0.06	0.03	0.38
Te	0.06	0.02	0.04	0.06	0.01	0.55	0.34	0.22
Bi	0.05	0.32	0	0.01	0.04	0.01	0.01	0
Pb	0	0	0	0	0	0	0	0
Ag	0.03	0.04	0	0	0	0	0	0
Se	0	0	0	0	0	0	0	0
S	13.12	13.00	13.24	13.2	13.33	13.09	13.04	13.19
$\Sigma_{\text{Cat}}$	15.89	15.99	15.75	15.79	15.67	15.91	15.96	15.81

Table A2-3, continued

Ore Type Sample	Pre-Chalcocite R1164 Rim	Pre-Chalcocite R1164 Core	Chalcocite R1152	Chalcocite R1166	Zn-Pb R1235	Zn-Pb R1959
Element						
Cu	47.32	44.54	47.73	42.30	31.72	42.68
Fe	0.04	0.01	3.11	1.75	0.08	3.23
Zn	0.21	0.01	0.04	0.05	7.66	5.21
As	6.93	3.66	18.97	5.71	0.52	20.60
Sb	3.98	2.33	0.39	20.79	28.08	0.15
Te	15.53	19.81	0.01	0.13	nd	nd
Bi	0.51	5.04	0.10	0.13	nd	nd
Pb	nd	nd	nd	nd	nd	nd
Ag	0.04	0.03	1.40	4.41	8.09	0.06
Se	nd	nd	nd	nd	nd	nd
S	26.28	25.59	28.52	25.47	24.26	28.32
Total	100.84	101.02	100.27	100.74	100.41	100.25
Atoms						
Cu	11.88	11.64	11.08	10.83	8.58	9.89
Fe	0.01	0	0.82	0.51	0.02	0.85
Zn	0.05	0	0.01	0.01	2.01	1.17
As	1.47	0.81	3.73	1.24	0.12	4.05
Sb	0.52	0.32	0.05	2.78	3.96	0.02
Te	1.94	2.58	0	0.02	0	0
Bi	0.04	0.40	0.01	0.01	0	0
Pb	0	0	0	0	0	0
Ag	0.01	0.01	0.19	0.67	1.29	0
Se	0	0	0	0	0	0
S	13.07	13.24	13.11	12.93	13.01	13.01
$\Sigma_{\text{Cat}}$	15.92	15.76	15.89	16.07	15.98	15.98

Table A2-4

Mineral Sample	Chalcostibite R1166	Luzonite R1166	Cupropavonite R1147	Krupkaite R1147	Tetradymite R1224*	Mawsonite R2336	Wittichenite R1577
Element							
Cu	25.5	46.22	4.45	5.76	2.64	44.38	33.17
Fe	nd	nd	0.01	0.02	2.02	13.09	0.59
Zn	nd	nd	nd	nd	0.35	0.02	0.04
Sn	nd	nd	nd	nd	nd	13.62	nd
As	0.44	9.66	nd	nd	nd	na	nd
Sb	46.56	14.27	0.01	0.06	0.29	na	0.03
Te	nd	0.01	0.24	nd	34.31	na	0.02
Bi	3.09	nd	60.22	57.8	57.14	na	45.83
Pb	nd	nd	8.93	20.63	nd	na	0.31
Ag	nd	0.04	10.06	nd	0.08	na	0.59
Se	nd	0.01	0.06	0.01	1.18	na	0.03
S	25.29	30.96	17.86	17.73	4.47	29.73	18.97
Total	100.87	101.17	101.83	102.07	102.66	100.86	99.51
Atoms							
Cu	1.02	3.01	0.63	0.98	0	6.03	2.70
Fe	0	0	0	0	0	2.02	0.05
Zn	0	0	0	0	0	0	0
Sn	0	0	0	0	0	0.99	0
As	0.01	0.53	0	0	0	0	0
Sb	0.97	0.49	0	0	0.02	0	0
Te	0.00	0	0.02	0	1.95	0	0
Bi	0.04	0	2.59	3.00	1.92	0	1.14
Pb	0	0	0.39	1.08	0	0	0.01
Ag	0	0	0.84	0	0.01	0	0.03
Se	0	0	0.01	0	0.10	0	0
S	2.00	4.00	5.00	6.00	0.96	8.00	3.07
Ore Type	Chalcocite	Chalcocite	Chalcopyrite	Chalcopyrite	Chalcopyrite	Bornite	Chalcopyrite

\*Note: Corrected for interference from host chalcopyrite by subtracting a 1:1:2 molar ratio of Cu:Fe:S during normalization.